HIGH ENERGY MEASUREMENTS OF THE DEUTERON PHOTODISINTEGRATION DIFFERENTIAL CROSS SECTION

BY

ELAINE CAROL SCHULTE

B.S., University of Illinois at Urbana-Champaign, 1997
M.S., University of Illinois at Urbana-Champaign, 2001

THESIS

Submitted in partial fulfillment of the requirements
for the degree of Doctor of Philosophy in Physics
in the Graduate College of the
University of Illinois at Urbana-Champaign, 2002

Urbana, Illinois

HIGH ENERGY MEASUREMENTS OF THE
DEUTERON PHOTODISINTEGRATION DIFFERENTIAL CROSS SECTION

Elaine Carol Schulte, Ph.D.
Department of Physics
University of Illinois at Urbana-Champaign, 2002
R. J. Holt, Advisor

New measurements of the high energy deutron photodisintegration differential cross section were made at the Thomas Jefferson National Accelerator Facility in Newport News, Virginia. Two experiments were performed. Experiment E96-003 was performed in experimental Hall C. The measurements were designed to extend the highest energy differential cross section values to 5.5 GeV incident photon energy at forward angles. This builds upon previous high energy measurements in which scaling consistent with the pQCD constituent counting rules was observed at 90° and 70° in the center of mass. From the new measurements, a threshold for the onset of constituent counting rule scaling seems present at transverse momentum approximately 1.3 GeV/c. The second experiment, E99-008, was performed in experimental Hall A. The measurements were designed to explore the angular distribution of the differential cross section at constant energy. The measurements were made symmetric about 90° in the center of mass. The results, which are neither consistent with meson exchange nor quark-exchange, remain puzzling.

Acknoweledgements

As with all great endevors, this one was the product of a great effort on the part of many people. Without their interest and professional support neither of these experiments would have been accomplished. My sincere gratitude is extended to the entire scientific, technical, and support staff at Jefferson Laboratory.

I also extend great thanks to my research advisor Dr. Roy Holt. Had it not been for his constant encouragement to continue my education at the University of Illinois, I never would have "been in the right place at the right time." This single event has been paramount in my success as a graduate student. I am also greatful for his encouragement and professional support through rousing "discussions" and a change of location to Argonne National Laboratory when he assumed leadership of the medium energy physics group. He has been a great teacher, and the honor was mine.

I also extend my thanks to the University of Illinois Department of Physics its staff and the Nuclear Physics Laboratory at the University of Illinois, especially Eric Thorsland and Penny Sigler for all of the many things I learned from the help and experiences they shared with me. Also, I extend my thanks to Argonne National Laboratory, and its staff.

I wish to thank my family, especially my sister Jessica and parents who always reminded me that graduate education is a privilege. They always help to keep everything in perspective. Without them I would have never survived this experience.

This work was supported by the University of Illinois at Urbana-Champaign Department of Physics, the National Science Foundation under grant numbers NSF PHY 94-20787 and NSF PHY 00-72044 the Thomas Jefferson National Accelerator Facility, Argonne National Laboraotry, and the United States Department of Energy under contract number W-31-109-Eng-38.

Contents

Chapter 1: Introduction: Why Study Deuteron Photodisintegration? 1

Chapter 2: Meson Exchange vs. QCD 3

2.1 Meson Exchange Theory 4

2.2 Quantum Chromodynamics 6

Chapter 3: Available Descriptions of Deuteron Photodisintegration . 10

3.1 Traditional Meson Exchange 11

3.1.1 Lee's Model 11

3.1.2 Laget's Model 14

3.2 Asymptotic Meson Exchange (AMEC) 16

3.3 Reduced Nuclear Amplitudes/Quark Exchange 18

3.4 Hard Rescattering Model 21

3.5 Quark Gluon String 23

3.6 Perturbative Quantum Chromodynamics–
Constituent Counting Rules 25

Chapter 4: High Energy Deuteron Photodisintegration Experiments 29

4.1 Scaling in Photoproduction Reactions 30

4.2 Electron-Deuteron Elastic Scattering 32

4.3 The Search for Hadron Helicity 33

4.4 Progress in Deuteron Photodisintegration Cross Section Measurements 34

4.5 The New Jefferson Lab Experiments: E96-003 and E99-008 36

Chapter 5: Experimental Procedure 38

5.1 The CEBAF Accelerator 39

5.1.1 Beam Position Measurements 41

5.1.2 Beam Energy Measurements 42

5.1.3 Beam Current Measurement 43

5.2 Bremsstrahlung Radiator and Targets 44

5.2.1 The Bremsstrahlung Radiator 45

5.2.2 The Halls A and C Cryotarget 46

5.3 Detection 49

5.3.1 Quadrupoles 50

5.3.2 Dipoles 52

5.3.3 Detectors 52

5.3.3.1 Drift Chambers 55

5.3.3.2 Scintillation Detector 57

5.3.3.3 Čerenkov Counters 58

5.3.3.4 The Lead Glass Calorimeter 59

5.4 The Trigger 59

5.4.1 The HMS Trigger 61

5.4.2 The Hall A Trigger 63

Chapter 6: Analysis of Deuteron Photodisintegration Data 64

6.1 Spectrometer Checkout 65

6.1.1 Reconstruction of the Photon Energy Spectrum, E_γ 71

6.1.1.1 Collimator and Exit Dipole Cuts 71

6.1.1.2 Particle Identification 73

6.1.1.3 Remaining Analysis Cuts 78

6.1.2 The E_γ Spectrum 80

6.1.2.1 Determination of the Photoproton Yield 80
6.2 Determination of the Differential Cross Section 87
6.2.1 Photoproton Yield for E96-003 89
6.2.2 Photoproton Yield for E99-008 89
6.2.3 Normalization of the Photoproton Yield 90
6.2.3.1 Efficiencies 91
6.2.3.2 Proton Attenuation 92
6.2.3.3 Bremsstrahlung 95
6.2.3.4 Virtual Bremsstrahlung 98
6.2.3.5 The Solid Angle $\Delta\Omega$ 100
6.2.4 The Differential Cross Section 101
6.3 Systematic Errors 103

Chapter 7: Results and Discussion 106
7.1 Consistency of E96-003 and E99-008 106
7.2 Theories Revisited 109
7.3 What Has Been Encountered? 115

Chapter 8: Summary 119

Chapter 9: Outlook 121

References 122

Appendix A: Mandelstam Variables 128

Appendix B: Time of Flight Optimization 130

Vita 132

List of Figures

1.1 Schematic diagram of the exclusive deuteron photodisintegration reaction. 2

2.1 $s^{11}\frac{d\sigma}{d\Omega}$ for the $d(\gamma,p)n$ reaction up to a photon energy of 4 GeV at $\theta_{cm} = 90°$. The the solid curve is the meson exchange model developed by T.S-H. Lee [10] and the long dashed curve is the meson exchange model developed by Laget [11]. Notice that above 0.5-0.8 GeV the present models are unable to reproduce the present data. The data appear to follow an s^{-11} dependence. Data are from Refs. [12, 13, 14, 15] . . . 6

3.1 Diagram of Lee's meson exchange current model. Figure a) shows the basic model being studied. Figure b) shows detail of the nucleon-nucleon final state interaction described in the model. The "bubble" in b) represents the half-off shell t-matrix governing the final state nucleon-nucleon interaction [10]. 11

3.2 Leading diagrams for Laget's model a) the deuteron pole; b) the nucleon pole; c) nucleon-nucleon rescattering; d) pion reabsorption; e) pion reabsorption followed by NN scattering. [11] 14

3.3 Asymptotic Meson Exchange Mode (AMEC) diagrams [29]. 16

3.4 Recent electron-deuteron elastic structure function results from Jefferson Lab Hall A. The figure is from Ref. [32]. The top panel shows the deuteron form factor F_d multiplied by the Q^2 dependence expected from pQCD predictions. The bottom panel shows the reduced form factor analysis from the RNA method. The dashed curve is the RNA prediction [33]. 19
3.5 Quark Exchange Model [34]. 20
3.6 Hard Rescattering Model (HRM) diagram [21]. 22
3.7 $s^{11}\frac{d\sigma}{d\Omega}$ for the $d(\gamma,p)n$ reaction up to a photon energy of 4 GeV at $\theta_{cm} = 90°$. The the solid grey band is the result of the Hard Rescattering Model calculation [21]. Data are from Refs. [12, 13, 14, 15] 23
3.8 Quark Gluon String (QGS) Regge diagram [20]. 23
3.9 pQCD Feynman diagram for deuteron photodisintegration. 26
3.10 $\frac{d\sigma}{dt} \sim s^{-9.7\pm0.4}$ seen in proton-proton elastic scattering. Data are as compiled in Ref. [36]. 27

4.1 $s^{11}\frac{d\sigma}{d\Omega}$ for the $d(\gamma,p)n$ reaction up to E_γ=4.0 GeV. Data are from references [12, 13, 14] 35

5.1 Site map of the Thomas Jefferson National Accelerator Facility complex. 40
5.2 Schematic diagram of CEBAF superharps. 41
5.3 Schematic diagram of the cryogenic target stack. Note that in Hall C the long cell is only 12.5 cm. 48
5.4 Schematic diagram of a single cryotarget cell. Note that the cell long cell in Hall C was only 12.5 cm. 49
5.5 Schematic diagram of the $d(\gamma,p)n$ experimental setup. In Experiment E96-003 the target was 12.5 cm long, whereas in Experiment E99-008 the target was 15 cm long. 49

5.6 Schematic diagram of the Hall C HMS entrance collimator. 50
5.7 Schematic diagram of the HMS in Hall C. Q1, Q2, and Q3 are the three quadrupole magnets. 53
5.8 Schematic diagram of the HMS detector package. In the figure, DC1 and DC2 denote the two drift chambers and S1X, S1Y, S2X, S2Y denote the two pair of segmented, scintillator hodoscope planes. . . . 53
5.9 Schematic diagram of the HRS in Hall A. 54
5.10 Schematic diagram of HRS detector package. The verticle drift chambers are labeled **VCD** and **S1** and **S2** are the two hodoscope drift planes described in the text. 54
5.11 Schematic diagram of the HRS drift chambers. 55
5.12 Schematic diagram of the HMS drift chambers. 56
5.13 Example of a trigger electronics setup. This example is the Hall C single arm trigger. 61
5.14 Example diagram of the trigger supervisor electronics. This schematic diagram is for the Hall C trigger supervisor. 62

6.1 Schematic diagram of the HMS sieve mask. 65
6.2 Image of the Hall C HMS sieve mask at the target. 66
6.3 Reconstruction of the Hall A sieve mask at the target. 67
6.4 A comparison of elastic electron scattering from a proton target in the Hall C HMS, Monte Carlo (dashed line) to data (solid line). 68
6.5 A comparison of elastic electron scattering from a proton target in the Hall A HRS, Monte Carlo (dashed line) to data (solid line). 69
6.6 A gaussian fit to the elastic peak for the HMS at 2.060 GeV incident beam energy. 70
6.7 A gaussian fit to the elastic peak for the HRS at 856 MeV incident beam energy. 71

6.8 Mass squared peak normalized to proton mass for Experiment E96-003. These data were taken at a beam energy of $E_{beam} = 2.060$ GeV at a center-of-mass angle of $\theta_{cm} = 53°$. Notice the reasonably clear separation of protons and deuterons. 74

6.9 Mass squared plot, normalized to the proton mass for E_b=2500 MeV at θ_{cm}=143° for Experiment E99-008. Plots a-d are LD_2 radiator in, LH_2 radiator in, LD_2 radiator out, and LH_2 radiator out, respectively. Notice clear proton, deuteron, and a hint of triton peaks in the spectra. The deuteron and triton peaks are not at 4 and 9 respectively because of the time-of-flight calibration method. 75

6.10 Mass squared peak normalized to proton mass for Experiment E96-003. These data were taken at a beam energy of $E_{beam} = 5.566$ GeV and a center-of-mass angle $\theta_{cm} = 37°$. Notice there is no clear separation of protons from deuterons. 76

6.11 Mass squared peak normalized to proton mass for Experiment E99-008. These data were taken at a beam energy of $E_{beam} = 1.670$ GeV and a center-of-mass angle $\theta_{cm} = 37°$. Notice there is no clear separation of protons from deuterons. 77

6.12 Mass squared peak normalized to proton mass for Experiment E96-003. This is a background subtracted mass squared spectrum. Notice a clear proton peak with no apparent deuterons remaining. The fitted gaussian was used to determine the mass squared PID cuts used in the analysis. 77

6.13 Examples of the Y_{target} spectra at a) E_b=5.066 GeV at $\theta_{cm} = 70°$, the lowest momentum run in E96-003, and b) E_b=5.566 GeV at $\theta_{cm} = 37°$, one of the worst background cases. 78

6.14 Example Y_{target} from the Hall A HRS for E_b=1670 MeV at $\theta_{\mathrm{cm}} = 53°$. Figures a) and b) show the agreement of the LH_2 and LD_2 target spectra after scaling, as described in the text, for radiator in and radiator out respectively. Figure c) shows the result of the background subtraction in Y_{target}. 79
6.15 E_γ spectra for JLab Experiment E96-003 at E_b=5.566 GeV at $\theta_{cm} = 37°$. The three panels show the effects of adding analysis cuts to the data set. 81
6.16 E_γ spectra for JLab Experiment E96-003 at E_b=5.066 GeV at $\theta_{cm} = 37°$. The data are subtracted without any compensation for background in the kinematically forbidden region above the end point. . 83
6.17 E_γ spectra for JLab Experiment E96-003 at E_b=5.566 GeV at $\theta_{cm} = 37°$, top panel, and $\theta_{cm} = 53°$, bottom panel. The spectra are normalized to collected charge and are background subtracted as described in the text. The solid curve illustrates the clear end points in these spectra, as well as the threshold for π^0 production. The grey shaded area represents the region in E_γ used to calculate the photoproton yield. 84
6.18 E_γ spectra for E_b=1.670 GeV at $\theta_{cm} = 37°$, 90°, and 143°. 85
6.19 E_γ spectra for E_b=1.950 GeV at $\theta_{cm} = 37°$, 90°, and 143°. 85
6.20 E_γ spectra for E_b=2.5 GeV at $\theta_{cm} = 37°$, 90°, and 143°. 86
6.21 Examples of the Y_{target} spectra with data taken from the region of the E_γ spectrum which is kinematically forbidden. The data are from $E_b =$ 1.670 GeV at $\theta_{cm} = 143°$. Panel a) liquid deuterium target, radiator in; b) liquid deuterium, radiator out; c) liquid hydrogen, radiator in; and d) liquid hydrogen, radiator out. Notice the similar, position dependent pattern to the background. 88
6.22 An energy loss distribution for 5.566 GeV incident electron beam on a 4% copper target. 97

7.1 $s^{11}\frac{d\sigma}{d\Omega}$ for the $d(\gamma,p)n$ reaction up to E_γ=5.5 GeV. The present data are in filled diamonds. Previous data are from references [12, 13, 14] 107

7.2 Angular distribution of $s^{11}\frac{d\sigma}{dt}$ for $E_\gamma \approx$1.6 GeV. Notice the good agreement with the present data (filled upward facing triangles) with the previous data [12, 13, 14]. The solid curve is the Asymptotic Meson Exchange Model of Nagorny and Dieperink. The dashed curve is the RNA Model. 108

7.3 Angular distribution of $s^{11}\frac{d\sigma}{dt}$ for $E_\gamma \approx$2.4 GeV. Notice the reasonable agreement with the present data (filled upward facing triangles) with the previous data [12, 13]. The solid curve is the Asymptotic Meson Exchange Model of Nagorny and Dieperink. The dashed curve is the RNA Model. 109

7.4 Angular distribution of center-of-mass cross sections for $E_\gamma \approx$1.6 GeV. The solid curve is the Asymptotic Meson Exchange Model of Nagorny and Dieperink. The dashed curve is the RNA Model. 111

7.5 Angular distribution of center-of-mass cross sections $\frac{d\sigma}{d\Omega_{cm}}$ for $E_\gamma \approx 1.9$ GeV. The dashed curve is the RNA Model. 112

7.6 Angular distribution of center-of-mass cross sections $\frac{d\sigma}{d\Omega_{cm}}$ for $E_\gamma \approx 2.4$ GeV. The solid curve is the Asymptotic Meson Exchange Model of Nagorny and Dieperink. The dashed curve is the RNA model 112

7.7 Proton-proton elastic differential cross section plotted as $s^{-10}\frac{d\sigma}{dt}$ (R). Notice the appearance of oscillations about s^{-10}. Data are as compiled in Ref. [78]. The solid curve is the fit to the data as described in Ref. [78]. An earlier fit to the data is described in Ref. [79]. 117

A.1 Schematic diagram of a two body process $AB \to CD$. The labels A, B, C, D are particles with four momenta P_A, etc. 128

List of Tables

5.1 Radiator foil thicknesses for the Hall C radiator ladder. The foils are made up of a stack of thin foils, the thicknesses of which are given in the table. Table from Ref. [56]. 46

5.2 Technical specifications for the Hall C and Hall A cryotarget. Values for cold lengths and window thicnkess are from references [57, 58] . . 47

5.3 Technical specifications for the HMS and HRS. The HMS is a quadrupole, quadrupole, quadrupole, dipole spectrometer, while the HRS is a quadrupole, quadrupole, dipole, quadrupole spectrometer. Further information on the HMS is available in reference [59]. For more information on the HRS see reference [60] 51

5.4 Phototube types used in Halls A [66] and C [59]. 58

5.5 ADC and TDC types used in the Halls A [66] and C [59] (TDC model obtained from Ref. [12]) data acquisition electronics. 60

6.1 Absorbances of materials in the HRS and target materials other than cryogenic deuterium. Values for these materials are from reference [72]. 92

6.2 Absorbances of materials in the HMS and target materials other than cryogenic deuterium. Values for HMS and Target components were taken from reference [12]. 94

6.3 Center of mass and s^{11} scaled cross sections for Jefferson Lab Experiment E96-003. The errors are shown first stastical followed by systematic error. 102

6.4 Center-of-mass cross sections for Jefferson Lab Experiment E99-008. The errors shown are first statistical followed by systematic error. Measurements were not made for $\theta_{cm} = 26°$ at 1.95 and 2.5 GeV, due to spectrometer limitations. At $\theta_{cm} = 127°$ at 2.5 GeV, a support post for the target chamber obscured the target making the data unusable. The θ_{cm} values listed are at $E_{beam} = 1.670$ GeV. Values at the remaining energies vary only by a small amount. 102

6.5 Corrections applied to the data and systematic errors for Experiment E99-008. Center of mass angles are given in nominal values. 103

6.6 Corrections applied to the data and systematic errors for Experiment E96-003. Center of mass angles are given in nominal values. 104

Chapter 1

Introduction: Why Study Deuteron Photodisintegration?

Exclusive deuteron photodisintegration is a nuclear reaction which has been studied in a variety of experiments over the past seven decades. Exclusive deuteron photodisintegration (referred to from here on simply as deuteron photodisintegration) is a simple reaction which, because if its simplicity, is amenable to calculation. In this reaction a real photon, produced by bremsstrahlung, impinges upon a deuteron, which breaks up into its constituents a proton and a neutron (see figure 1.1).

Early experiments involving deuteron photodisintegration determined the binding energy of the deuteron, the only bound state of a proton and neutron, and estimating the neutron mass [1]. Studies performed over the past decade and a half have revealed a suprising result. In cross section measurements taken at the Stanford Linear Accelerator Center (SLAC) at 90° in the center of mass, asymptotic scaling consistent with perturbative quantum chromodynamics (pQCD) predictions set in at remarkably low incident photon energies [2, 3]. Further studies followed which attempted to find such scaling at forward angles to no avail [2, 4].

Nuclear reactions at intermediate energies, those which occur around a few GeV, then pose a challenge for nuclear physicists. Traditionally, nuclear reactions, like deuteron photodisintegration, are described using meson exchange current models (also called meson exchange models or MEC models). Meson exchange models use mesons and baryons to describe reactions. At very high energies, the techniques of pQCD are expected to become valid descriptions. For deuteron photodisintegration at few-GeV energies neither of these extremes appear to apply. Previous measurements have shown that above about 800 MeV incident photon energy meson exchange models break down and pQCD is not yet expected to be valid.

New measurements of the deuteron photodisintegration differential cross section were taken during Jefferson Laboratory experiments E96-003 and E99-008 the subject of this thesis. These experiments were designed to test two aspects related to describing nuclear reactions at intermediate energies. E96-003 was designed to investigate possible thresholds for the onset of asymptotic scaling at angles forward of 90° in the center of mass. During E99-008 a suite of angular distribution measurements were taken symmetric about 90° in the center of mass. The behavior of these measurements should provide insight into what framework the interactions of nucleons, neutrons and protons, with each other is most applicable.

The measurements taken during E96-003 have provided exciting new evidence for a threshold for the onset of scaling consistent with pQCD predictions. The angular distribution measurements of E99-008 show behavior not yet consistent with QCD inspired descriptions. They do, however, provide the first complete angular distribution at high energies.

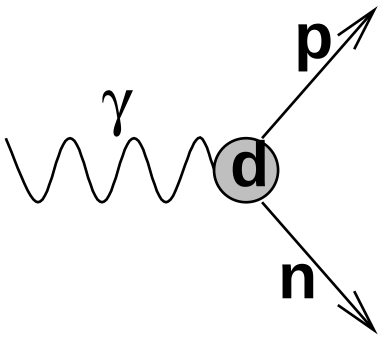

Figure 1.1: Schematic diagram of the exclusive deuteron photodisintegration reaction.

Chapter 2

Meson Exchange vs. QCD

Nuclei are strongly bound. But what does it mean to be strongly bound? This is a question which nuclear physicists struggled to answer for many decades. Protons are positively charged and neutrons are neutral, nevertheless, these two nucleons bind together to produce the nuclei present in everyday materials. Nuclei are clearly not bound though the electromagnetic force in the same way that electrons are bound in atoms. Nuclei must be bound together by some other force that is much stronger than the electromagnetic force. Thus, nuclei are said to be strongly bound.

Describing the strong force, then became a focus for nuclear physicists. With the advent of meson exchange theory, nuclei and nuclear reactions were analyzed in terms of models theories. In these models the exchange of various mesons mediates the reactions in the same sense that photons mediate the electromagnetic interaction. Further studies, using pion nucleon scattering [5], of mesons and baryons (the classification of particles into which nucleons fall) found that these particles are actually composite objects. Over time further studies were performed which led to the development of quantum chromodynamics [6] which describes mesons and baryons in terms of bound constituents, known as quarks and gluons, to characterize the strong force. Over the last several decades two pictures have emerged which can be employed to describe nucleon-nucleon interactions, like those which occur in deuteron photodisintegration. The question arises, which one should be used?

2.1 Meson Exchange Theory

Meson exchange theory is the classical technique used to describe nucleon-nucleon interactions. This technique was first postulated in 1934 by Hideki Yukawa [7] and is drawn in analogy to the very successful field theory of the electromagnetic force, Quantum Electrodynamics. Various exchange particles, mesons, are used in this technique to develop potential functions used to describe nucleon-nucleon interactions. This technique has been very successful at describing nucleon-nucleon interactions. For deuteron photodisintegration, however, at high energy its use has become limited.

Meson exchange theory was postulated in the 1930's and is based on the principles of Quantum Electrodynamics (QED) the field theory which describes the electromagnetic force [8]. Yukawa, in his theory devised a field theory equation,

$$\partial_\nu^2 \Phi - \mu^2 \Phi = -4\pi\eta(\vec{r}, t), \tag{2.1}$$

where Φ is a scalar field, μ^2 has unit length^{-2}, and $\eta(\vec{r}, t)$ is the source strength [9]. This is analogus to the QED field equation,

$$\partial_\nu^2 \psi = -\frac{\rho(\vec{r}, t)}{\epsilon_\circ}, \tag{2.2}$$

where ψ is a scalar field and $\rho(\vec{r}, t)$ is the electromagnetic charge distribution, and $\epsilon_\circ$ is the permittivity of free space. The additional term $-\mu^2\Phi$ in Eq. 2.1 describes the finite range of the strong force. The solution of Eq. 2.1 leads to the Yukawa potential between two point sources,

$$V = -g^2 \frac{e^{-\mu\mathcal{R}}}{\mathcal{R}}, \tag{2.3}$$

where $\mathcal{R} = |\vec{r_1} - \vec{r_2}|$ and g is the coupling constant analogous to e in QED [9]. Thus, Yukawa developed a field theory which could be applied to understanding the strong nature of nucleon-nucleon interactions.

As a result of the short range of the Yukawa potential, given by μ in Eq. 2.3, the exchange particles in Yukawa's theory must be different from photons, which govern QED. These exchange particles are massive, with masses found from Compton's formula [8]

$$\mu = \frac{\hbar}{mc}. \tag{2.4}$$

Yukawa predicted the mass of these particles from experimental evidence of the range of the nuclear force [8]. He estimated these exchange particle masses to be about 100 MeV. Because they were heavier than electrons, called leptons ("light-weight"), but lighter than the "heavy-weight" baryons (neutrons and protons) Yukawa called these new exchange particles mesons, "middle-weight." Mesons with the characteristics described by Yukawa were later found in cosmic ray studies and are known as pions (π) [9]. Other mesons have also been discovered and used to describe nucleon-nucleon interactions. As a result Yukawa's theory of nuclear forces led the way to modern meson exchange theories.

Various other potentials have been developed over time using the basic ideas begun by Yukawa in his theory. This method has been very successful describing nuclear physics data. Increased sophistication allowed the meson exchange technique to be applied at higher and higher energies. For deuteron photodisintegration such models work very well up to incident photon energies of about 500 MeV (Fig. 2.1). Figure 2.1 shows the scaled invariant differential cross section, $s^{-11}\frac{d\sigma}{dt}$, for the deuteron photodisintegration reaction as a function of the incident photon energy. The variables s and t are the Mandelstam variables, and their definition can be found explicitly in Appendix A. In Fig. 2.1 the two models of deuteron photodisintegration presented up to about 500 MeV are able to reproduce features in the data quite well. For photon energies above 500 MeV, however, they begin to lose their predictive power.

Meson exchange theory, introduced by Yukawa in the 1930's, was a revolutionary method for viewing the strong nature of nuclear forces. Developed in analogy to Quantum Electrodynamics, Yukawa's theory predicted a massive exchange particle for the nuclear force. These particles of approximately 100 MeV mass were given the name meson because their mass was between that of the electron and nucleon. Meson exchange proved a powerful method for describing deuteron photodisintegration, but

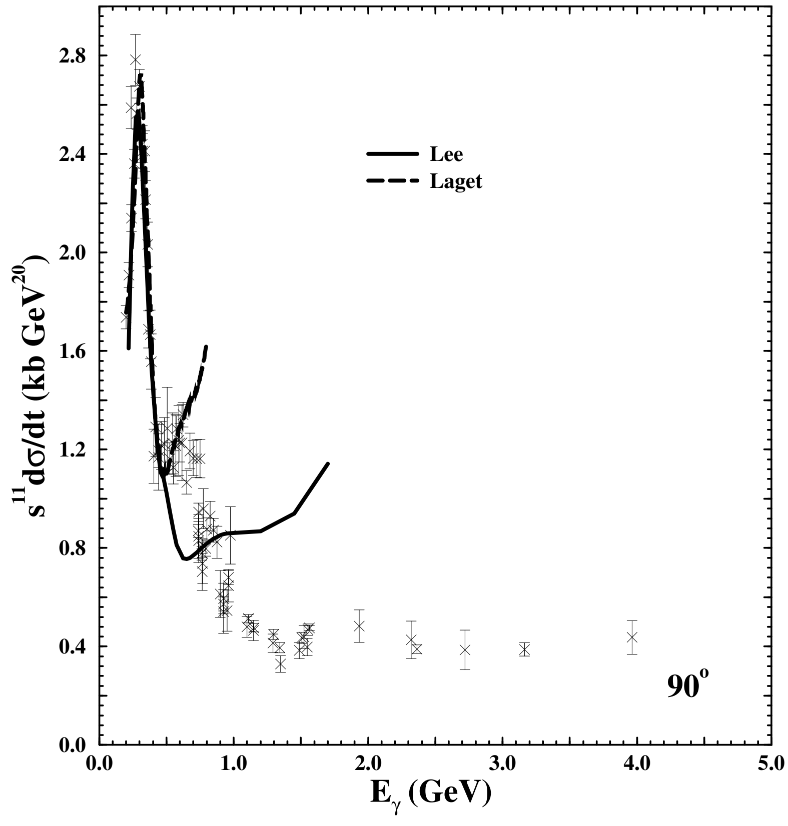

Figure 2.1: $s^{11}\frac{d\sigma}{d\Omega}$ for the $d(\gamma,p)n$ reaction up to a photon energy of 4 GeV at $\theta_{cm} = 90°$. The the solid curve is the meson exchange model developed by T.S-H. Lee [10] and the long dashed curve is the meson exchange model developed by Laget [11]. Notice that above 0.5-0.8 GeV the present models are unable to reproduce the present data. The data appear to follow an s^{-11} dependence. Data are from Refs. [12, 13, 14, 15]

at high photon energies, above about 500 MeV, it is a technique which appears to lose its descriptive capability. Resolving this difficulty requires consideration of a much more complete picture of meson-baryon interactions including all possible excited states of the nucleon and all meson exchanges or another picture of strong interactions, quantum chromodynamics.

2.2 Quantum Chromodynamics

Quantum chromodynamics is a field theory approach to the strong interaction. Quantum chromodynamics (QCD) views the hadrons, baryons and mesons, as composite objects of point like particles called quarks. Quarks introduce a new quantum number, analogous to charge, called color. Because the coupling constant for QCD, α_s, is strongly dependent on momentum transfer, perturbative methods like those used in QED are only valid at large momentum transfers. QCD is expected to be able to describe nuclear interactions, like deuteron photodisintegration; however, α_s is still relatively large even at the highest energies so far measured in deuteron photodisintegration, perturbative approaches are not expected to be valid and non-perturbative techniques are very difficult to calculate.

Quantum chromodynamics (QCD) describes the hadrons, mesons and baryons, in terms of point-like constituents called quarks. Each baryon has three valence quarks and each meson is composed of a quark and an antiquark [5]. Quarks were postulated to explain the spectroscopy of the baryons [16].

Quarks are spin $\frac{1}{2}$, fermions, which carry fractional electric charge. Therefore, they interact electromagnetically. There were some inconsistencies, however, with using quarks to describe all of the observed baryons. For example, to explain the correct charge and angular momentum of the Δ^{++}, Fermi stastistics had to be violated [5]. A solution to this problem was found by introducing a new quantum number.

To resolve the Fermi stastictics problem a new quantum number, known as color, was introduced. Each quark carries a unit of "color charge" [5] red, green, or blue. Thus the quarks are distinguishable from the leptons by color, the leptons are colorless [17]. The hadrons are also colorless. Therefore, the quarks must interact to form colorless objects [5]. Quarks interact with each other strongly. Photons only interact with quarks electromagnetically, therefore, some other interaction particle must be responsible for strong interactions. A massless boson called the gluon is responsible for carrying the color field. Gluons interact with quarks much the same way that photons interact with leptons. One important exception exists. Gluons carry a "charge" of color. Therefore, they interact not only with quarks but also with each other. This adds complexity to QCD calculations.

QCD exhibits asymptotic freedom. This is a quality of the non-Abelian nature of QCD. In theories which are asymptotically free, the coupling constant decreases with increasing momentum [17]. In order for perturbative methods to be of any use in calculating interactions in QCD, α_s, the coupling constant must be small. The strong coupling constant takes the following form [5]:

$$\alpha_s(Q^2) = \frac{2\pi}{(33 - 2n_f)\log(Q^2/\Lambda^2_{QCD})} \tag{2.5}$$

where Λ_{QCD} is a charasteric scale, n_f is the number of quark flavors, and Q^2 is the momentum transfer in the interaction. For α_s to be small the $\log(Q^2/\Lambda^2_{QCD})$ term of Eq. 2.5 must be large; or the momentum transfer must be large compared to Λ^2_{QCD}. The cutoff Λ_{QCD} is estimated experimentally to be between 0.1 and 0.5 GeV [5]. For deuteron photodisintegration the momentum transfer important in the problem is the momentum transfer per nucleon t_N. This momentum transfer is found by [18]:

$$t_N^{\gamma d \to pn} = -2m_N T_N \tag{2.6}$$

where T_N is the kinetic energy of the recoil nucleon. For T_N=5 GeV, a kinetic energy reached in the new high energy data, α_s values are of order 0.5. For scale, compare this value to the value of α used in QED, $\frac{1}{137}$. The value of α_s is not very small. Therefore, it is not naïvely expected that perturbative techniques should be applicable even up to 5.5 GeV photon energy for deuteron photodisintegration.

Quantum chromodynamics is a field theoretical approach to describing strong interactions. QCD views the hadrons, baryons and mesons, as a composite of objects called quarks. Quarks are the fractionally charged, point-like elementary particles of QCD. To avoid problems with Fermi stastictics, QCD introduces a new quantum number called color. Color can be viewed as the "charge" of strong interactions. The color field is carried by massless bosons known as gluons. Gluons are "charged" with color, as such they can interact with each other. QCD descriptions of nuclear interactions are most simply calculated in the regime where perturbative techniques are applicable; however, the form of the coupling constant, α_s, restricts this regime to very high momentum transfers. Even at typical momentum transfers for high energy deuteron photodisintegration, α_s is still not sufficiently small to expect that perturbative techniques should be valid.

Chapter 3

Available Descriptions of Deuteron Photodisintegration

As described in Chapter 2, there are two basic frameworks which can be used to describe deuteron photodisintegration. The meson exchange picture has produced very successful models up to a few hundred MeV in photon energy. Two models, one by T.-S. H. Lee and one by J.M. Laget, have attempted to describe deuteron photodisintegration into the 1 to 2 GeV region. Because pQCD, the extreme case of QCD where interactions are most easily calculable, is not expected to be a valid technique for describing deuteron photodisintegration in the few GeV region, several approaches have been developed to try to reconcile these extremes. The Asymptotic Meson Exchange model attempts to modify the traditional meson exchange technique by employing short range deuteron wave functions to describe the short distance behavior of the reaction. Models which include QCD concepts and involve single quark exchanges, such as Reduced Nuclear Amplitudes [19], a Regge model known as Quark Gluon String [20], and the Hard Rescattering Model [21]also exist. Pertubative QCD, the high energy extreme, provides a very simple expression to predict the deuteron photodisintegraton cross section known as the Constituent Counting Rules [22]. The following sections in this chapter will summarize the important features of each of these techniques, and what they predict for the energy and angular dependencies for the differential cross section.

3.1 Traditional Meson Exchange

3.1.1 Lee's Model

The meson exchange model developed by T.-S. H. Lee calculates the differential cross section for deuteron photodisintegration only at 90° in the center of mass. This model describes the reaction occuring in two parts involving photon absorption and subsequent nucleon-nucleon interaction. A coupled channel model for nucleon-nucleon interactions is used to characterize the final state interaction. A relativistic approach has also been taken, with little effect on the model's high energy predictive power.

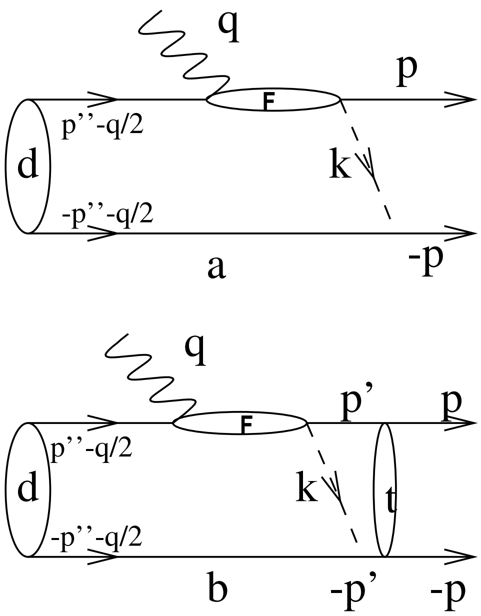

Figure 3.1: Diagram of Lee's meson exchange current model. Figure a) shows the basic model being studied. Figure b) shows detail of the nucleon-nucleon final state interaction described in the model. The "bubble" in b) represents the half-off shell t-matrix governing the final state nucleon-nucleon interaction [10].

This model, a diagram of which is shown in figure 3.1, is broken into two parts [10]:

1. a photon is absorbed on a nucleon which may, in the deuteron, excite into a resonance and mesons are exchanged.

2. the outgoing nucleons interact *via* meson exchange.

As a result the following three processes must to be calculated [10]:

1. The $\gamma + N \to N+$ mesons off shell amplitude (F in Fig. 3.1)

2. The "half off-shell" t matrix governing the nucleon-nucleon final state interaction

3. The absorption of the emitted mesons.

The calculation of F, the meson production piece, is well described by a Born term, a Δ resonance and an $N^*(1470)$ resonance term. Both single pion and two pion exchange are included in the meson production where the two pion piece describes two-pion production [10]:

$$\gamma N \to N^* \to \pi\Delta \to \pi\pi N. \tag{3.1}$$

The resulting resonance and the emitted mesons participate in the final state interaction.

The final state nucleon-nucleon interaction is described with a coupled channel model. That is, a set of coupled differential equations such as [23]

$$\left(\frac{p^2}{2\mu_{NN}} + V_{NN} - E\right)\psi_{NN} = -V_{NN,N\Delta}\psi_{N\Delta} \tag{3.2}$$

$$\left(\frac{p^2}{2\mu_{N\Delta}} + M_\Delta - M + V_{N\Delta} - E\right)\psi_{N\Delta} = -V_{N\Delta,NN}\psi_{NN} \tag{3.3}$$

must be solved in order to obtain a description of the reaction. In Eqs. 3.2 and 3.3, $\mu_{NN(\Delta)}$ is the reduced mass of the $NN(\Delta)$ system, $M(M_\Delta)$ is mass of the nucleon

(Δ), $V_{NN(\Delta)}$ are diagonal potentials, and $V_{NN,N\Delta}$ are transition potentials. Lee's approach extends the Paris potential to include the Δ and $N^*(1470)$ resonances in a coupled channel approach [10] which provides a reasonable description of the phase shift data [24]. The Paris potential is a two-nucleon potential derived from meson exchange theory concepts [25]. The meson absorption is described by a form factor

$$\frac{\Lambda^2 - \mu^2}{q^2 + \Lambda^2} \tag{3.4}$$

which regulates the short distance behavior. In Eq. 3.4 μ is the pion mass, q is the relative pion-nucleon momentum and Λ is a parameter which can be fit. Values for the parameter Λ typically range from 650 MeV/c to 1000 MeV/c [24]. Cutoff values of this momentum correspond to a distance scale of approximately 0.3 to 0.2 fm. This model is constrained by data in the γN, NN, and low energy deuteron photodisintegration reactions.

A relativistic front-form approach has also been tried. In this approach the Hamiltonian is expressed as

$$H = \frac{m^2 + \vec{P}_T^2}{P^+} \tag{3.5}$$

where $\vec{P}_T = (P_1, P_2)$, $P^+ = (P_0 + P_3)$, and m is the mass operator [26]. This method was also evaluated using the Paris potential, however, the effect on the predictive power of the model was not very great [10].

T.-S. H. Lee developed a model of the deuteron photodisintegration, but only predicted values of the differential cross section at 90° in the center of mass. As seen in Fig. 2.1 the model describes the cross section very well below 0.7 GeV, but fails above this energy. Both a relativistic and non-relativistic approach were taken with no significant difference between them. The non-relativistic model uses a coupled channel approach to describe the nucleon-nucleon final state reaction. This is the second of two primary pieces of the model. The first describes the absorption of a photon on a nucleon.

3.1.2 Laget's Model

J. M. Laget also developed a meson exchange current model of deuteron photodisintegration. This model, also only calculated the cross section at 90° in the center of mass, expands the cross section in terms of leading amplitudes. As shown in Fig. 2.1, the results of this calculation indicate good agreement up to a photon energy of approximately 0.7 GeV, after which the description begins to break down. In this model the photon is allowed to couple explicitly to the exchanged meson. Form factors are used to reproduce the correct cross section values.

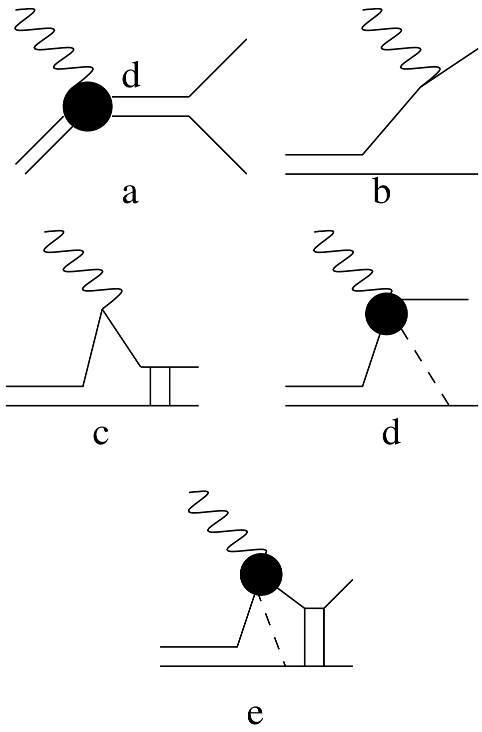

Figure 3.2: Leading diagrams for Laget's model a) the deuteron pole; b) the nucleon pole; c) nucleon-nucleon rescattering; d) pion reabsorption; e) pion reabsorption followed by NN scattering. [11]

Laget's model expands the deuteron photodisintegration cross section in terms of leading amplitudes (see Fig. 3.2). The first is the nucleon pole amplitude, in which the photon couples to one or another of the nucleons. The photon can couple directly to the deuteron; this is the deuteron pole amplitude. Also necessary are a nucleon-nucleon rescattering amplitude and an amplitude describing the reabsorption of the produced meson, including Delta (Δ) resonance production [11].

In this model the photon can couple directly to the exchanged meson. A nucleon can emit a meson, like the pion. This meson can then travel far off the mass shell; that is, become a virtual meson. The photon couples to this virtual meson before it is reabsorbed. In this way Laget explicitly couples photons directly to the meson currents [11].

To properly reproduce the cross sections, form factors, mathematical constructions used to describe composite objects [27], are needed at each meson-baryon vertex [11]. Laget allows for the exchange of rho (ρ) and pi (π) mesons. As in Lee's model, each πNN or $\pi\Delta N$ vertex a form factor of monopole form is used:

$$F_\pi(q^2) = \frac{\Lambda_\pi^2 - m_\pi^2}{\Lambda_\pi^2 - q^2}. \tag{3.6}$$

In Eq. 3.6 Λ_π is the cutoff mass and ranges from 1 GeV $< \Lambda_\pi <$ 1.2 GeV [11]. A dipole form factor is used at each $\rho\Delta N$ and ρNN vertex:

$$F(q^2) = \frac{\Lambda_\rho^2 - m_\rho^2}{\Lambda_\rho^2 - q^2}. \tag{3.7}$$

In Eq. 3.7 the cutoff mass $\Lambda_\rho = 2m$ where m is the mass of the ρ [11], as determined by from analysis of electromagnetic form factors.

Laget's model is based upon meson exchange. Form factors at each meson-baryon vertex are needed to correctly describe the cross section data. In this model the incoming photon is allowed to couple directly to a produced meson. The deuteron photodisintegration amplitude is expressed as an expansion of leading amplitudes. The Reid soft core wave function [28] is used to evaluate the associated matrix elements. The model predicts an absolute cross section.

3.2 Asymptotic Meson Exchange (AMEC)

Nagorny, Dieperink, and their collaborators have devised a model [29] which attempts to extend the meson exchange concept into the few GeV photon energy region. They argue that it is not suprising that traditional meson exchange models are unsuccessful because of the short distances over which the reaction occurs. In Asymptotic Meson Exchange the short distance part of the interaction is parametrized with a strong form factor. Because the hard part of the reaction occurs over short distances, relativistic prescriptions are taken. Asymptotic Meson Exchange gives mixed results in describing the energy dependence at all energies, and angles.

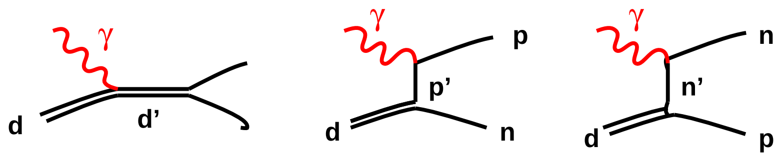

Figure 3.3: Asymptotic Meson Exchange Mode (AMEC) diagrams [29].

Nagorny, *et al.*, argue that failure of traditional meson exchange techniques to reproduce the deuteron photodisintegration data in the few GeV region is not unexpected [29]. At photon energies over 1 GeV, the reaction occurs over distances of about 0.2 fm. As a result the AMEC prescription is divided into two main parts, a "soft" part described by traditional meson exchange techniques, and a "hard" or short range part which accounts for this new non-traditional phenomena [29].

The primary diagrams contributing to this model are shown in Figure 3.3. The short distance behavior, or "hard" part, of the process is described by a strong form factor of the following type:

$$G(p^2) = \frac{C}{(\Lambda^2/2 + m^2 - p^2)^g}. \tag{3.8}$$

Form factors of this type are obtained from constraining the form factor to reproduce the asymptotic behavior of the basis model [30]. In Eq. 3.8, C is a normalization constant, Λ is a "range parameter," m is the nucleon mass, and p the momentum of the off-shell nucleon [29]. Nagorny, *et al.* have used $g = 3$ to describe the data between 1 GeV and 4 GeV photon energies [29].

Relativistic effects are important at short distances. As a result the authors transformed their prescription into light-front and instant form relativistic prescriptions. In these prescriptions the form factor is transformed into the appropriate coordinate systems.

The instant-form form factor is expressed as [29]:

$$G^{if}(-k_i^2) = \frac{C}{(\delta^2 - k_i^2)^g}. \tag{3.9}$$

In Eq. 3.9 the index i runs across the three Mandelstam variables s, t, and u. The values k_i^2 are expressed as [29]:

$$k_t^2 = -\alpha \vec{k}^2 \tag{3.10}$$

$$k_u^2 = -(2-\alpha)\vec{k}^2 \tag{3.11}$$

$$k_s^2 = -\vec{k}^2 \tag{3.12}$$

$$\vec{k}^2 = -\alpha \vec{k}^2. \tag{3.13}$$

The values α and δ are:

$$\alpha = 1 - \frac{k}{E_k}\cos\theta_{cm} \tag{3.14}$$

$$\delta = \frac{\Lambda^2}{4} + \alpha_0^2 \tag{3.15}$$

$$\alpha_0 = m^2 - \frac{m_d^2}{4}. \tag{3.16}$$

There is one $G^{if}(-k_i^2)$ for each of the s, t, and u vertices. Two values of the exponent g were explored, $g = 3$ and 4, with $g = 3$ giving the best energy dependence. This, however, produces a very steep angular distribution due to the combination of α and $\vec{k}_i^2$ terms in $G^{if}(-k_i^2)$ [29].

The light-front prescription transforms $G(p^2)$ (Eq. 3.8) into the following form [29]:

$$G^{lc}(\alpha, k^2) = \frac{C}{(\beta^2 - \vec{k}^2)^g}\phi_\kappa(\alpha). \tag{3.17}$$

In Eq. 3.17 $\phi_\kappa(\alpha) = \alpha^{-\kappa}$ where α and $\vec{k}^2$ are given in Eq. 3.9. The exponent κ takes on two values such that $\phi_\kappa(\alpha) \to 0$ in the non-relativistic limit: $\kappa = 0$ and $\kappa = \frac{1}{2}$. This formalism separates the s and $\cos\theta_{cm}$ terms. Therefore, the strengths of the s dependence and θ_{cm} dependence are independent and a strong s dependence and softer angular dependence is possible [29].

The Asymptotic Meson Exchange model is designed to extend the concepts of traditional meson exchange current theory into the few GeV energy regime. A light-front prescription of the model describes the energy dependence and softly rising, asymmetric angular dependence about 90° in the center of mass, as seen in previous measurements, better than the instant form relativistic prescription does. AMEC uses a strong form factor to describe the short range part of the reaction, which, it is argued, is not properly described in non-relativistic meson exchange theory.

3.3 Reduced Nuclear Amplitudes/Quark Exchange

Reduced Nuclear Amplitudes (RNA) developed by Brodsky and Hiller and Quark Exchange, developed by Radushkin, are related methods to describe the deuteron photodisintegration differential cross section. This method is based upon the reduced form factor technique developed by Brodsky and Chertok. In the reduced amplitude technique the transverse momentum, P_T, is the kinematic quantity which governs the onset of asymptotic scaling. The formalism devised by Radushkin clearly illustrates the symmetric nature of the angular distribution predicted by this technique.

Brodsky and Chertok developed the reduced form factor to describe the electron-deuteron elastic form factor (see Fig. 3.4) [19]. The reduced form factor is given by [31]

$$f_d = \frac{F_d(q^2)}{F_N^2(\frac{1}{4}q^2)}. \tag{3.18}$$

In Eq. 3.18 F_d is the deuteron form factor and F_N^2 is the product of two nucleon form factors. Each nucleon is assumed to carry $\frac{1}{4}|q|^2$, the momentum transfer squared to

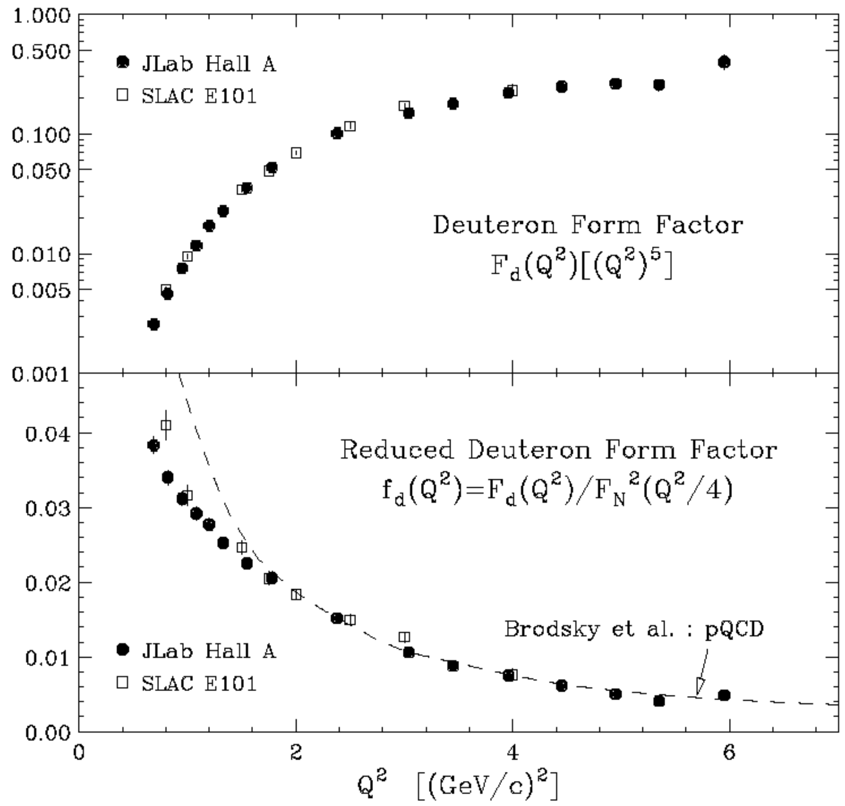

Figure 3.4: Recent electron-deuteron elastic structure function results from Jefferson Lab Hall A. The figure is from Ref. [32]. The top panel shows the deuteron form factor F_d multiplied by the Q^2 dependence expected from pQCD predictions. The bottom panel shows the reduced form factor analysis from the RNA method. The dashed curve is the RNA prediction [33].

the deuteron. By using the reduced form factor, the nuclear structure is effectively removed from the problem [31]. The nucleon form factors are found by:

$$F_N(q^2) = \frac{C_N}{(1 - q^2/0.71)^2} \tag{3.19}$$

The constant C_N is a normalization constant and the value 0.71 (GeV^2) was found by fitting nucleon form factor data [31]. Brodsky and Hiller in the RNA for deuteron photodisintegration model give the expression for the general reduced scattering amplitude as [19]:

$$m(s,t) = \mathcal{M}(s,t)\{\prod_{i=1}^{A} F_N(\hat{t}_i = q_i^2)\}^{-1} \tag{3.20}$$

where q_i is the momentum transferred to each nucleon. For deuteron photodisintegration

$$m_{\gamma d\to pn} = \frac{\mathcal{M}}{F_n(\hat{t}_n)F_p(\hat{t}_p)} \tag{3.21}$$

where

$$\hat{t}_n = (p_n - \frac{1}{2}p_d)^2 \tag{3.22}$$
$$\hat{t}_p = (p_p - \frac{1}{2}p_d)^2 \tag{3.23}$$

where $p_{p(n,d)}$ is the proton(neutron, deuteron) four momentum and the form factors $F_N(\hat{t}_N)$ are given in Eq. 3.19 [19].

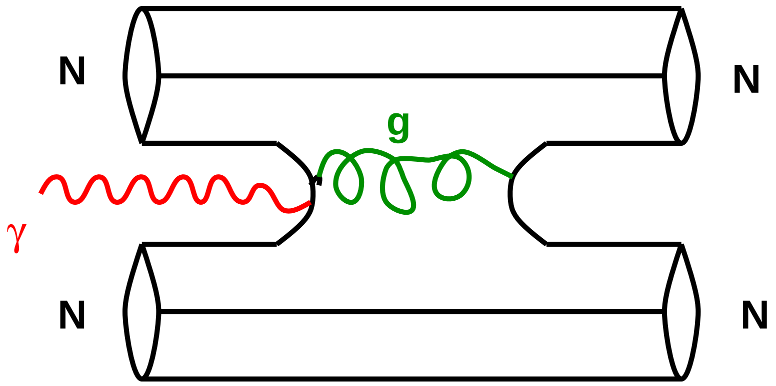

Figure 3.5: Quark Exchange Model [34].

By analogy with the electron-deuteron (e-d) elastic form factor, for which scaling sets in at $Q^2 = 1$ (GeV/c)^2, any scaling behavior for deuteron photodisintegration is argued to set in for momentum transfers, in this case P_T of approximately 1 GeV/c. Using this assumption the scaling condition for deuteron photodisintegration is:

$$P_T m_{\gamma d\to pn} \simeq \text{constant;. } P_T^2 \geq 1 \text{ (GeV/c)}^2 \tag{3.24}$$

The amplitude $m_{\gamma d\to pn}$ can be factored into an energy/momentum-dependent piece and an angular-dependent piece,

$$m_{\gamma p\to pn} = P_T^{-1} f(\theta_{cm}), \tag{3.25}$$

where $P_T^{-1} = tu/s$ (see Appendix A for the definition of u) up to logarithmtic terms, if particle masses are ignored [19]. From this the center of mass differential cross section can be constructed:

$$\frac{d\sigma}{d\Omega_{cm}} \sim \frac{1}{s[s-m_d^2]^{\frac{1}{2}}} \frac{F_p^2(\hat{t}_p)F_n^2(\hat{t}_n)}{P_T^2} f^2(\theta_{cm}). \tag{3.26}$$

Radushkin reformulated the expression of the form factors in his Quark Exchange model. A diagram of these models can be seen in Figure 3.5. Radushkin describes the amplitude in terms of energy and scattering angle in the center of mass [34]:

$$M(E,\theta_{cm}) = \frac{f^{SD}(E,\theta_{cm})}{(\mu + mE)^4} C(E,\theta_{cm}) \tag{3.27}$$

where $C(E,\theta)$ is given by,

$$C(E,\theta) = \left[1 - \frac{\cos^2\theta_{cm}}{(1+\frac{m}{E})(1+\frac{\mu^2}{mE})^2}\right]^4, \tag{3.28}$$

where $\mu^2 = 0.71$ GeV^2, E is the laboratory photon energy, and m is the nucleon mass. From these expressions a symmetry about 90° in the center of mass, given by the $\cos^2\theta$ term, in the angular distribution of the cross section can be seen.

The Reduced Nuclear Amplitudes and Quark Exchange Models are very similar in principle. The reduced amplitude technique was developed by Brodsky and Chertok to remove nuclear structure from calculations of the electron-deuteron form factor. RNA predicts the onset of scaling behavior at $P_T \geq 1$ GeV/c, consistent with the e-d elastic form factor measurements. The formulation given by Radushkin shows the symmetric nature of the angular distribution about 90° in the center of mass, predicted by this technique.

3.4 Hard Rescattering Model

The Hard Rescattering Model, illustrated in Figure 3.6, allows a photon to be absorbed on a quark. This results in a high momentum scattering of the struck quark

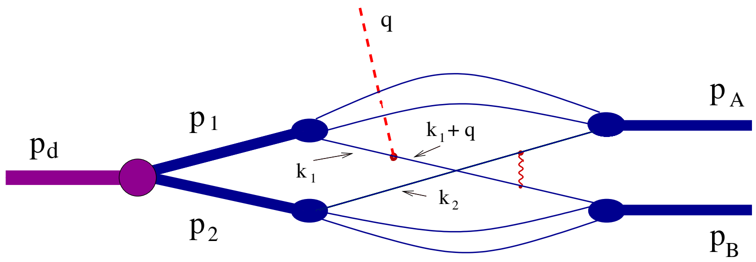

Figure 3.6: Hard Rescattering Model (HRM) diagram [21].

on a quark in the other nucleon. The residual nucleons have high relative momentum after the reaction [21]. A low-momentum, non-relativistic deuteron wave function, Ψ_d^{NR}, is used to describe the initial deuteron. The use of the low momentum wave function is necessary because the deuteron is loosely bound. The quarks which interchange in the reaction do so by exchanging a hard (high energy) gluon; and, the struck quark must not radiate any soft gluons before reaching the second quark [21].

The quark interchange piece of this model is parametrized by using high energy, large angle, proton-neutron scattering data. Because little data are available at the momentum transfer per nucleon, t_N, values needed, $\frac{d\sigma^{pn\to pn}}{dt}$, was extrapolated to appropriate values. The proton-neutron cross section already scales as s^{-10}, so the requirement that $\frac{d\sigma^{\gamma d\to pn}}{dt}$ scale as s^{-11} at high energies is naturally met [21]. The final expression for the differential cross section takes the following form [21]:

$$\frac{d\sigma^{\gamma d\to pn}}{dt} = \frac{4\alpha}{9}\pi^4\frac{1}{s'}C(\frac{t_N}{s})\frac{d\sigma^{pn\to pn}}{dt} \times \left|\int \Psi_d^{NR}(p_z = 0, p_\perp)\sqrt{m_N}\frac{d^2p_\perp}{(2\pi)^2}\right| \tag{3.29}$$

In Eq. 3.29 $C(\frac{t_N}{s}) \approx 1$ at $90°$ in the center of mass, and is taken equal to 1 in the calculation. Ψ_d^{NR} is the Paris potential wave function, $s' = s - M_d^2$, $\alpha = \frac{p_{1+}}{p_{d+}}$, where $p_{i+} = (p_{i0} + p_{i3})$, and $p_\perp = p_{1\perp} = -p_{2\perp}$, where $p_{i\perp} = (p_{i1}, p_{i2})$. The quantities p_i denote the outgoing nucleons' momenta, and p_i1 and p_i2 are the x and y components of the momentum vectors. Because of the parametrization of the quark rescattering by proton-neutron scattering data, the description is an uneven band in Fig. 3.7.

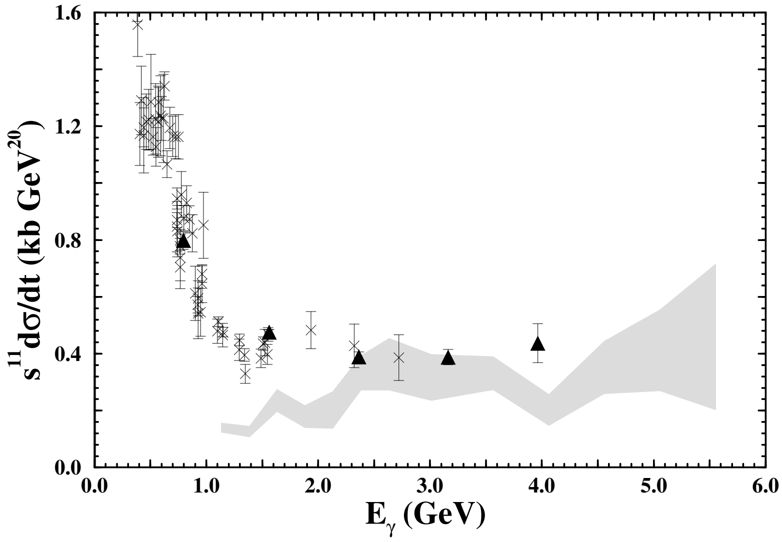

Figure 3.7: $s^{11}\frac{d\sigma}{d\Omega}$ for the $d(\gamma,p)n$ reaction up to a photon energy of 4 GeV at $\theta_{cm} = 90°$. The the solid grey band is the result of the Hard Rescattering Model calculation [21]. Data are from Refs. [12, 13, 14, 15]

3.5 Quark Gluon String

The Quark Gluon String model uses Regge theory to calculate the deuteron

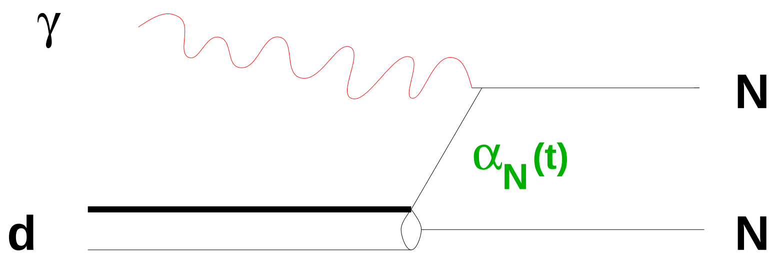

Figure 3.8: Quark Gluon String (QGS) Regge diagram [20].

photodisintegration cross section. A diagram of this model is given in Fig. 3.8. Phenomenological Regge trajectories, $\alpha(t)$, have the form [20]

$$\alpha_N(t) = \alpha_N(0) + \alpha'_N(0)t + \frac{1}{2}\alpha''_N(0)t^2K(t) \quad (3.30)$$

where (3.31)

$$K(t) = e^{-\beta t^2} \quad (3.32)$$

and the K(t) term in Eq. 3.31 is needed to prevent the violation of unitarity. This model, however, uses non-linear trajectories which are derived from QCD studies. These trajectories are parametrized [20]

$$\alpha(t) = \alpha(0) + \gamma[T^{\nu} - (T-t)^{\nu}] \tag{3.33}$$

where $0 \leq \nu \leq \frac{1}{2}$, and T is the non-linearity parameter. The trajectory follows from the screened quark-antiquark potential $V(R)$:

$$V(R) = \left[\frac{-\alpha}{R} + \sigma R\right] \frac{1 - e^{-\mu R}}{\mu R}. \tag{3.34}$$

The authors studied the extreme cases where $\nu \to 0$, which gives a logarithmic dependence on T,

$$\alpha(t) = \alpha(0) - \gamma\nu \log((1 - \frac{T}{t}), \tag{3.35}$$

and where $\nu = \frac{1}{2}$ which gives a square root dependence [20],

$$\alpha(t) = \alpha(0) + \gamma\left[\sqrt{T} - \sqrt{(T-t)}\right]. \tag{3.36}$$

The quark-antiquark model was extended to baryons in order to apply the QGS to deuteron photodisintegration. This was accomplished by describing a baryon as a composite object containing a quark and a diquark. This allows the baryon trajectories to take a similar form as the quark-antiquark systems studied in lattice QCD calculations which formed the basis for the non-linear trajectories [20]. The trajectories $\alpha(t)$ are then used to calculate the differential cross section for the deuteron photodisintegration reaction. Leaving T as the free parameter and setting the slope and intercept found from the phenomenological trajectory (Eq. 3.31), the authors found that the logarithmic form provides the best description of the data up to 4 GeV. The parameters used in calculating the deuteron photodisintegration cross section are found by fitting to various data sets, such as $pp \to \pi^+ d$ and even high energy deuteron photodisintegration data at the most forward angle, 36° in the center of mass [20].

The Quark Gluon String Model also provides a prediction for the angular distribution of the differential cross section. The authors used two approaches. The first was assuming that the incoming photons were isovector only. This produced a symmetric distribution about 90° in the center of mass. This is inconsistent with the available data at approximately 1.6 GeV photon energy. By including an isovector-isoscalar photon interference term, the model is able to produce an asymmetric angular distribution [20]. This model does not, however, predict an absolute cross section.

3.6 Perturbative Quantum Chromodynamics–Constituent Counting Rules

Processes in quantum chromodynamics are most simply calculated in energy or distance scales where perturbative methods can be applied akin to their application in Quantum Electrodynamics. The nature of the running coupling constant, $\alpha_s(Q^2)$, requires high energies for perturbation theory to be valid. At perturbative energy scales, however, a simple prescription exists to predict the behavior of invariant differential cross sections. Behavior consistent with these rules, known as Constituent Counting Rules, has been seen in high-energy hadronic processes.

Perturbation theory can only accurately be applied to a process when the scales of the problem are small and higher orders in the expansion are smaller than preceding orders. In both Quantum Electrodynammics (QED) and QCD the coupling constant, the important scale in the problem, changes with momentum transfer squared (Q^2). In QED $\alpha(Q^2)$ increases with increasing Q^2. In QCD, however, because the exchange bosons, gluons, have self interactions, the strong coupling constant $\alpha_s(Q^2)$ decreases with increasing Q^2 (see Section 2.2) [22]. Brodsky and Lepage argue that because Λ_{QCD}, the cutoff in Eq. 2.5, is between 100 MeV and 300 MeV from experiment pQCD could be valid for hadronic distances as large as 1 fm [22]. Using this argument it may be possible to apply a pQCD method to describe medium as well as high energy processes.

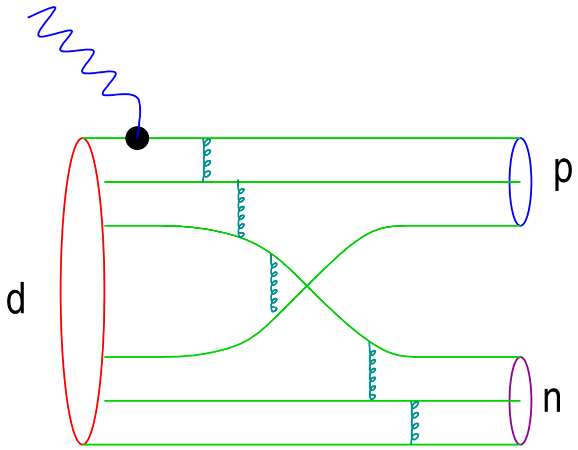

Figure 3.9: pQCD Feynman diagram for deuteron photodisintegration.

The Constituent Counting Rules, sometimes called dimensional scaling laws, were developed by Matveev, Muradyan, and Tavkhelidze and Brodsky and Lepage independently. A diagram describing the pQCD process for deuteron photodisintegration is shown in Fig. 3.9. Consequences of pQCD are as follows [22, 35]:

1. Total helicity must be conserved.

2. There exists a power law scaling (constituent counting rules) for fixed angle binary reactions, i.e. $A + B \rightarrow C + D$:

$$\frac{d\sigma}{dt}(AB \rightarrow CD) \sim \frac{1}{s^{n-2}} f(\theta_{cm}). \tag{3.37}$$

Thus, there are several features of this prescription. First note that in Eq. 3.37 the differential cross section is factorizable. The energy dependence and angular dependence are described by two separate functions. In general the angular piece, $f(\theta_{cm})$, is extremely complicated to calculate and depends heavily upon the underlying dynamics [22, 35]. The energy dependence depends only upon the number of constituents, or elementary fields, involved in the reaction. Elementary fields are leptons, photons, and quarks. Only those components in the initial and final states are counted. In Eq.

3.37 n can be expanded for deuteron photodisintegration as follows,

$$n = n_A + n_B + n_C + n_D, \tag{3.38}$$

where

1. $n_A = 1$, the photon
2. $n_B = 6$, there are 6 quarks in the deuteron
3. $n_C = n_D = 3$, there are three quarks in each final state nucleon.

So $n = 13$ for deuteron photodisintegration and an s^{-11} energy dependence would be expected, and seen in Fig. 2.1 where the cross section flattens out in $s^{11}\frac{d\sigma}{dt}$.

Such power law scaling has been seen in hadronic reactions. For example for $s \geq 15$ GeV^2 in proton-proton elastic scattering s^{-10} scaling is seen (see Fig. 3.10) [36]. Below $s \simeq 15$ GeV^2, however, the power law scaling is not apparent [36].

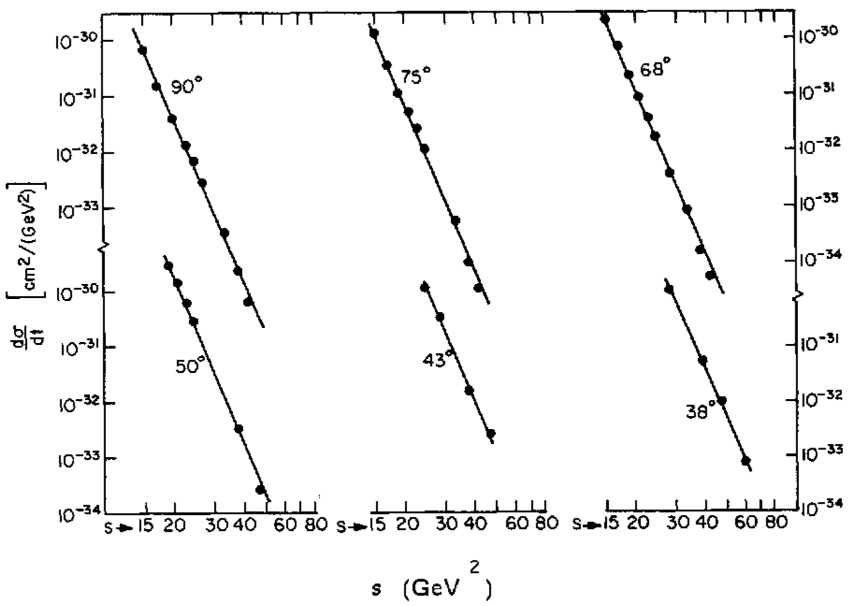

Figure 3.10: $\frac{d\sigma}{dt} \sim s^{-9.7\pm0.4}$ seen in proton-proton elastic scattering. Data are as compiled in Ref. [36].

Power law scaling predicted by the constituent counting rules has been seen in hadronic reactions such as proton-proton elastic scattering. These rules require that helicity be conserved and that there is a factorizable, fixed angle description of the differential cross section. For deuteron photodisintegration a power law scaling of s^{-11} is predicted by constituent counting. Constituent counting is only expected to be valid in regions where perturbative methods become valid in QCD, for small values of $\alpha_s(Q^2)$. The validity of applying this technique at available energies is highly contested [37].

Chapter 4

High Energy Deuteron Photodisintegtation Experiments

Experiments must be performed to gain insight into which of the two frameworks of nuclear reactions, specifically deuteron photodisintegration, provides the most complete description. Photoreactions in general, and deuteron photodisintegration in particular, have been widely used to gain insight into the transition from meson exchange to quantum chromodynamics. Both $s^{-(n-2)}$ scaling and hadron helicity conservation have been searched for extensively. Photoproduction reactions on the proton and the deuteron have been studied in order to search for $s^{-(n-2)}$ scaling. Inconclusive results have been obtained in photoproduction of pions on deuterons. A new factorization of the reduced nuclear amplitude, however, has provided some insight into understanding these results [38]. Electron scattering reactions, particularly elastic electron-deuteron scattering, have also been investigated. Hadron helicity conservation, through polarized photoreactions, has been studied. As yet data from these experiments have been unable to provide evidence of hadron helicity conservation. Deuteron photodisintegration measurements have also proved inconclusive. The differential cross section at 90° and 70° in the center of mass above approximately 1.2 GeV and up to 4 GeV persist in s^{-11} scaling, consistent with the constituent counting rules. Nevertheless, up to 4 GeV no scaling, has been seen at angles forward of 90° in the center of mass.

To further the investigation new measurements were taken. These measurements extended the energy range, up to 5.5 GeV, in which the deuteron photodisintegration differential cross section was measured at angles forward of 90° in the center of mass. A complete angular distribution suite, symmetric about 90° in the center of mass, and up to an incident photon energy of 2.4 GeV has also been measured. These new data will provide two new pieces of information to assist in the description of the transition from meson exchange to quantum chromodynamics.

4.1 Scaling in Photoproduction Reactions

Photoproduction of mesons on both protons and deuterons has been studied at high energies in the search for asymptotic scaling. Results for production on protons appear to give good agreement with constituent counting rules scaling predictions [39]. Results on the deuteron, however, are inconclusive [40].

The photoproduction of non-strange and strange, as well as some vector, mesons have been studied at high energies. Strange mesons are those which contain a strange (or anti-strange) quark, such as the kaon. Non-strange mesons, like pions, contain no strange quarks. At fixed angles in the center of mass, s^{-7} scaling seems to give reasonably good agreement with the energy dependence of the data. This seems to be true for strange as well as non-strange meson production [39]. The data available for vector meson production, ρ and ω, is insufficiently clear to determine the energy dependence of the production process. It cannot, however, rule out the s^{-7} prediction either [39].

A recent measurement of neutral pion (π°) production on the deuteron was performed at Jefferson Lab. The measurements were performed at two center of mass angles 90° and 136° [40]. The results are inconclusive. At 136° in the center of mass, the data are consistent with constituent counting rule $s^{-(n-2)}$ scaling. At 90°, however, the data produce an $n-2$ value which is much lower than predicted by constituent counting [40].

Brodsky, Hiller, Ji, and Miller have investigated a reformulation of the reduced nuclear amplitudes approach to attempt to develop and understanding of the processes involved in $\gamma + d \to \pi^0 + d$. The new factorization breaks the scattering amplitude into three factors [38]:

1. "A nucleon photoproduction amplitude carrying half of the overall momentum transfer at the same center of mass angle."

2. A nucleon form factor possessing half the overall momentum transfer.

3. A reduced deuteron form factor with monopole dependence.

Using these conditions to generate the new scattering amplitude, combined with data from photopion production on the proton, agreement with the JLab $\gamma d \to \pi^0 d$ data is obtained.

Photoproduction reactions on nucleons, particularly the proton, exhibit constituent counting rule type scaling in measured differential cross sections. These results have been reasonably consistent in both strange and non-strange meson production. Data on neutral pion photoproduction on the deuteron, however, has provided inconclusive results with respect to such scaling. Brodsky, Hiller, Ji, and Miller have developed a new factorization, akin to reduced nuclear amplitudes, which appears to provide a reasonable qualitative agreement with the JLab data [38]. Nevertheless, clear evidence for the need to explicitly include quark-gluon degrees of freedom in nuclear reactions had not yet been observed. Other tests need to be investigated.

4.2 Electron-Deuteron Elastic Scattering

There have been two recent measurements of the elastic electron-deuteron *(e-d)* structure function, another place to look for QCD behavior. A structure function is a function which describes the momentum distribution of the constituents in the target particle. These experiments were both performed at Jefferson Lab, one in Hall C and the other in Hall A.

The first of the two recent experiments to measure the elastic *e-d* structure function was performed in Hall C at Jefferson Lab. This measurement covered a Q^2 (momentum transfer squared) range from 0.66 $(\mathrm{GeV}/c)^2$ to 1.8 $(\mathrm{GeV}/c)^2$ [41]. Up to the highest Q^2 value measured in this experiment, no evidence, or consistency with, pQCD consitutent counting rules or models based upon QCD ideas was evident [41]. In fact, the results could be explained by a meson exchange model. The tensor polarization in electron-deuteron elastic scattering, which was measured in Hall C, is also consistent with meson-exchange models.

The second experiment was performed in Hall A. This experiment was designed to measure the *e-d* elastic structure function in a Q^2 range from 0.7 $(\mathrm{GeV}/c)^2$ to 6 $(\mathrm{GeV}/c)^2$ [32]. This measurement yielded an interesting result. Above $Q^2 = 2(\mathrm{GeV}/c)^2$ the data appear consistent with Brodsky and Hiller's Reduced Nuclear Amplitudes analysis (see section 3.3 for a description of Reduced Nuclear Amplitudes). The data were also consistent with constituent counting rule scaling [32]. There is one caveat, however; the data can also be described by including meson-exchange currents [32] with conventional nucleon-nucleon interactions (see Fig. 3.4).

Electron-deuteron elastic scattering, has provided some new and very useful information. Above $Q^2 = 2(\mathrm{GeV}/c)^2$ the elastic structure function appears consistent with RNA and pQCD predictions. Nevertheless, the data can still be described by meson exchange based models as well. Thus, no clear and decisive evidence of QCD behavior has been found in electron-nucleus reactions, even at high momentum transfer.

4.3 The Search for Hadron Helicity

Perturbative QCD has a second prediction–hadron helicity conservation. This condition is studied through polarization measurements. Such studies have many uses and have frequently been used to understand reaction mechanisms.

Many polarization studies of deuteron photodisintegration were carried out in the 1970's and 1980's. These studies focused primarily on the search for dibaryon resonances [42]. While this was the primary purpose of the measurements, the data from these studies, performed below 1 GeV photon energy, also provided much needed information for more general understanding of such topics as nuclear forces and meson exchange currents [42]. At higher energies the search for hadron helicity conservation became the focus of the measurements. Recent measurements from Yerevan using 0.6 GeV to 1.6 GeV linearly polarized photons have shown no consistency with pQCD hadron helicity conservation [43].

Recent polarization measurements of deuteron photodisintegration have been made at Jefferson Lab in Hall A. Using circularly polarized photons up to 2.4 GeV, the polarization transfer and induced polarization of the outgoing proton were measured [44]. The results for the polarization were inconsistent with both meson exchange and pQCD pictures of deuteron photodisintegration [44].

Polarization studies have been used to gain information about reaction mechanisms in nuclear reactions, including deuteron photodisintegration. Recent polarization studies have focused on seeking evidence for hadron helicity conservation. Even at high incident photon energies hadron helicity conservation has not yet been observed. Arguments have been formulated as to why this occurs, especially in light of recent deuteron photodisintegration cross section measurements which will be addressed in the next section.

4.4 Progress in Deuteron Photodisintegration Cross Section Measurements

In the late 1980's and throught the 1990's several experiments were performed which were designed to measure the deuteron photodisintegration differential cross section. These experiments were performed both at SLAC (Stanford Linear Accelerator Center) and Jefferson Lab. Each measurement increased the incident photon energy used in the reaction. Some suprising results were discovered as a result of these experiments.

SLAC experiment NE8 pushed the incident photon energy up to 1.6 GeV and measured backward angles in the center of mass, 90°, 114°, and 143° [3, 45]. This experiment found two suprising results. Above an incident photon energy of approximately 1.2 GeV, the differential cross section at 90° in the center of mass appeared to exhibit constituent counting rule, s^{-11}, scaling [3]. At backward angle the cross sections appeared to show a steep rise above 90° in the center of mass [45]. These results, especially the s^{-11} scaling were further investigated in another SLAC experiment, NE17.

SLAC experiment NE17 further increased the incident photon energy to 2.8 GeV. The center of mass angles 37°, 53°, and 90° were investigated in this experiment [2]. At 90° in the center of mass, s^{-11} scaling persisted up to 2.8 GeV incident photon energy. In addition, it appeared that similar scaling had set in at 53° in the center of mass [2]. Constituent counting rule scaling was not seen at 37° in the center of mass, however. Nevertheless, things were beginning to look very promising.

Jefferson Lab experiment E89-012 pushed the limits still further. Measurements were taken at 36°, 52°, 69°, and 89° in the center of mass up to a photon energy of 4 GeV. These data exhibited persistent scaling at $89° - 90°$ in the center of mass up through 4 GeV as well as scaling at 69° in the center of mass [4]. Unfortunately, the scaling at 53° in the center of mass observed in SLAC NE17 did not persist and no

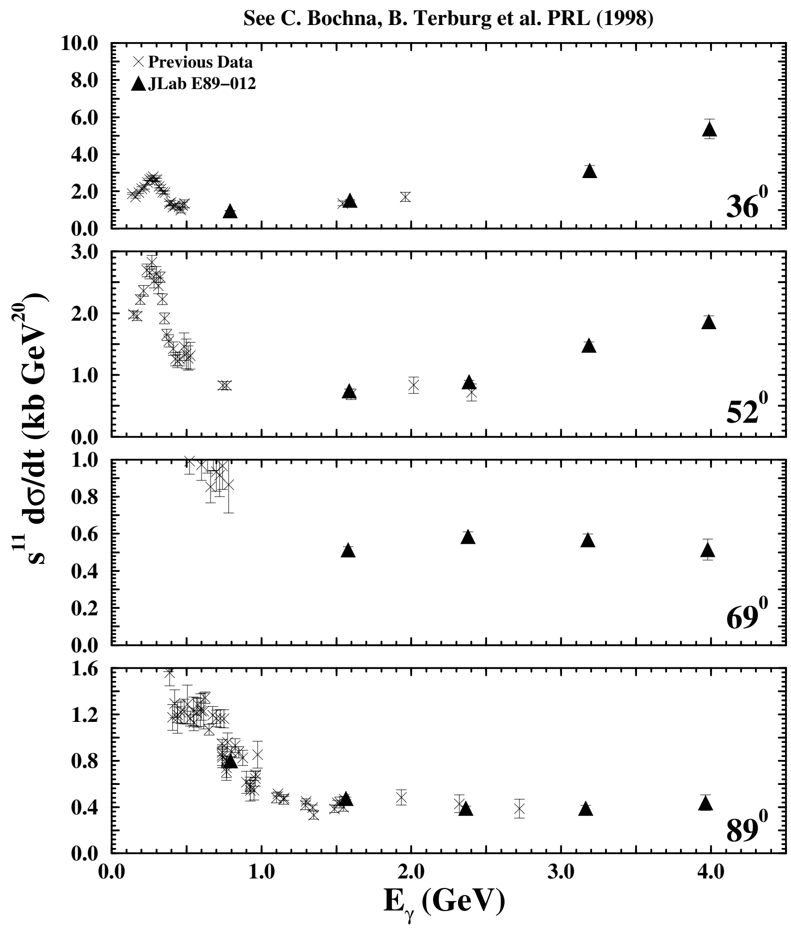

Figure 4.1: $s^{11}\frac{d\sigma}{d\Omega}$ for the $d(\gamma,p)n$ reaction up to E_γ=4.0 GeV. Data are from references [12, 13, 14]

scaling was yet seen at 36° [4]. The results of these experiments are summarized in Fig. 4.1

The past 15 years or so have seen very interesting results from deuteron photodisintegration as a reaction suitable for exploring the meson exchange to QCD transition region. The suprising results seen in SLAC and Jefferson Lab experiments warranted further investigation at both high energies and large angles.

4.5 The New Jefferson Lab Experiments: E96-003 and E99-008

Two new experiments were performed at Jefferson Lab in 1999. The first was performed in Hall C, experiment E96-003. The second was a parasitic experiment executed in Hall A, E99-008. The data from these experiments are the first at incident photon energies above 4 GeV (E96-003), and the first complete angular distribution at energies above 1 GeV (E99-008). It is hoped that both of these experiments will provide benchmark data for understanding the mechanisms which drive the deuteron photodisintegration reaction in the few GeV energy region.

The persistence of constituent counting rule scaling at 90° in the center of mass and the apparent scaling at 70° in the center of mass prompted the need to push toward finding a scaling threshold. The data at the forward angles 37° and 53° in the center of mass could provide this information if scaling should set in at these angles. This necessitated an increase in photon energy. In experiment E96-003 the photon energy was increased to 5.0 GeV and 5.5 GeV. Data were taken at 37°, 53°, and 70° in the center of mass. Because of time constraints and the very small values of the differential cross section at large center of mass angles, no further data at 90° were taken. Time constraints also required a change in the method used in background suppression. This will be addressed in detail in Chapters 5 and 6. If a scaling threshold is uncovered in these new data, it supplies evidence for the need to include QCD in the descriptions of deuteron photodisintegration.

The backward peaking observed in the data from NE8 also warrants investigation. The opportunity presented itself in Hall A during the running of experiment E89-019, a polarized deuteron photodisintegration measurement at 90° in the center of mass. Employing the spectrometer normally used for electron detection, a complete measurement of the angular distribution symmetric about 90° in the center of mass was performed. This measurement was made up to an incident photon energy of approximately 2.4 GeV. Time allowed for the taking of a extreme forward angle data point, not yet measured at high energies. At the most backward angle, 143° in the center of mass, background suppression was the primary concern. This will be fully addressed in Chapter 6.

New data now exists for deuteron photodisintegration at high energies. Previous measurements of the differential cross section have shown this reaction as a promising testing ground for exploring the transition region between meson exchange and QCD. These new data should help shed some light on the behavior of this transition region.

Chapter 5

Experimental Procedure

New measurements of the high energy deuteron photodisintegration differential cross section were made at the Continuous Electron Beam Accelerator Facility (CEBAF) at the Thomas Jefferson National Accelerator Facility (JLab). Two experiments were performed. Experiment E96-003 was executed in experimental Hall C, and the differential cross section was measured at 5.0 GeV and 5.5 GeV incident photon energies. Experiment E99-008 was performed in experimental Hall A. This measurement was made with incident photon energies of 1.6 GeV, 1.9 GeV, and 2.4 GeV. A complete angular distribution was measured. The experiments were performed in the chosen experimental halls because of the unique detection characteristics afforded by them.

To perform this measurement a high quality, high-energy, high-duty-factor electron beam was required. CEBAF was ideal for this purpose. A reliable beam of real photons and stable liquid deuterium targets, capable of operating with large heat loads, were also required. The target group at JLab was able to supply both a copper radiator system to produce a reliable source of bremsstrahlung photons as well as a set of long, stable cryogenic hydrogen and deuterium targets. Halls A and C provide detection systems capable of reaching the high momenta required to to make these measurements. The large solid angle spectrometers (detectors) needed to be able to reach very small (Hall C) and very large (Hall A) angles. The design of the spectrometers allowed for such constraints. It is the entire system offered at JLab – accelerator and experimental halls – which made these measurements tractable.

5.1 The CEBAF Accelerator

The CEBAF accelerator consists of a pair of superconducting linear accelerators connected by two bending arcs. With this setup electrons are recirculated through the accelerator increasing in energy by integral numbers of the linac energy until they are extracted into the experimental halls. CEBAF can provide electron beams to each of its three experimental halls simultaneously. The beam energy, current, and position must be monitored throughout the experiment. Position and current were monitored throughout the course of data taking. Energy was nominally monitored throughout the data taking, and periodically measured to check the absolute (real) beam energy in service. The beam current monitors were also periodically calibrated.

The CEBAF accelerator combines two linear accelerators (linacs) with two bending arcs to accelerate electrons up to a value which is roughly an integral number (up to 5) times to total linac energy. Each linac accelerates the electrons by one half of the energy per pass. One pass through the accelerator is the entire circuit: through the first (North) linac, bent through the first (East) arc, through the second (South) linac, and bent through the second (West) arc. The linacs are set by determining the energy per pass (E_p) needed to acquire the desired energy for the pass value (N) requested according to the following expression [46]:

$$E_b = \left(N + \frac{45\ \text{MeV}}{800\ \text{MeV}}\right) E_p. \tag{5.1}$$

The quantity $\frac{45\ \text{MeV}}{800\ \text{MeV}}$ in Eq. 5.1 describes the percentage of the energy per pass to which the electron injector must be set. The values 45 MeV and 800 MeV arise from the original injector and linac acceleration settings. For E96-003 the maximum energy desired was $E_b = 5.566$ GeV, an N value of 5, the highest available energy in scientific production at that time.

Each linac is made up of a series of superconducting resonant cavities. These cavities resonate at 1497 MHz. The electrons are divided into "bunches" which have a time length of 1.67 ps. The bunches arrive at the beam switch yard, the area where the electron beam is extracted into the experimental halls, at the same frequency as the cavity frequency. At extraction every third bunch is sent to a single experimental hall. Thus the bunches arrive in the hall at one third the linac resonant frequency, or 499 MHz. This provides the experimental halls with bunches of electrons separated by 2 ns [12]. Because the detector responses in the halls are longer than 2 ns, the beam appears continuous. Hence it is called a "continuous wave" accelerator [47]. A diagram of the accelerator and laboratory complex is shown in figure 5.1.

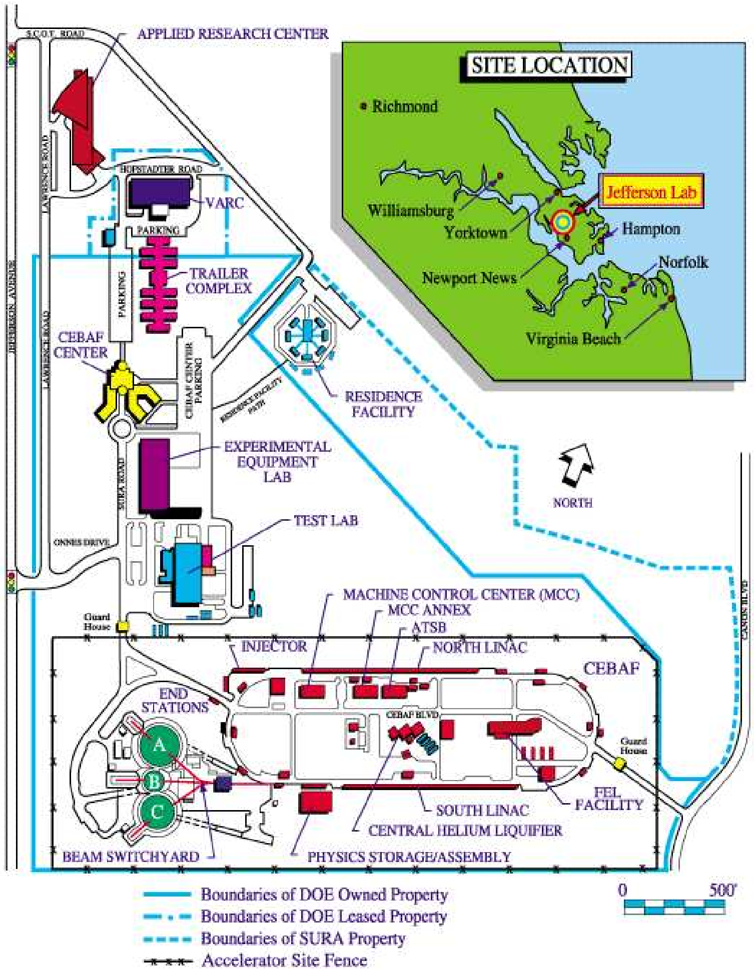

Figure 5.1: Site map of the Thomas Jefferson National Accelerator Facility complex.

5.1.1 Beam Position Measurements

Knowledge of the position of the beam is important for two main reasons. First,

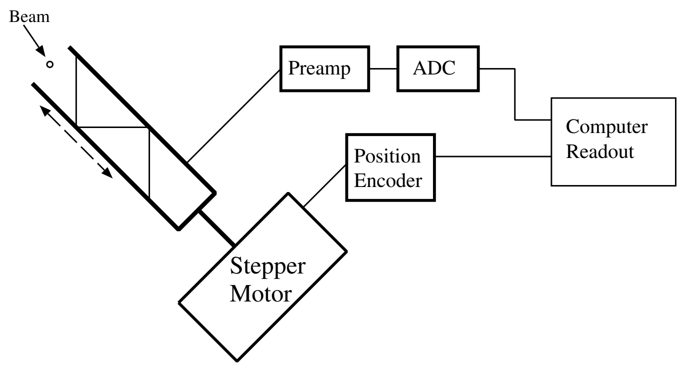

Figure 5.2: Schematic diagram of CEBAF superharps.

precise knowledge of the beam position is necessary for high precision measurements of the beam energy. During the experiment it is also important to be sure that the beam is on the target in the appropriate location in order to minimize background and to optimize the momentum measurement of reaction products in the spectrometer.

A device called a "superharp" is used to make very precise measurements of the beam position. The superharp is made up of three tungsten wires oriented such that both the horizontal and vertical beam position can be measured [12]. There are three pair of superharps along the arcs which deliver beam to the experimental halls. These are used during energy measurements to steer the beam through the dipole magnets properly. The superharp is mounted to a drive mechanism and inserted into the beam at 45° to the coordinate plane (see Fig. 5.2) [12]. The superharp gives absolute beam positions because the position of the superharp is recorded from an encoder device attached to the drive mechanism. Using this technique the position of the beam can be determined to better than 20 μm [48]. A complete description of the superharps and their use and reliability is given in Ref. [48]. This measurement technique, while, precise is destructive and cannot be employed while experimental data are being taken [12].

A second method of monitoring the beam position is employed during production data taking. Non-invasive beam position monitors are located along the beam lines entering the experimental halls. These monitors consist of a cylindrical cavity with four pickup antennae symmetrically space about the cylinder axis. The axis (z) of the cylinder lies along the beam direction, and the cylinder is rotated such that the antennae are at 45° with respect to the normal coordinate axes [49]. As the beam passes through the cylinder, the antennae pick up the bunch structure. This creates a signal which can be converted into a beam position. The beam position is determined from the difference in signal for opposing pair of antenna (for example X_+ and X_-) over the sum. This measurement is relatively insensitive to the beam current and is accurate to about ±1 mm in absolute and <0.2 mm in relative beam position [12].

5.1.2 Beam Energy Measurements

The energy of the electron beam must be accurately known. Therefore, several beam energy measurements were taken during the course of both experiments. The basic procedure for measuring the beam energy is the same in both Halls A and C. This method relied upon using the beamline arc magnets, which direct the electron beam into each experimental hall, as spectrometers.

It is the beam momentum which is actually determined. The beam momentum is given by the following expression [50]:

$$p = \frac{e}{\phi} \int \vec{B} \cdot d\vec{\ell}. \tag{5.2}$$

In Eq. 5.2 e is the charge on the electron, ϕ is the angle of beam deflection, and $\int \vec{B} \cdot d\vec{\ell}$ is the integral of the magnetic field over the path of the electron beam. In order to get an accurate momentum measurement, then, $\int \vec{B} \cdot d\vec{\ell}$ must be known very accurately.

In both the Hall C and Hall A arcs there are eight dipole magnets [50]. Hall A has a ninth dipole which serves as the reference dipole during the energy measurement

[51]. The general procedure for an "arc energy measurement" is as follows:

1. Turn off all non-dipole and compensating magnets [52].

2. Use superharps (see Subsection 5.1.1) to get an accurate beam position [12].

3. Adjust the current in the dipoles to move the beam through the centers (central ray) of the dipole system [52].

The difference between the measurements in Halls A and C comes in the way the field integral, $\int \vec{B} \cdot d\vec{\ell}$, is determined. In Hall A the ninth dipole in the arc dipole series is mapped precisely while the energy measurement is taking place. From this *in situ* field map, the fields of the remaining eight, assumed to be identical, arc dipole magnets is inferred [51]. In Hall C one of the eight dipoles in the arc series is precisely mapped as a function of current [12, 52]. The remaining dipoles, again, are assumed identical [12]. From this information about the dipole fields, $\int \vec{B} \cdot d\vec{\ell}$ can be calculated very precisely [12]. This leads to a very accurate ($\frac{\delta E}{E} \sim 10^{-3}$) absolute energy measurement [52].

5.1.3 Beam Current Measurement

The beam current measurements are vitally important to experimental measurements. It is from the beam current that the total charge, which is directly related to the number of electrons used in the experiment, is acquired. The beam current is constantly monitored during experimental data taking and periodically calibrated. An excellent discussion of the beam current monitoring equipment and techniques is given in Appendix A of Ref. [53]. A summary is presented in this thesis.

The basic current monitoring technique is the same in both Halls A and C. The pieces of equipment employed in beam current monitoring are resonant cavities (three in Hall C, two in Hall A [54]) and an Unser parametric current transformer (PCT) [53]. The Unser acts as a direct current transformer and can be very precisely calibrated.

It is used to get a “true” value for the beam current, and the resonant cavity beam current monitors were calibrated against the Unser [53].

The second beam current monitoring device, and the one which is used to calculate total charge, is a resonant cavity beam current monitor (BCM). There are three of these in Hall C and two in Hall A. These BCM’s are cylindrical cavity resonators oriented such that the electron beam passes along the z (long) axis [53]. Inside these cavities are antenna which pick up the stored power in the resonant cavity caused by the presence of the electron beam. Power, of course is proportional to the square of the current. From this information, the beam current can be continuously monitored [53].

These devices do require regular calibration. The Unser is calibrated about once each month. The BCM’s, however, require calibration every few days [53]. These pieces of equipment use different calibration techniques. The Unser is calibrated using a high precision DC current supplied by a wire which runs along, and inside, the beamline through the Unser. Because the current in the wire is very precisely known, the Unser can be very precisely calibrated [53]. The resonant cavity BCM’s are calibrated using the electron beam. The Unser, which has been previously independently calibrated, is used to obtain the “true” beam current. Using a procedure which samples beam currents from 0 to 50 μA in two minute intervals where each current set point is spaced by two minute intervals of 0 μA current sample, the BCM’s can be calibrated relative to the Unser monitor. The procedure for determining and monitoring the beam current is accurate to approximately 1% at 20 μA [53]. Because of noise, the relative accuracy is current dependent.

5.2 Bremsstrahlung Radiator and Targets

For measurements of deuteron photodisintegration, a source of real photons and a supply of deuterons are needed. The photons are obtained from a process called bremsstrahlung. These photons are the result of energy loss by electrons passing through matter [55]. The deuterons are supplied by a cryogenic (liquid) deuterium target. The use of this piece of equipment is the focus of this section.

5.2.1 The Bremsstrahlung Radiator

Bremsstrahlung is the process by which electrons, or positrons, lose energy by radiating photons as the electrons (positrons) pass through matter [55]. These photons are real, that is they have a $Q^2 = 0$. To create bremsstrahlung a "radiator" or target must be developed to produce adequate numbers of photons to carry out the experiment.

The radiator was made from thin copper (Cu) foils, and the design of the radiator was the same in both Halls A and C. In Hall C the radiator assembly was located approximately 1.2 m upstream of the center of the target [56], and in Hall A, approximately 73 cm [51]. The radiator assembly was attached to the beamline and kept under vacuum [56]. To prevent damage to the radiator foils caused by beam heating, the entire assembly was water cooled. The frame, which acted as the heat sink for the foils, was kept at or about room temperature. The water cooling was sufficient to keep the foils at about 110°C above the ambient temperature [56].

The assembly for the radiator foils holds five different thicknesses in a ladder. These foil thicknesses are nominally 2%, 4%, 6%, 7%, and 8% of a radiation length [56]. A radiation length is defined as the "distance over which the electron energy is reduced by a factor of $\frac{1}{e}$ due to radiation loss only" [55]. The radiator foils are used as the bremsstrahlung radiator are composites of multiple foils stacked together. The individual foils are extruded copper and their uniformity was measured to ± 3 μm over the foil surface. The mass of each radiator foil is known to ± 0.1 mg [56]. A table of the radiator thicknesses is given in Table 5.1. During E96-003 only the 2% and 4% radiators were used due to high background radiation levels. During E99-008 the 6% radiator was used.

Nominal Thickness (%)	Mass (g)	Area (cm^2)	Thickness $g/(cm^2)$	Total Thickness (% radiation length)
2	1.4974	6.978	0.2146	1.847 ± 0.002
	0.1626	7.111	0.0229	
4	1.5380	7.267	0.2117	3.489 ± 0.003
	1.5491	7.214	0.2147	
	0.1620	7.264	0.0223	
6	4.3316	7.260	0.5966	6.021 ± 0.003
	0.6283	7.064	0.0889	
	0.6443	7.264	0.0887	
7	4.3960	7.260	0.6052	7.060 ± 0.003
	1.5102	7.034	0.2147	
	0.6346	7.207	0.0881	
8	4.3380	7.260	0.5975	7.975 ± 0.041
	1.4944	7.076	0.2119	
	1.5421	7.132	0.2162	

Table 5.1: Radiator foil thicknesses for the Hall C radiator ladder. The foils are made up of a stack of thin foils, the thicknesses of which are given in the table. Table from Ref. [56].

The radiator position was selected through a computer controlled interface to a stepper motor. The motor raised and lowered the entire radiator ladder in steps of $\leq 2.6 \times 10^{-4}$ cm until the desired radiator was in position [56]. The lifting procedure was quite reproducible and the absolute position of the radiator was known to $\pm 2.6 \times 10^{-3}$ cm [56].

5.2.2 The Halls A and C Cryotarget

These experiments used cryogenic (liquid) hydrogen and deuterium targets. The cryotargets used in Halls A and C were extended targets and were largely identical. The differences between the two setups are listed in Table 5.2. An excellent description of the cryotarget system used at JLab is given in Appendix C of Ref. [12].

A diagram of the target system is given in Fig. 5.3, with a more detailed view of a single target given in Fig 5.4. There are three "loops" on each cryotarget ladder. Two

Hall C and Hall A Cryotarget Specifications		
	Hall C	Hall A
Operating Temperature (Hydrogen) (K)	19.00	19.00
Operating Temperature (Deuterium) (K)	22.00	22.00
Density (Hydrogen) (g/cm^3)	0.0230±0.00007	0.0230±0.00007
Density (Deuterium) (g/cm^3)	0.1670±0.0005	0.1670±0.0005
Cold Length (Hydrogen) (cm)	12.48±0.04	14.91±0.02
Cold Length (Deuterium) (cm)	12.46±0.04	14.95±0.02
Upstream Window Thickness (Hydrogen) (cm)	0.0071±0.0003	0.0071±0.0003
Upstream Window Thickness (Deuterium) (cm)	0.0071±0.0003	0.0071±0.0003
Downstream Window Thickness (Hydrogen) (cm)	0.0105±0.0005	0.0107±0.0005
Downstream Window Thickness (Deuterium) (cm)	0.0114±0.0005	0.0094±0.0005

Table 5.2: Technical specifications for the Hall C and Hall A cryotarget. Values for cold lengths and window thicnkess are from references [57, 58]

of the loops, one with hydrogen, one with deuterium, were used in these experiments. Only the extended target, that is the longer of the two, were used. The target cells were made from "3004 series aluminum beer can blanks supplied by Coors Brewing Company" [12]. These blanks have $1.3 \times 10^{-2} \pm 5 \times 10^{-3}$ cm thick walls and have had their windows punched convex. The blanks are secured to aluminum blocks which are attached to the lifting device [12]. Aluminum flow deflectors were used to create turbulant flow of the target cryogen. The entire assembly is placed in a vacuum scattering chamber with a 0.006 cm aluminum exit window to the spectrometer in Hall C [12]. The scattering chamber in Hall A has a 0.004 cm aluminum exit window to the spectrometer.

The target density was also monitored. The target densities at operating temperatures are given in Table 5.2. The error in the densities is due to two factors [57]:

1. Estimates in the amounts of ortho- and para-hydrogen.

2. Uncertainties in the equation of state for deuterium.

These caused an approximately 0.5% error in density determination. There is also an error in density due to temperature measurements of on the order of 0.1%. When the

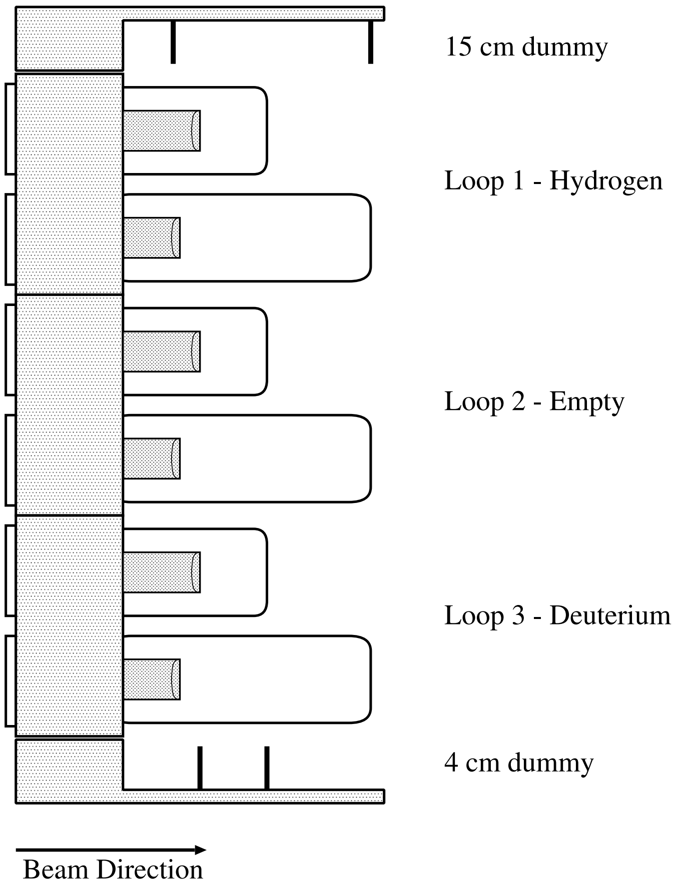

Figure 5.3: Schematic diagram of the cryogenic target stack. Note that in Hall C the long cell is only 12.5 cm.

beam changes, current increases and decreases, or the beam shuts off, the temperature and thus the density temporarily fluctuates. The measured fluctuation of density with temperature was about 1.8% for hydrogen and 1.3% for deuterium per Kelvin of temperature change. For the beam currents used in this experiment $\approx 25\ \mu$A effects of energy deposited by the beam causing density fluctuations in the target was negligible [57]. Unfortunately, target purity was not measured during these experiments. Nevertheless, the purity of the target, estimated from previous samplings was $\sim 99\%$ for deuterium.

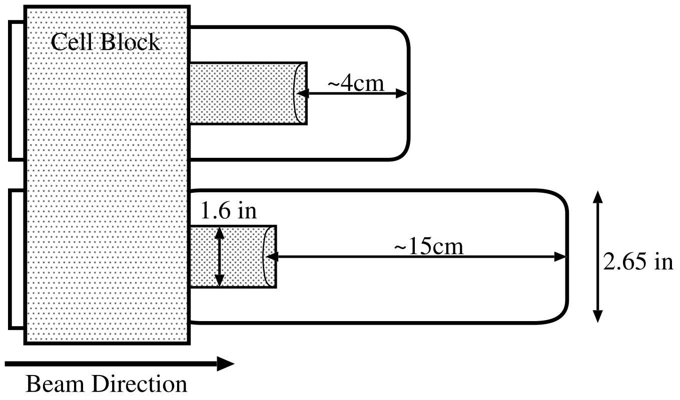

Figure 5.4: Schematic diagram of a single cryotarget cell. Note that the cell long cell in Hall C was only 12.5 cm.

5.3 Detection

Using the real bremsstrahlung photons from the radiator and the deuterons

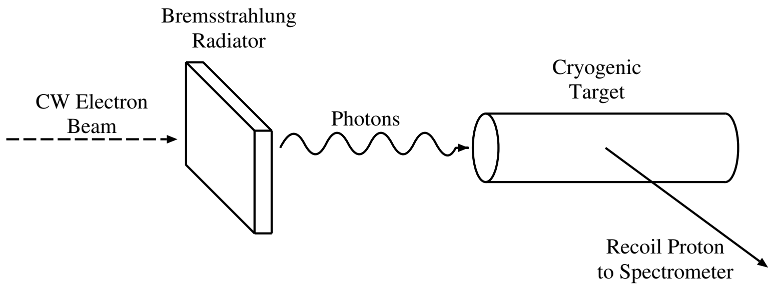

Figure 5.5: Schematic diagram of the $d(\gamma, p)n$ experimental setup. In Experiment E96-003 the target was 12.5 cm long, whereas in Experiment E99-008 the target was 15 cm long.

from the deuterium target the deuteron photodisintegration reaction can take place. (see experimental setup sketch in Fig. 5.5). The recoiling photons were the particles which are detected. Protons are charged and this makes them much easier to detect than the neutrons. To "view" these protons, a magnetic spectrometer was used. A spectrometer works for charged particles much like a light microscope, and prisim. The magnetic spectrometer, however, is much larger.

5.3.1 Quadrupoles

Like a microscope the spectrometer is first aligned with the object under study. In both Halls A and C all spectrometer equipment is mounted to motorized carriages which allow them to be placed at various angles in the laboratory [59, 54]. The spectrometers "view" the target through a high density collimator (see Fig. 5.6 for an example of the Hall C collimator) which helps to define the "solid angle" ($\Delta\Omega$) or volume of angular space seen by the spectrometers [59, 54]. Table 5.3 summarizes many of the important features of the Hall C (HMS) and Hall A (HRS) spectrometers.

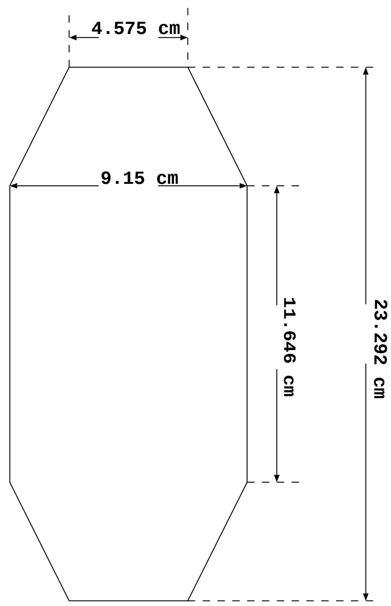

Figure 5.6: Schematic diagram of the Hall C HMS entrance collimator.

HMS and HRS Technical Specifications		
	HMS	HRS
Spectrometer Type	QQQD	QQDQ
Bend Angle	$25°$	$45°$
Maximum Central Momentum	7.4 GeV/c	4.0 GeV/c
Momentum Resolution	$<0.1\%$	$\sim 0.02\%$
Momentum Acceptance	$\pm 8\%$	$\pm 4.5\%$
Solid Angle, point target	~ 8 msr	~ 6 msr
Solid Angle, extended target	~ 6 msr	~ 4 msr

Table 5.3: Technical specifications for the HMS and HRS. The HMS is a quadrupole, quadrupole, quadrupole, dipole spectrometer, while the HRS is a quadrupole, quadrupole, dipole, quadrupole spectrometer. Further information on the HMS is available in reference [59]. For more information on the HRS see reference [60]

The focusing elements of the spectrometers are a series of quadrupole magnets. These quadrupoles act as a series of thin lenses for charged particles [61, 55]. Unlike thin lenses, however, magnetic quadrupoles have two axes which must be taken into consideration. Each quadrupole has a convergent (focusing) and divergent (dispersive) axis. These quadrupoles are combined to act much like optical doublets or triplets in a thin lens system across each axis. Just like a system of thin lenses, the magnetic doublets or triplets provide magnification to the original object, in this case the pattern of recoiling particles from the target. The quadrupoles focusing strengths are adjusted for the particles of interest by adjusting the magnetic field to the necessary strength.

As Table 5.3 shows the HMS (High Momentum Spectrometer) in Hall C has a triplet configuration of quadrupoles followed by a dipole [59]. The HRS (High Resolution Spectrometer) in Hall A has a doublet preceding its dipole. The dipole is followed by a third quadrupole which provides some additional focusing in the convergent (focusing) direction [62].

5.3.2 Dipoles

The incoming particles from deuteron photodisintegration which have been collected and focused by the quadrupole optics must now be analyzed. On their way to the focal plane, the particles pass through the first piece of analyzing equipment, the dipole. The dipole acts as the prism did in Isaac Newton's famous experiment breaking white light into its colors. This is the phenomenon called dispersion [63] and works in a similar way for charged particles in a magnetic field.

The dipole of the spectrometer provides a reasonably constant magnetic field. Each dipole bends the particles by an angle θ: 25° for the HMS, 45° for the HRS. The steeper the bend angle, the greater the effect of the dispersion, which allows greater momentum resolution. The dispersion occurs because the charged particles entering the magnetic field are bent at different radii according to their momentum [61, 55]:

$$cP = 0.3BR. \tag{5.3}$$

In Eq. 5.3 P is the momentum of the incoming protons, B is the magnetic field, and R is the radius of curvature for the bending particle. The dipole field B is set such that the particles having the desired nominal momentum, called the "central momentum," will follow a path through the center of the dipole. This is the "central ray." Particles of momentum differing from the chosen central momentum will follow different paths governed by Eq. 5.3.

5.3.3 Detectors

Once the particles have moved through the magnetic optical system, they must be imaged. In the microscope analogy the eye, or some other optical device like a camera, is used for the purpose of imaging. Photographic emulsions, in fact, have been used to detect charged particles, however, it is not the most efficient method for this purpose. Much more efficient electronic methods are available for particle detection. Each spectrometer is "topped" with a detector package surrounded by a high density concrete shielding house, referred to as a "hut" [59, 54]. The detectors in each hut are an ionization detector called a "drift chamber," a set of scintillation detectors called "hodoscopes," and a Čerenkov counter. The HMS also contains an electromagnetic calorimeter which, for experiment E96-003, was used only during certain calibrations. Diagrams of each spectrometer and the detector packages are shown in Figs. 5.7, 5.8, 5.9, 5.10.

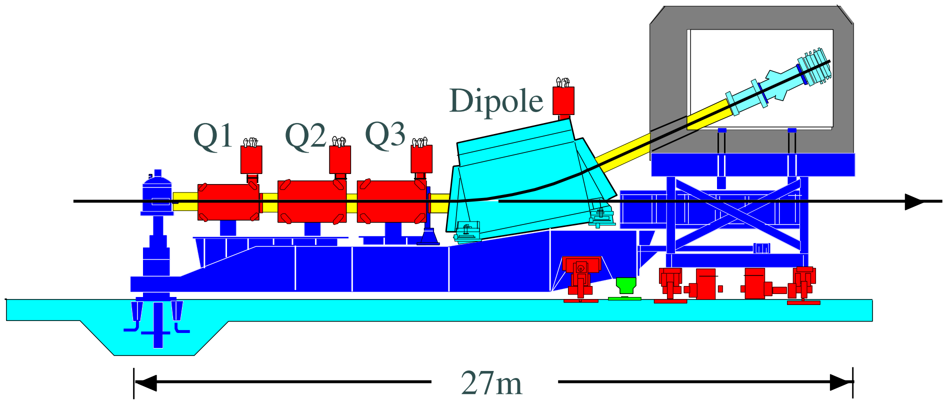

Figure 5.7: Schematic diagram of the HMS in Hall C. Q1, Q2, and Q3 are the three quadrupole magnets.

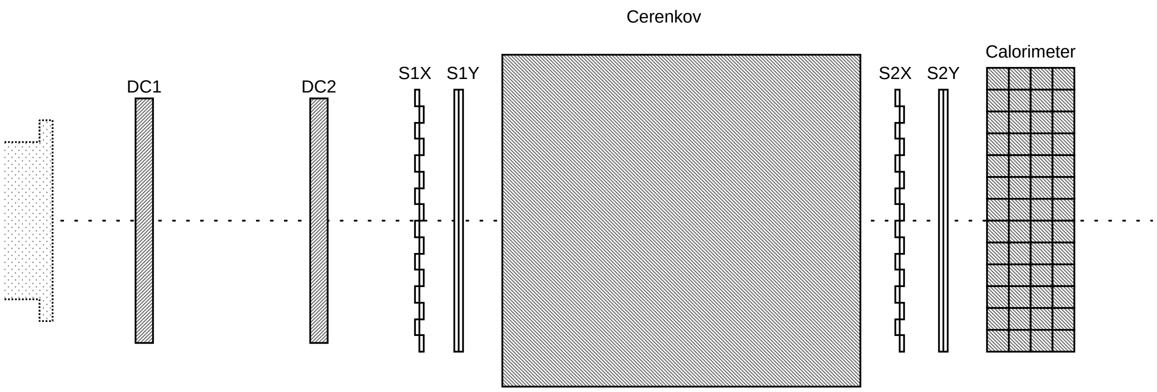

Figure 5.8: Schematic diagram of the HMS detector package. In the figure, DC1 and DC2 denote the two drift chambers and S1X, S1Y, S2X, S2Y denote the two pair of segmented, scintillator hodoscope planes.

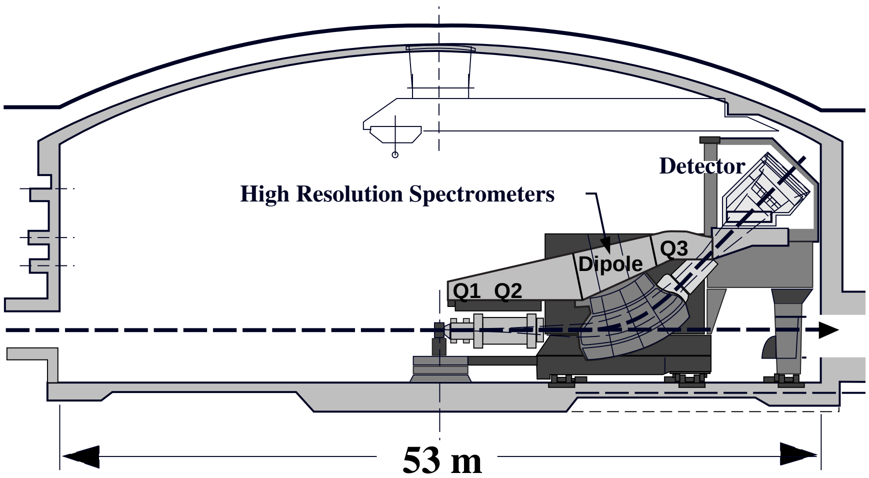

Figure 5.9: Schematic diagram of the HRS in Hall A.

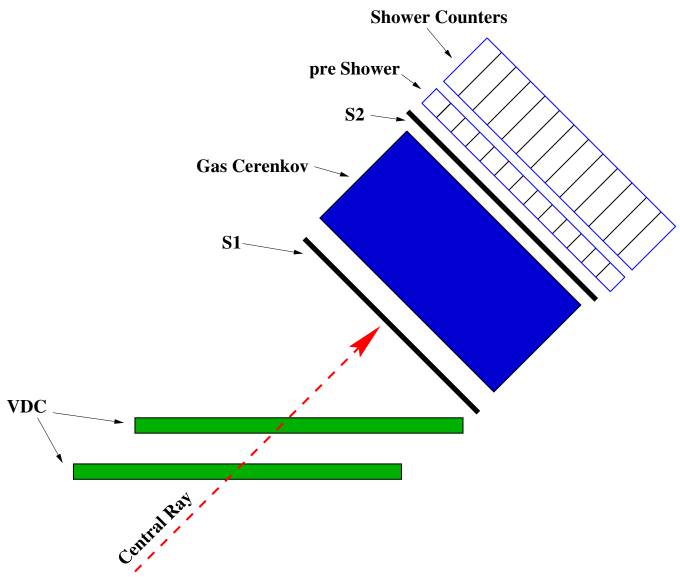

Figure 5.10: Schematic diagram of HRS detector package. The verticle drift chambers are labeled **VCD** and **S1** and **S2** are the two hodoscope drift planes described in the text.

5.3.3.1 Drift Chambers

Each spectrometer detector package is equipped with a pair of drift chambers. Drift chambers are electronic devices which rely upon the ionization of a gas as a charged particle passes through the gas [55]. The gas chosen for the JLab Hall A and C spectrometers' drift chambers is a mixture of argon and ethane, 65% argon to 35% ethane in Hall A [54], 50% argon 50% ethane in Hall C [64]. This is called the "drift gas" [55]. Diagrams of the HRS and HMS drift chambers are given in Figs. 5.11 and 5.12.

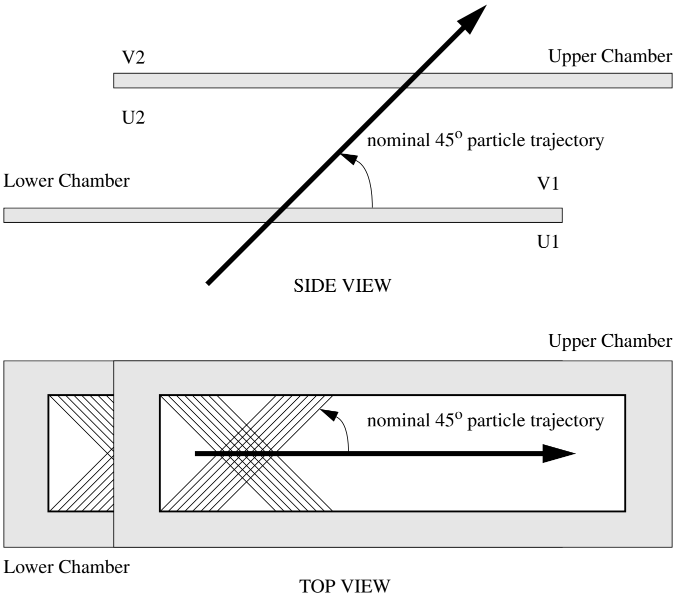

Figure 5.11: Schematic diagram of the HRS drift chambers.

As the particle passes through the gas, electron-ion pairs are created. The electrons are accelerated through a constant electric field held between the cathode and anode (signal) wires [55]. Typically extra wires called "field wires" are also introduced to help keep the field uniform [55]. This is the case in Hall C where the drift chambers are made up of six wire planes. Four of the planes measure x and y with one of the x and y planes (the x' and y' planes) offset from the other. The remaining pair is at a 15° angle (the u and v planes) [59]. In these chambers the anodes consist

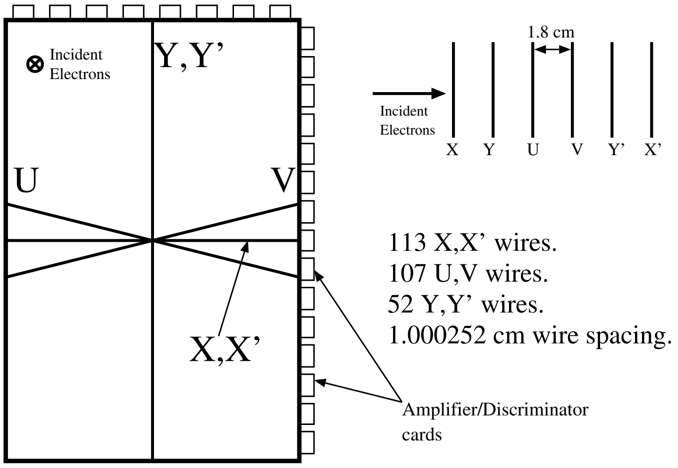

Figure 5.12: Schematic diagram of the HMS drift chambers.

of 25 μm gold plated tungsten wire separated by 1 cm. The cathode (field wires) are 150 μm gold plated copper-beryllium wires [64]. These wires are also spaced 1 cm apart but are located in between the sense wires [59]. In addition there is a plane of field wires each separated by 9 mm from the "sense plane" between each plane of alternating cathode/anode wires (sense plane). This gives a sense plane (x, x', y, y', u, v) spacing of 1.8 cm. The chambers are separated from each other by 81.2 cm and have an active area (the area where particles are detected) of 113 cm by 52 cm. Further details can be found in Refs. [59] and [64].

In Hall A the chamber design is somewhat different. These chambers have only two wire planes set at 45° with respect to the chamber frame. The anode wires are 20 μm gold plated tungsten. The cathode, however, is a sheet of 6 μm gold plated mylar. Therefore, no field wires are used [54]. Instead three high voltage (cathode) planes are used in each chamber [65]. There are a total of 400 wires in each chamber, of which 368 are sense wires [54] and the remaining 32, 16 on each end, are used to shape the field [65]. The chambers have an active area of 211.8 cm by 28.8 cm with a wire spacing of 4.2 mm. They are 35 cm apart and horizontally offset by 35 cm [65].

In both cases the chambers, which are capable of giving position information, are used to determing the incoming particle's path. This is called "tracking." From the particle tracks, the original location of the particle can be deconvolved.

5.3.3.2 Scintillation Detector

Both spectrometers have a set of scintillation counters called hodoscopes. Scintillators are detectors with fast responses to the presence of a charged particle. They are devices which contain a luminescent chemical which fluoresces, that is once excited by an energetic particle, gives off energy as light very rapidly [55]. In the case of Hall A and C the scintillator counters were made out of thin polystyrene bars doped with a fluorescing organic molecule [59, 65]. Plastic is desirable because it is inexpensive, easily shaped, and safe for the user to handle [55]. The bars are optically connected at each end by a lucite light guide to a photomultiplier tube [59, 65]. These bars are organized into planes. There are four planes in Hall C [59] and two in Hall A [65].

In Hall C the four planes are organized into two pair of x and y planes. These pairs are separated by approximately 2.2 m. The scintillators serve to provide time-of-flight information as well as form the event trigger [59]. The x planes consist of 16 bars 75.5 cm long by 8 cm wide by 1 cm thick. The y planes are 10 bars 120.5 cm long by 8 cm wide by 1 cm thinck. To ensure complete coverage the scintillator bars are overlapped by 0.5 cm, giving a total active area of 120.5 cm. by 75.5 cm [59].

The setup in Hall A is somewhat simpler. Hall A has only two planes of scintillators. These planes are separated by approximately 2 m. Each plane has six 0.5 cm thick scintillator bars overlapped by 0.5 cm. The two planes have different active areas. The forward most plane (S1) has an active area of 170 cm by 35 cm while the back plane (S2) has an active area of 220 cm by 54 cm [65].

A summary of the PMT models used in Halls A and C is in Table 5.4. In both cases the scintillator signals from the PMT's are read out by ADC's and TDC's. The signal is passed to an ADC and descriminator. The ADC's provide information about the amount of energy deposited in the scintillator bars. The signal passed to

Hall C and Hall A Hodoscope PMT Models		
	Hall C	Hall A
Hodoscope	Phillips XP2282	Burle 8575

Table 5.4: Phototube types used in Halls A [66] and C [59].

the descriminator. If the signal fires the descriminator, a signal is sent to the TDC and logic modules which form the appropriate combinations of signals to register an event in the hodoscope [59, 54].

5.3.3.3 Čerenkov Counters

Each detector package has a counter, used to identify particles, which works on the phenomenon of Čerenkov radiation. Čerenkov radiation occurs whenever a particle travels faster than the speed of light in the medium in which the particle is travelling [55]. The speed of light v in a medium is dependent upon the index of refraction of the medium n:

$$v = \frac{c}{n},\ c \text{ the speed of light in vacuum.} \tag{5.4}$$

When a particle's velocity (β) exceeds v then a shockwave effect occurs and light is produced [55]. This light can be collected by a phototube to detect the presence of a particle in the counter. The momentum threshold for a particle to be detected by Čerenkov radiation is

$$P_T = \frac{M_{part}}{\sqrt{2\delta}} \tag{5.5}$$

where δ is the difference between the index of refraction of the medium and the index of refraction of vacuum [61, 55]. Using this formula the materials with the necessary index of refraction can be chosen.

In Hall C the Čerenkov counter was used for pion detection. The counter is a 1.2 m long cylinder [59] which was filled with perfluorobutane (C_4F_{10}) gas at 0.78 atmospheres. Perfluorobutane has an index of refraction of 1.00143 at 1 atmosphere and 300 K [59]. At this pressure the pion threshold (using Eq. 5.5) is 2.5 GeV/c, more than adequate for E96-003.

In Hall A the detector package is equipped with both a gas Čerenkov [65] and an aerogel Čerenkov. The 1.5 m gas Čerenkov was filled with 1 atm of CO_2 gas (n=1.00041) [65]. This did not provide any particle identification for E99-008. The aerogel Čerenkov, however, was intended to provide pion identification. Upon data analysis, however, it appeared that the aerogel Čerenkov failed to function. This was not detrimental for the experiment, however, since pion background was expected to be negligible, and found to be so in previous experiments.

5.3.3.4 The Lead Glass Calorimeter

An electromagnetic calorimeter, made from 10 cm by 10 cm by 70 cm lead glass blocks, was used in Hall C for certain calibration procedures. The calorimeter was 4 blocks deep and 13 blocks high [59] with phototubes at each end of the glass blocks. An electromagnetic calorimeter measures the energy of an incoming particle by detecting all of the energy deposited within the calorimeter. By analyzing the amounts of energy left in the calorimeter, some additional particle identification is made possible [59].

5.4 The Trigger

All of these detector signals are read out by various electronics. Analog-to-digital converters (ADC's) were used to measure the charge for any signals from the photomultipliers. Time-to-digital converters were used to measure the times at which events occured, in for example, the drift chambers. A summary of the electronics types is given in Table 5.5.

All of this was controlled by an electronic logic device called the trigger supervisor. The trigger supervisor (TS), in the microscope with a camera for image recording

Hall C and Hall A Data Acquisition Electronics		
	Hall C	Hall A
Drift Chambers TDC	LeCroy 1877	LeCroy 1877
Hodoscope TDC	LeCroy 1875	LeCroy 1872A
Hodoscope ADC	LeCroy 1881M	LeCroy 1881M
Čerenkov ADC	LeCroy 1881M	LeCroy 1881M

Table 5.5: ADC and TDC types used in the Halls A [66] and C [59] (TDC model obtained from Ref. [12]) data acquisition electronics.

analogy, acts as the shutter on the camera. The TS "decides" when an event can be read and what type of event is being processed [59]. The TS has three logical states, GO, EN1, and BUSY. GO is the state which must be true in order for data taking to begin. EN1 enables the real physics events to be taken. There is a non-physics event type, the pedestal, which is taken at the beginning of each data run. The pedestal triggers are the first 1000 triggers in the file and are randomly generated by a pulser in the TS [59]. During pedestal triggering all ADC channels are read out and threshold values determined. EN1 is "false" for pedestals so that real physics events are not included. After taking pedestals EN1 is set to "true" and only ADC or TDC channels which have data to be recorded are read from that point onward. This is called sparsifed [59]. The third state, BUSY, prohibits the processing of a new incoming event if a previous event is still being processed [59].

These three control states are read by a programmable logic module with eight outputs (LeCroy 8LM 2365). The first four inputs create what is called a "pretrigger." The pretrigger is the state where the triggering condition has been met, the firing of scintillator hodoscopes in this case (the specifics of which will be discussed later) and EN1 is "true". If the TS is not busy (BUSY set to "false") then a trigger is formed. The triggers are the signals from the remaining four outputs on the logic module [59]. Both the real triggers and the pretriggers are counted by scalers, devices which increment each time a pulse is sent to them, and used for determine dead time [59]. See Figs. 5.13 and 5.14 for an example of how trigger electronics can be set up.

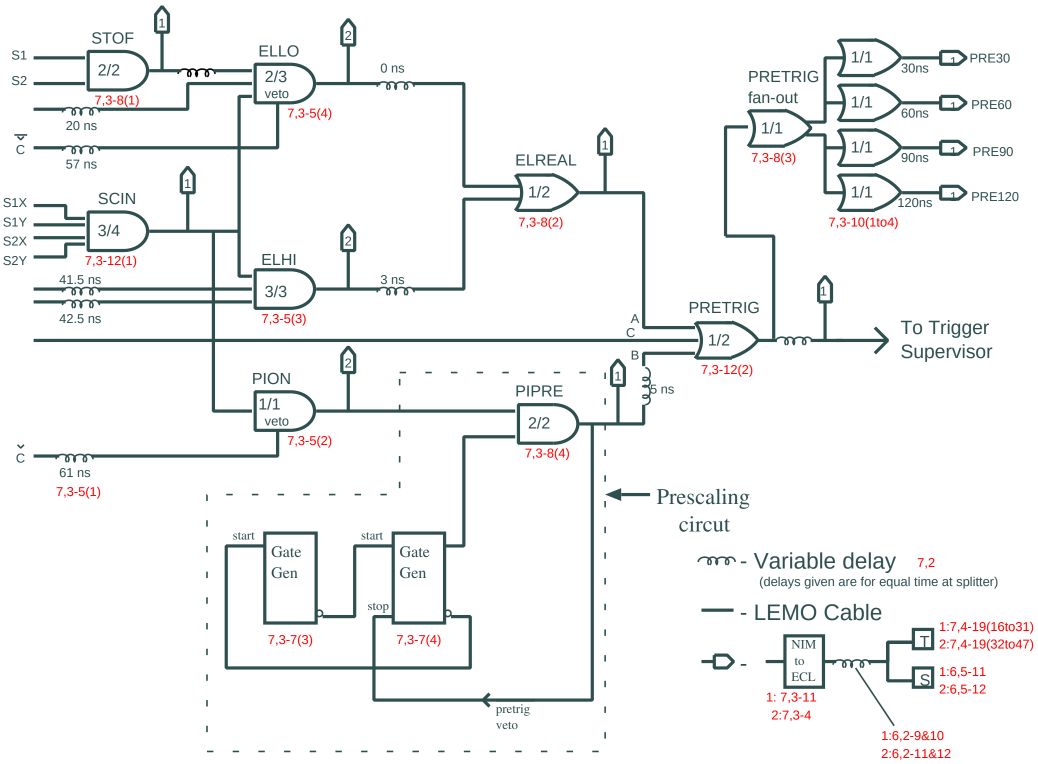

Figure 5.13: Example of a trigger electronics setup. This example is the Hall C single arm trigger.

5.4.1 The HMS Trigger

The deutron photodisintegration experiment E96-003 used a simple trigger a diagram of which is in Fig. 5.13. A trigger was formed when all four scintillator planes were hit and signals were detected under the following conditions [59]

1. In the x planes, both a right and a left phototube, anywhere on the plane, must have fired (top and bottom for the y planes).

2. Each of the four scintillator planes must meet condition 1 (that is a logical AND of condition 1 in each plane was formed).

3. When condition 2 is met, this is called the "SCIN trigger" [67] and SCIN is set to "true."

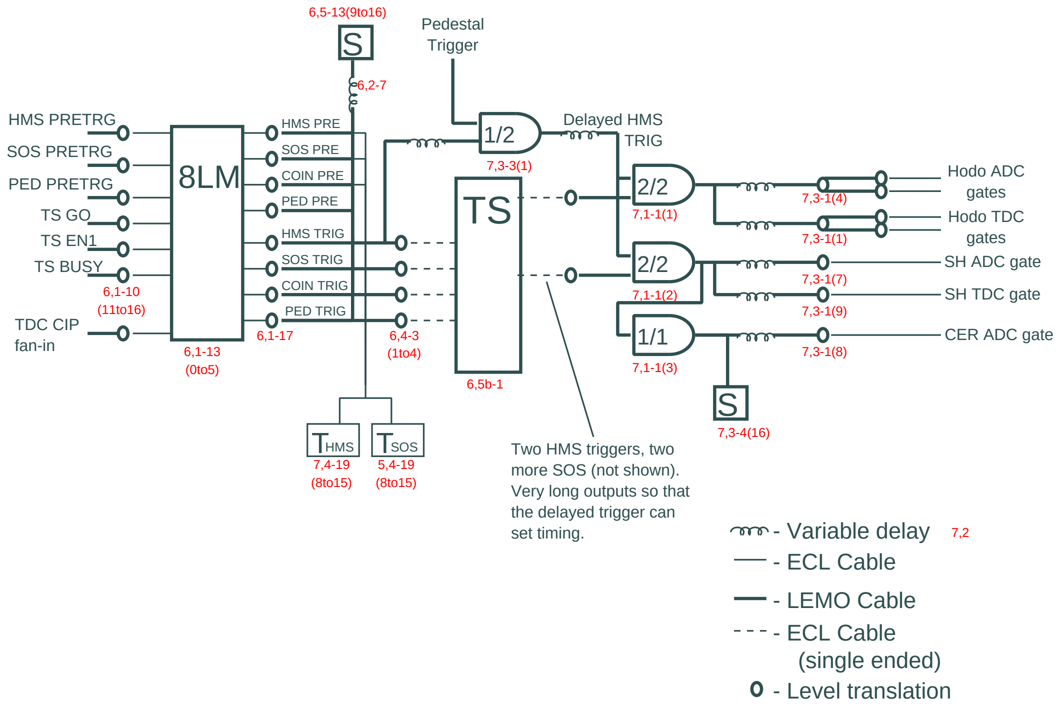

Figure 5.14: Example diagram of the trigger supervisor electronics. This schematic diagram is for the Hall C trigger supervisor.

4. SCIN is sent to the TS, which if EN1=TRUE and BUSY=FALSE a trigger is formed (otherwise a only pretrigger is formed) and the TDC starts and stops and ADC gates are sent to the readout electronics and the event is processed.

The processed event is read out and recorded by the data acquisition computer. This computer runs the CEBAF Online Data Acquisition (CODA) which controls the acquisition of data from the Read-Out Controllers (ROC's), CPU's on FastBus and VME crates [59]. After collection and building by the computer, the events are written to disk, and subsequently to tape in the JLab data storage tape silo. More detailed information on the trigger setup and CODA are available in [59].

5.4.2 The Hall A Trigger

The Hall A trigger is also quite simple. The trigger is formed, once again by signals from the scintillator hodoscope. Both planes must have a valid combination of signals to compute the trigger [54].

The scintillation trigger is formed as follows [54]

1. Both left and right phototubes of the *same* scintillator bar in each plane must fire.

2. The signals from each scintillator plane are combined to form a logical AND.

3. The programmable logic unit (which take the place of the 8ML in the general trigger description) checks the signals to ensure the track of the particle is approximately 45°.

4. This signal, S1, is sent to the trigger supervisor for event processing.

Once a successful trigger has been formed data acquisition proceeds in the same was as for Hall C. More information about the Hall A trigger is available in Ref. [54].

Chapter 6

Analysis of Deuteron Photodisintegration Data

Once the high energy deuteron photodisintegration data were collected and written to tape in the JLab data storage silo, the data were ready for analysis. The analysis of these data proceeded in several stages. The first stage involved checking the spectrometers' ability to reproduce expected patterns. This is known as checking the spectrometer's optics. The second stage involved extracting quantities from the data which are used to reconstruct the spectrum of photon energies which impinged upon the liquid deuterium target. The third and final stage was the extraction of the number of events which could be used to measure the differential cross section.

The "raw" event files produced by the CODA event builder must first be "replayed" or decoded into useful data files. That is, files which contain the information about an event not only in terms of signals from the data acquisition electronics, but also in a form which extracts the kinematic quantities for an event from the electronics' signals. Kinematic quantities are those which describe the event in terms of physical quantities such as momentum and angle. This decoding is done by a "replay engine" which is designed to take in the information from the detectors through the readout electronics and reconstruct from times (provided by the TDC's) and analog signals (from the ADC's) the various quantities of interest. Both experimental halls used in these experiments had their own replay software. In Hall A the replay software was called ESPACE and is described in Ref. [54]. In Hall C software known as "Hall C Replay" was used and is described in Ref. [59]. All data used in any steps of the analysis process were first replayed before it was analyzed.

6.1 Spectrometer Checkout

The first data replayed was "optics data" which, in this case, consisted of data taken on a carbon target with a "sieve" inserted in the entrance collimator. The sieve was a high density plate with a grid of holes drilled into it, an example of which is given in Fig. 6.1 for the Hall C High Momentum Spectrometer (HMS). A similar slit was used in the Hall A spectrometer.

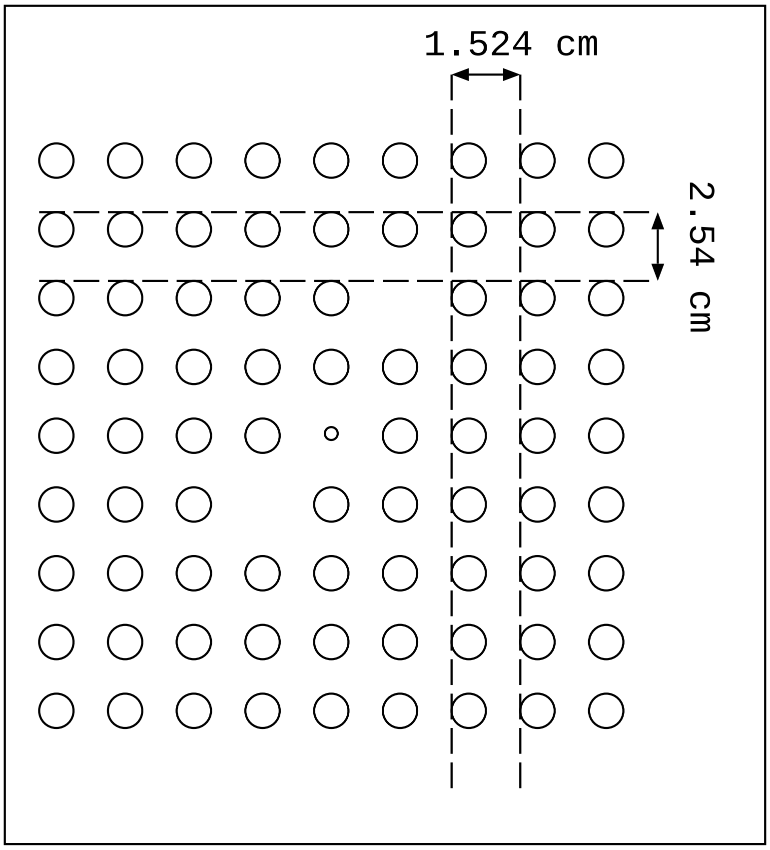

Figure 6.1: Schematic diagram of the HMS sieve mask.

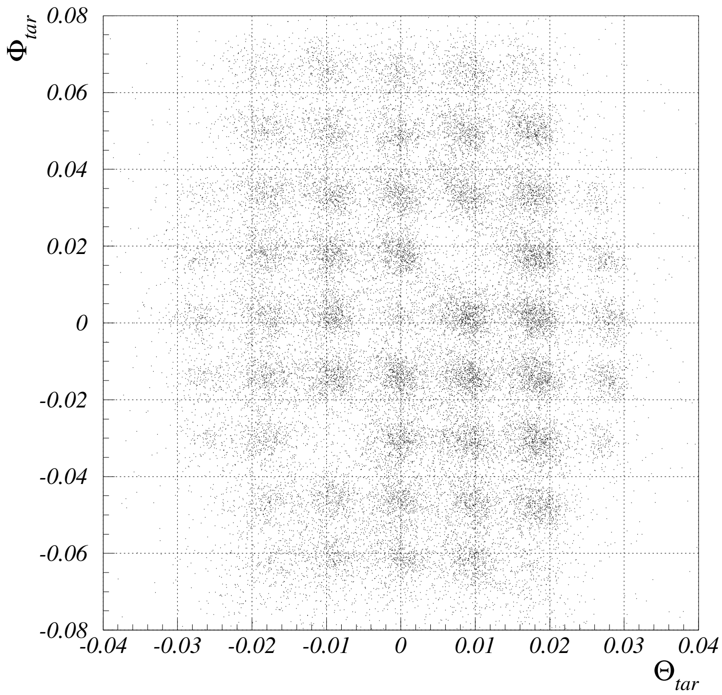

Figure 6.2: Image of the Hall C HMS sieve mask at the target.

Electrons which scatter from the carbon target into the spectrometer and which pass through the holes in the sieve are recorded. After replay, the angles (ϕ_{target} and θ_{target} in Fig. 6.2) which are in-plane (θ_{target}) and out-of-plane (ϕ_{target}) are reconstructed and plotted (See Figs. 6.2 and 6.3). The center hole is smaller in Fig. 6.2, which reduces the number of events making the image smaller. The center hole in Fig. 6.3 is larger increasing the number of events which pass through making a darker image. The open spaces in Fig. 6.2 (larger "dots" in Fig. 6.3) are used to ensure correct orientation of the image. From these images the error in the reproduced spacing of the sieve holes can be determined. Also, any shifts that may be needed to center the image can be applied to the replay engine. With appropriate input and good agreement with of the replayed data set with the measured values, of such quantities as sieve hole spacing, confidence in the reconstruction of scattering angles

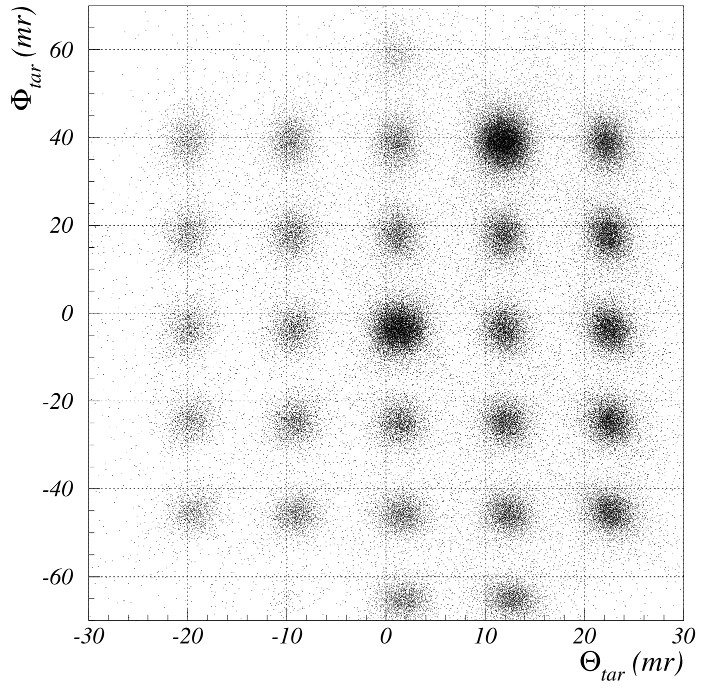

Figure 6.3: Reconstruction of the Hall A sieve mask at the target.

and the determination of the solid angle is obtained. The agreement of the sieve slit reconstruction with the measured hole spacing was 4% with an error comperable to the measurement for the Hall C High Momentum Spectrometer using the COSY-based matrix elements, and 1% for the Hall A HRS with the fit of the matrix elements being the primary limiting factor.

The next set of data analyzed is some elastic electron scattering from a hydrogen (proton) target. This data is used to check the shape of the focal plane distributions against expected distributions for elastic scattering of electrons off of protons. The expected distributions are generated by the Hall C Monte Carlo computer program SIMC. SIMC was later modified to describe the Hall A HRS. SIMC is a computer program which generates simulated physics events according to a user-selectable, probability distribution. These simulated events are then propagated through a model system. This procedure generates "spectra" or patterns of events, which can be compared to real physics spectra. Because elastic electron scattering from protons is a well known and well studied reaction, it makes a good test case for the optics study, which, in this case, provides information about how well the Monte Carlo is working (see Figs. 6.4 and 6.5).

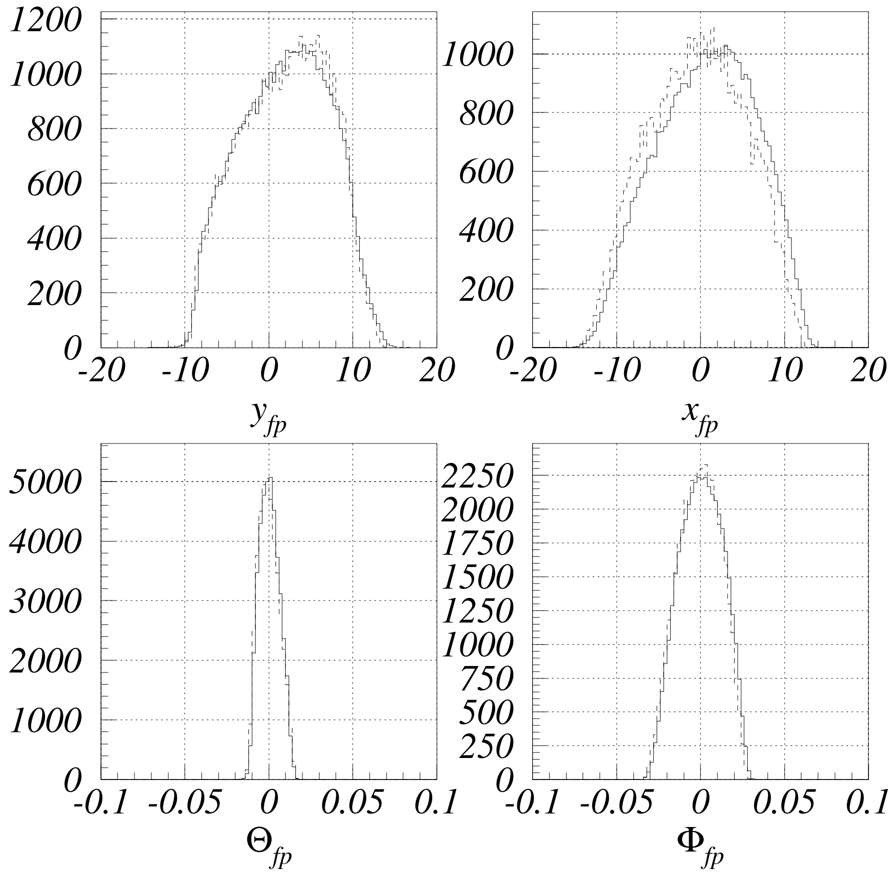

Figure 6.4: A comparison of elastic electron scattering from a proton target in the Hall C HMS, Monte Carlo (dashed line) to data (solid line).

The comparison of the Monte Carlo generated proton elastic electron singles distributions also provides a means of checking how well the spectrometer reconstructs the particle momenta. By comparing the spectra for the reconstructed momenta

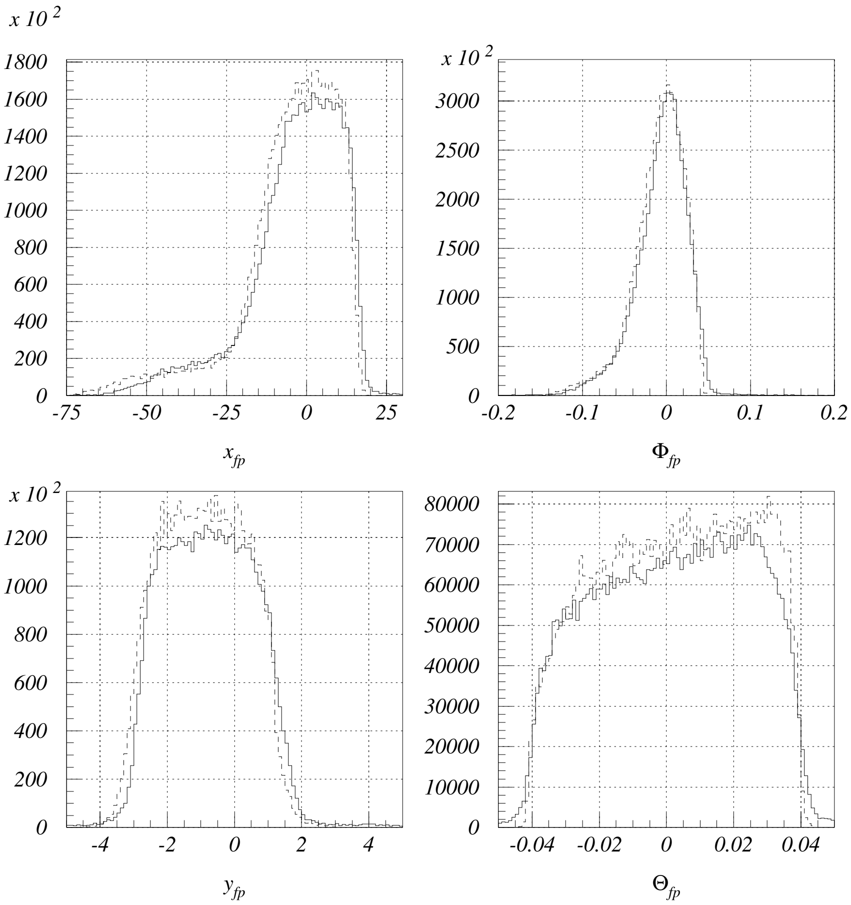

Figure 6.5: A comparison of elastic electron scattering from a proton target in the Hall A HRS, Monte Carlo (dashed line) to data (solid line).

(which is analogous to x_{fp} in Figs. 6.4 and 6.5) an offset between the Monte Carlo and spectrometer spectra is observed. This offset which was about 0.5% for the HMS and 0.4% for the HRS. Systematic errors were estimated from these offsets. They added approximately 0.3% to the center-of-mass cross section error through the jacobian which converts the laboratory differential cross sections to the center-of-mass differential cross sections. An additional error of about 5% was added to the E96-003 $s^{11}\frac{d\sigma}{dt}$ values through the error in s^{11}.

The "optics" which are actually checked is a matrix which describes the passage of particles through the magnetic "lenses" (see section 5.3.1). This matrix, for Hall

C and the Monte Carlo used for both Hall A and Hall C was generated by a program developed by Michigan State University's National Superconducting Cyclotron Facility called COSY Infinity [68] and calculated up to 6th order. In Hall A the HRS optical matrix is produced by fitting the sieve slit data, and calculated up to 5th order. These matrices are akin to the optical matrices used to calculate the focal length, magnification, and other optical quantities for a series of optical lenses [63].

The momentum resolution must also be estimated. This procedure also used the electron-proton elastic singles data. Generating spectra for the reconstructed electron momentum in which the angular dependence is removed, a gaussian can be fit to the elastic peak found in the spectra (See Figs. 6.6 and 6.7). The resolutions found from these fits (the standard deviation σ of the gaussians) was 0.24% for Hall C and 0.2% for Hall A. The value for the Hall A resolution, however, was found at relatively low momentum, $p_e = 0.724$ GeV/c. A part of the relatively large momentum resolution is caused by multiple scattering through the target and vacuum chamber, as well as the target position resolution.

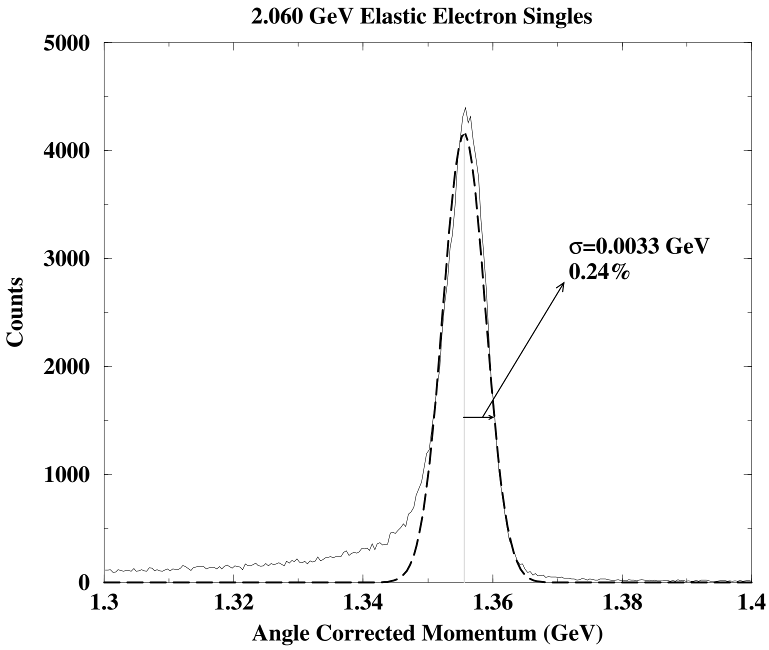

Figure 6.6: A gaussian fit to the elastic peak for the HMS at 2.060 GeV incident beam energy.

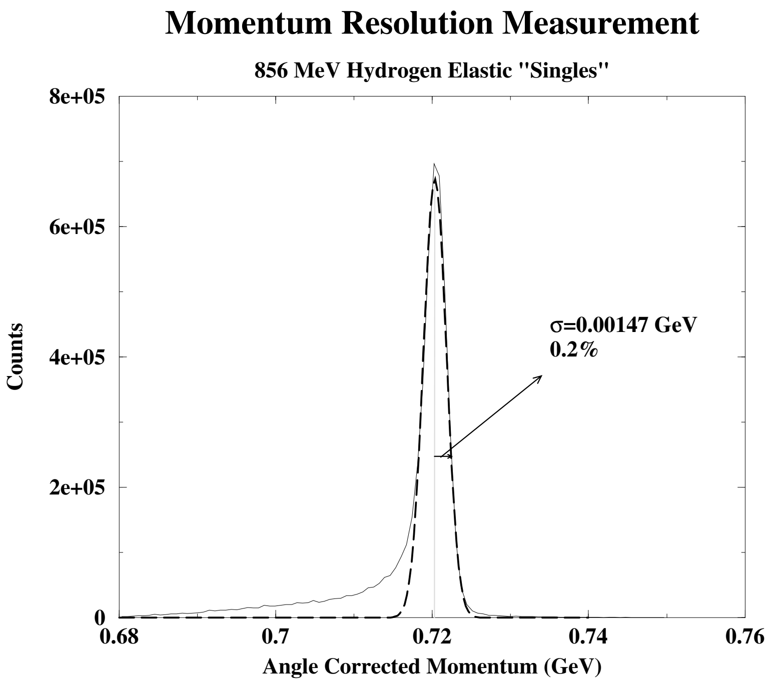

Figure 6.7: A gaussian fit to the elastic peak for the HRS at 856 MeV incident beam energy.

6.1.1 Reconstruction of the Photon Energy Spectrum, E_γ

The raw data, once processed, has many events which are undesirable. Most of these are simply background events which must be cut away. Thus "cuts" are applied to the various reconstructed kinematic quantities. Cuts are logical conditions placed on variables in an "n-tuple" or array of variables. These logical conditions restrict which events are subsequently analyzed.

6.1.1.1 Collimator and Exit Dipole Cuts

The first set of cuts are designed to eliminate stray events. These events may be events which "punch through" the high density collimator or through unshielded couplings between magnets and the detector shield house. To find where events come from they must be tracked through the drift chambers. These tracks provide the path the particle was following when it arrived at the focal plane of the spectrometer. From this, the particles' tracks can be transformed,through a matrix which defines the reverse through the optical elements, back to the image source (target).

The particle tracks in Hall A are found from the VDC information. From the drift times, a distance perpendicular to the anode wire to the point where the incoming particle passed, leaving electrons behind, can be calculated. Five of these "perpendicular distances" are found, one for each of the five wires nearest which the track passed. Fitting a straight line to these distances gives the intercept of the particle path with the wire plane. This process is repeated for each plane in each chamber yielding two pair of spatial coordinates for the incoming particle's path [54].

In Hall C the drift chambers provide tracking information as well. The Hall C tracks are found by first finding the position where the particle passed through the drift chamber. For each wire, the distance at which the particle passed is determined [59]. From these determinations in each plane, a set of "hits" called "space points" in each drift chamber is identified. Using these space points a "stub" or line through the points is fit. Various combinations are tried until the fit with the lowest χ^2, or mean square deviation between the fit line (stub) and the measured point, is found [59]. This procedure is performed in each drift chamber. The particle track is found by determining which pair of stubs, one in each chamber, are consistent with each other (for example they must be colinear). Further information on Hall C tracking can be found in Ref. [59].

Geometry cuts are applied to the data using the tracks and the angle the tracks make with the "central ray" through the spectrometer (where the angles are given by $\frac{dy}{dz}$ and $\frac{dx}{dz}$, where z is the direction of the central ray, in the small angle approximation). The entrance collimator can be reconstructed using the target angles ($\frac{dy_{tar}}{dz}$ is the in plane angle $\frac{dx_{tar}}{dz}$ is the out of plane angle) and the target position y_{tar} (y_{tar} is the target length projected into the spectrometer coordinate system). Plotting $\mathcal{L}\frac{dy_{tar}}{dz} + y_{tar}$ *versus* $\mathcal{L}\frac{dx_{tar}}{dz}$ where $\mathcal{L}$ is the distance from the target to the spectrometer entrance (166.37 cm in Hall C, 110.9 cm in Hall A) the entrance collimator can be imaged. A series of cuts in $\mathcal{L}\frac{dy_{tar}}{dz} + y_{tar}$ and $\mathcal{L}\frac{dx_{tar}}{dz}$ can be created and applied to all data which eliminate events which are outside of the entrance boundaries.

In Hall C a second set of geometrical cuts were applied at the entrance to the detector hut, and the dipole exit. A set of cuts at the focal plane projected to 750 cm back from the focal plane to an apparent focus near the dipole exit allowed for the placement of logical cuts on focal plane variables. These cuts were able to eliminate events which "punched through" a relatively unshielded vacuum coupling collar between the dipole and the shield house.

6.1.1.2 Particle Identification

Once stray events were removed the task of identifying which particles are protons became paramount. As previously discussed in section 5.3.3.3 pions were removed using Čerenkov detection in Hall C. The numbers of pions present were very small (<0.2%) and the inability to detect them in Hall A was not detrimental.

The next important determination was the difference between protons and deuterons. This separation was attempted using time of flight for each event recorded, and the measured momentum for the event (extracted from the particle tracking) to reconstruct the particle mass. Particle mass, m, is reconstructed as follows:

$$m^2 = p^2(\frac{1}{\beta^2} - 1). \tag{6.1}$$

In Eq. 6.1 p is the particle momentum and β is the particle velocity, both in natural units, which leaves m^2 in units of GeV^2. Time of flight, from which β is extracted, refers to the time it takes for a particle to travel from one hodoscope plane (or $x - y$ pair in Hall C) to the other. If the resolution is sufficient, or the flight path is long enough Eq. 6.1 gives good separation of protons and deuterons (see Figs. 6.8 and 6.9). If either condition is not true, however, then determining the difference between a proton and a deuteron, expecially when their velocities are very close as they are in the E96-003 Hall C data, becomes a problem (see Fig. 6.10). The determination of proper mass cuts for particle identification, and even whether or not applying such cuts is acceptable, becomes a challenge involving both cut identification and background suppression (see Fig. 6.12). In Hall C E96-003 proper cuts were found using the background suppression techniques discussed in section 6.1.2.1. In Hall A E99-008, however, the decision was made to avoid placing mass-squared particle identification cuts beause the timing resolution in single arm mode is quite poor in general, despite clear peaks in very low-momentum kinematic settings (see Figs. 6.11 and 6.9).

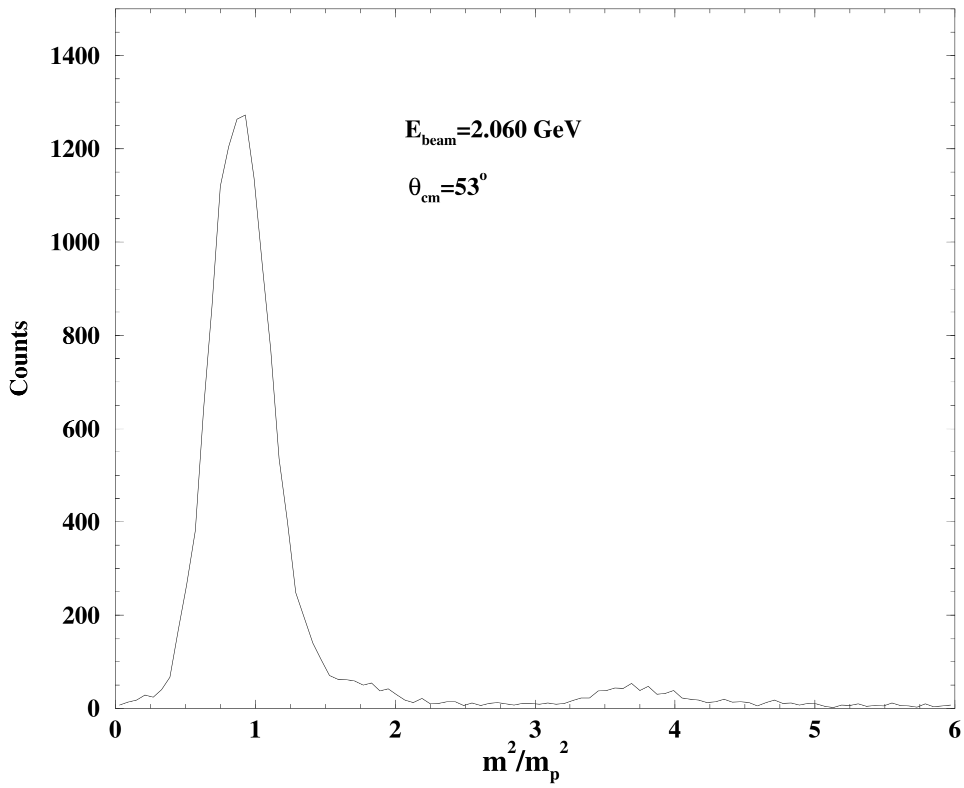

Figure 6.8: Mass squared peak normalized to proton mass for Experiment E96-003. These data were taken at a beam energy of $E_{beam} = 2.060$ GeV at a center-of-mass angle of $\theta_{cm} = 53°$. Notice the reasonably clear separation of protons and deuterons.

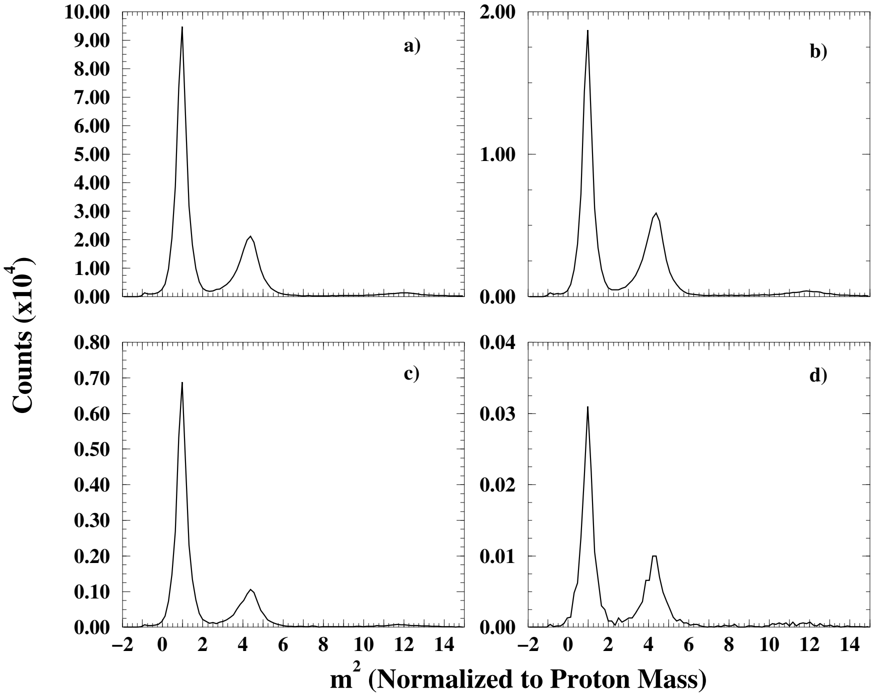

Figure 6.9: Mass squared plot, normalized to the proton mass for E_b=2500 MeV at θ_{cm}=143° for Experiment E99-008. Plots a-d are LD_2 radiator in, LH_2 radiator in, LD_2 radiator out, and LH_2 radiator out, respectively. Notice clear proton, deuteron, and a hint of triton peaks in the spectra. The deuteron and triton peaks are not at 4 and 9 respectively because of the time-of-flight calibration method.

In Hall C the time-of-flight peaks, β, were well described by gaussian distributions. Using lower energy, E_{beam}=2.606 GeV, deuteron photodisintegration data, the mass squared spectra were fit using Eq. 6.1. The background was subtracted resulting in the spectrum in Fig. 6.12. To this spectrum was then fit two gaussians, one was for the protons, and a second to search for the presence of a deuteron peak. From these fits at time t and a standard deviation (time resolution) σ were extracted for the HMS time-of-flight resolution. The timing resolution was used as the starting resolution in the higher energy data proton peak fits (see Fig. 6.12). The average time-of-flight (centroid of the gaussian distribution) was allowed to be adjusted by the fitting procedure because of difficulties in obtaining a clean sample of protons of appropriate momentum for time-of-flight calibration (see Appendix B for a brief description of the time-of-flight calibration procedures). Figure 6.12 shows an example of a mass

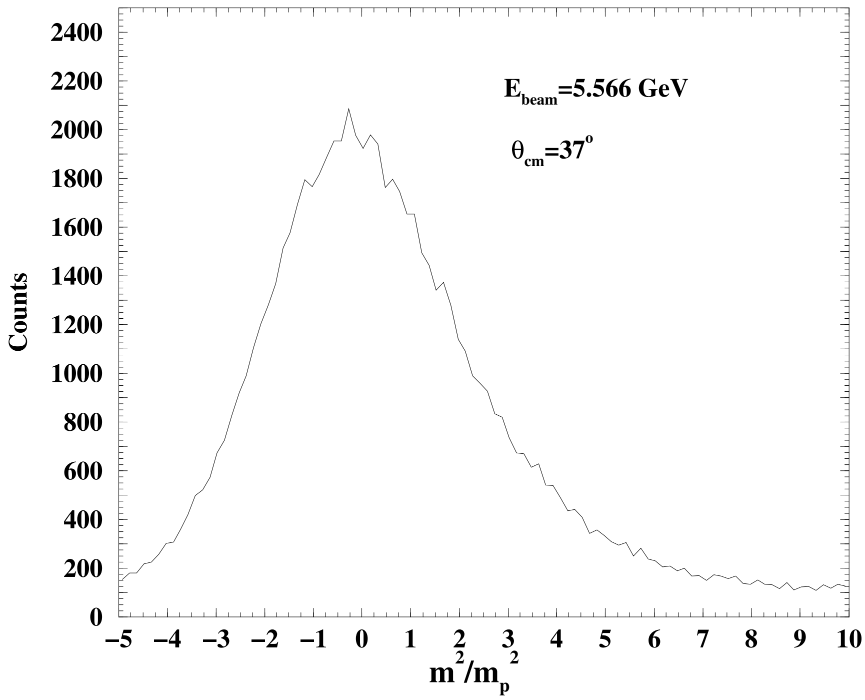

Figure 6.10: Mass squared peak normalized to proton mass for Experiment E96-003. These data were taken at a beam energy of $E_{beam} = 5.566$ GeV and a center-of-mass angle $\theta_{cm} = 37°$. Notice there is no clear separation of protons from deuterons.

squared spectrum. The grey shaded region shows the area used in the analysis. These cuts are at 2.5σ of the mean mass squared value. This leaves out approximately 2% of the photoprotons, which are taken into account during yield normalization.

Systematic error on the particle identification cut was assessed by placing a series of cuts at 1σ, 1.5σ, 2σ, and 2.5σ of the fitted gaussian. The laboratory cross section was then calculated with each cut and compared to the cross section calculated at 2.5σ, the analysis cut, times a factor A which was the area found by integrating the gaussian over the standard deviation chosen. For example, to compare the 1.5σ cut the area of the gaussian between $\pm 1.5\sigma$ would be calculated to give A. The comparison would then determine to what extent $A \times \frac{d\sigma_{2.5\sigma}}{d\Omega_{lab}} = \frac{d\sigma_{1.5sigma}}{d\Omega_{lab}}$. The average of these comparisons gave an average discrepancy of 3% which was applied as the systematic error.

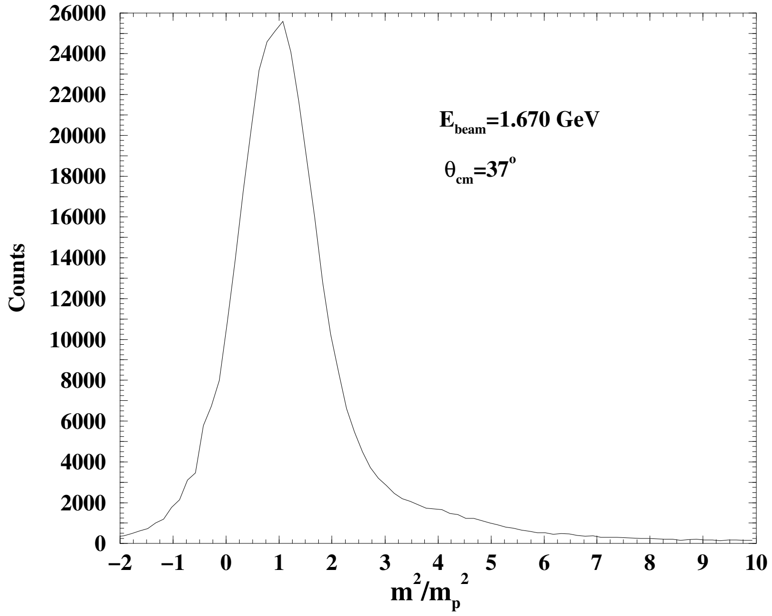

Figure 6.11: Mass squared peak normalized to proton mass for Experiment E99-008. These data were taken at a beam energy of $E_{beam} = 1.670$ GeV and a center-of-mass angle $\theta_{cm} = 37°$. Notice there is no clear separation of protons from deuterons.

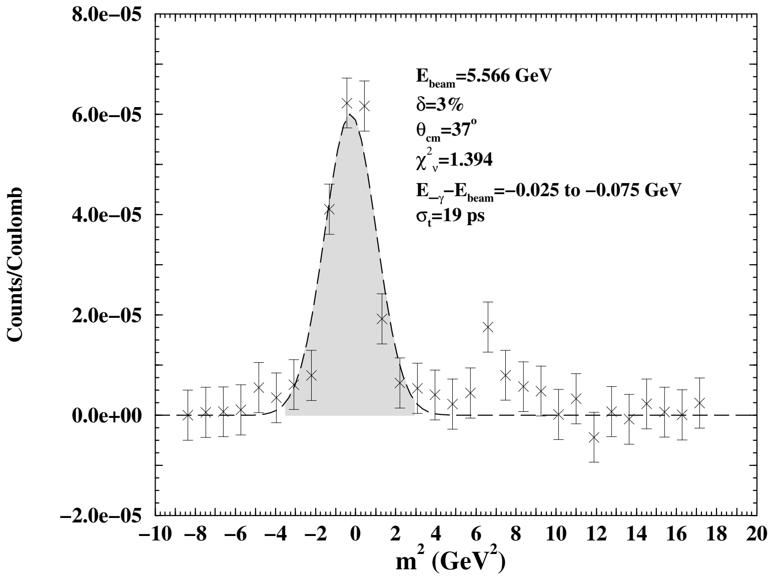

Figure 6.12: Mass squared peak normalized to proton mass for Experiment E96-003. This is a background subtracted mass squared spectrum. Notice a clear proton peak with no apparent deuterons remaining. The fitted gaussian was used to determine the mass squared PID cuts used in the analysis.

6.1.1.3 Remaining Analysis Cuts

Two cuts remain which must be described. The first is a cut on the momentum acceptance of each spectrometer. The second is the determination of the usable target length.

A cut on spectrometer momentum acceptance was made to ensure events being considered passed through the well-known region of the spectrometer. In Hall A a cut of $\pm 4.5\%$ in δ ($\delta = \frac{p-p_0}{p_0}$, where p_0 is the spectrometer central momentum) was used since this is the total useful region in δ. In Hall C a δ cut of $\pm 8\%$ was used.

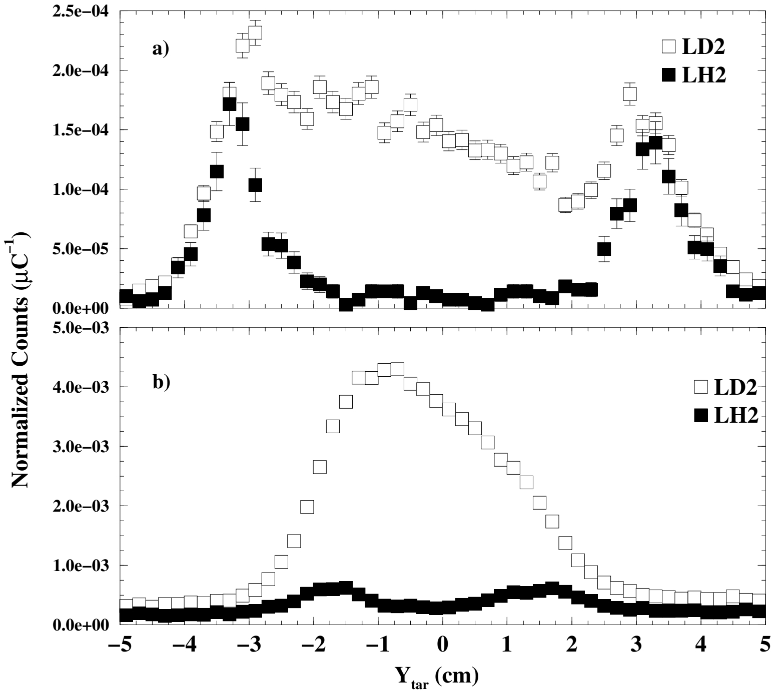

Figure 6.13: Examples of the Y_{target} spectra at a) E_b=5.066 GeV at $\theta_{cm} = 70°$, the lowest momentum run in E96-003, and b) E_b=5.566 GeV at $\theta_{cm} = 37°$, one of the worst background cases.

The target length was determined by placing cuts at or near the aluminum target windows. These windows were found by looking at reconstructed target spectra (see Figs. 6.13 and 6.14) from data taken on the hydrogen targets. In Hall C, the cuts were placed on the target end caps themselves to improve statistics. In Hall A, for data

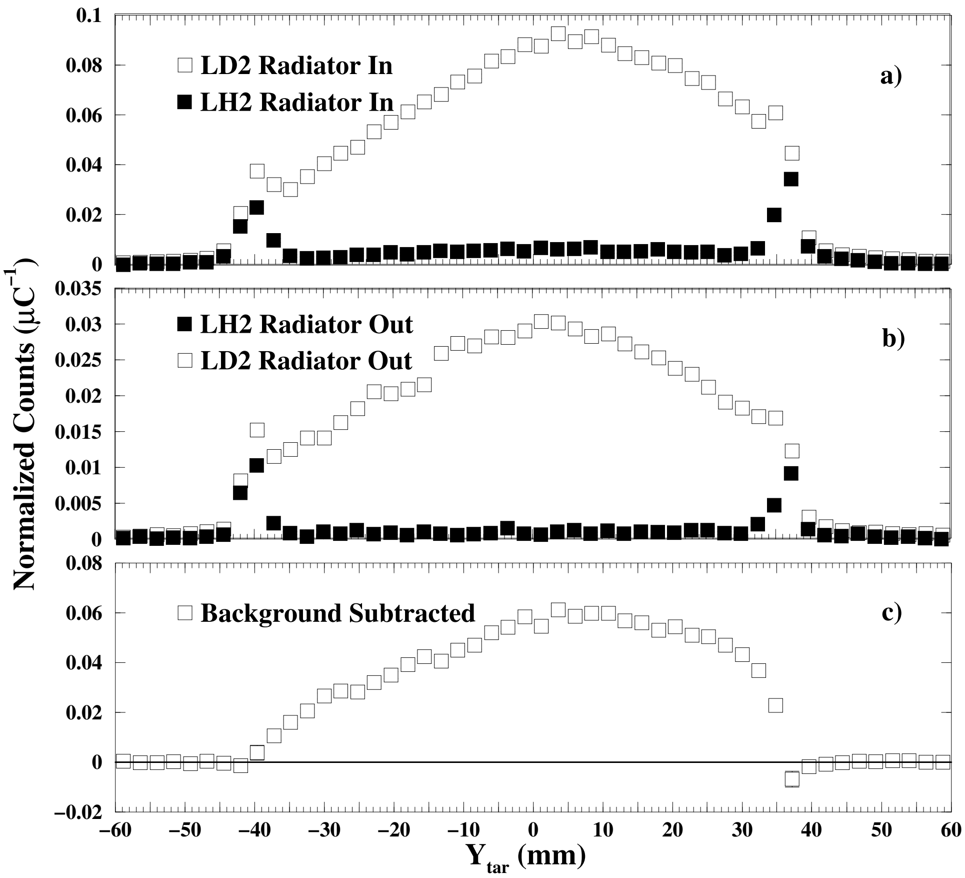

Figure 6.14: Example $Y_{\rm target}$ from the Hall A HRS for E_b=1670 MeV at $\theta_{\rm cm} = 53°$. Figures a) and b) show the agreement of the LH_2 and LD_2 target spectra after scaling, as described in the text, for radiator in and radiator out respectively. Figure c) shows the result of the background subtraction in $Y_{\rm target}$.

where the full 15 cm of target can be imaged (the HRS can only see approximately ±5 cm in y_{target} [60]) cuts were placed as close to the end caps as possible without including endcap events. In Hall A the end caps could be very clearly seen for angles were y_{target} ($y_{target} = \frac{\mathcal{L}}{\sin(\theta_{HRS})}$) is $< \pm 5$ cm. At larger angles, cuts were placed at ±4 cm in y_{tar} to avoid edges of the HRS' target acceptance. Error on the target length was found by fitting gaussians to the peaks in the spectra caused by the end caps. This provided both the location of the end caps (the centroid of the gaussian) and the standard deviation of the gaussian was used as the error in the ability to apply the target length cuts. This error amounted to about 3% in the worst case for E96-003 and 1.3% for E99-008. In both cases target length cuts were important for proper normalization and background suppression.

6.1.2 The E_γ Spectrum

The spectrum which is used in extracting the photoproton yield is the reconstructed photon spectrum or E_γ spectrum. The real bremsstrahlung photons which impinge upon the target have a maximum energy at the beam energy (called the end point), but, continuous spectrum of energies is produced. Since total four momentum (the vector $\tilde{\mathrm{P}}$=(E,P$_x$,P$_y$,P$_z$)) must be conserved, from the energy and momentum of the detected protons the energy spectrum of the incident photons can be reconstructed. The total momentum of the system is:

$$\tilde{\mathrm{P}}_\gamma + \tilde{\mathrm{P}}_d = \tilde{\mathrm{P}}_p + \tilde{\mathrm{P}}_n. \tag{6.2}$$

By employing conservation of momentum and the knowledge that the square of a four vector is invariant (the same in all reference frames) and equal to the square of the mass (i.e. $\tilde{\mathrm{P}}_n^2 = m_n^2$), Eq. 6.2 can be solved for E_γ, the incident photon energy:

$$E_\gamma = \frac{\frac{1}{2}(m_p^2 + m_d^2 - m_n^2) - m_d E_p}{E_p - [P_p \cos(\theta_p) + m_d]}. \tag{6.3}$$

In Eq. 6.3 the m_i's are the particle masses (proton, neutron, and deuteron), E_p is the proton energy, P_p the proton momentum, and θ_p the proton *laboratory* angle. Using these quantities which are uniquely defined in both E96-003 and E99-008, the photon energy spectrum can be reconstructed.

6.1.2.1 Determination of the Photoproton Yield

Once the photon energy spectrum is reconstructed, the photoproton yield for deuteron photodisintegration can be extracted. This yield is what, when properly normalized, will be used to determine the differential cross section. The first step in determining the useful proton yield is suppression of background (unwanted) events. Next the proper region of the E_γ spectrum must be taken, that is only those events which come from $\gamma + d \rightarrow p + n$ should be used.

Cuts are applied (See section 6.1.1) to the data to reduce the numbers of background events present in the data. The effect of each cut on background levels is assessed by generating E_γ spectra. Each set of cuts has a different effect on the data. In E96-003, the data had very high backgrounds. Figure 6.15 shows the effects of the cuts on backgrounds for a 5.5 GeV, $\theta_{cm} = 37°$ data set from E96-003. Background rates were not as high in E99-008, partly because of the lower beam energies used. Nevertheless, the cuts placed on the data have the same, if somewhat less dramatic effect. Photon energy spectra were generated for both hydrogen and deuterium data.

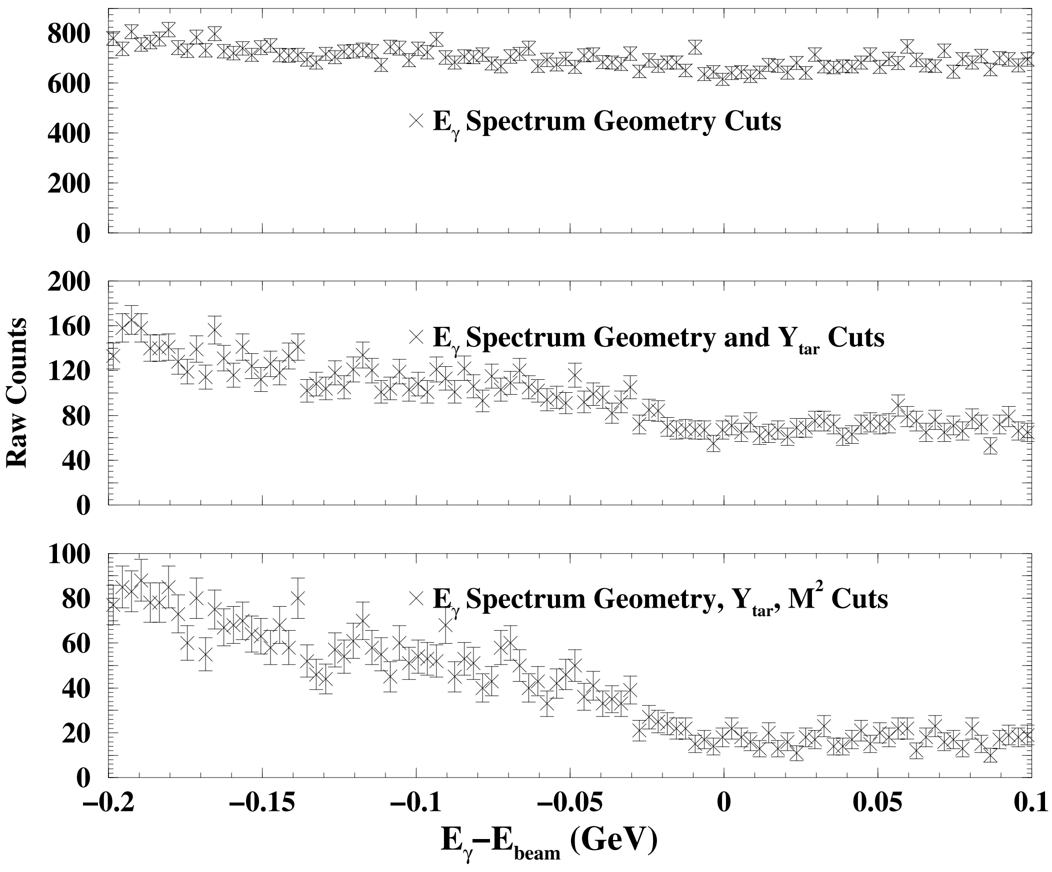

Figure 6.15: E_γ spectra for JLab Experiment E96-003 at E_b=5.566 GeV at $\theta_{cm} = 37°$. The three panels show the effects of adding analysis cuts to the data set.

At this point a distinction between the two techniques used in E96-003 and E99-008 to assess and eliminate background must be addressed. In experiment E96-003, where photon energies reached 5.5 GeV, the deuteron photodisintegration cross section is quite small. Thus it took a relatively long time (up to 5 to 10 days) to measure a single point at the maximum energy. Time constraints required a change in the types of data collected. Previously the experimental procedure required that data with both the hydrogen and deuterium targets be taken with the copper bremsstrahlung radiator in and out of the beam line. This procedure permitted the assessment of events caused by electrodisintegration of the deuteron (Data was taken following this "standard" procedure in E99-008.). This procedure is relatively time consuming, as experimental time would have been invested in "radiator out" studies at a loss of a factor of two in stastistical accuracy. The solution was to take data only with the "radiator in" and compensate for the electrodisintegration events using "virtual photon theory" when "counting" the total number of photons used in the experiment. The use of virtual photon theory in experiment E96-003 will be addressed in section 6.2.3.4.

Once the E_γ spectra have been generated, they must be properly normalized. Normalization of the spectra puts them into the "correct units" for comparison to each other. That is, at each energy point, the total number of events at that energy are divided by the total number of electrons used in the experiment (charge) and the computer "dead time" or the fraction of the time the computer was unable to accept and process events. By correcting for dead time, or more accurately "live time", the fraction of the time the computer was able to process events, ensures that the real number of events generated by the reaction are used. This procedure converts the spectra into units upon which arithmetic operations can be performed. The hydrogen spectra are subtracted from the deuterium spectra. The end result should produce a photon spectra which has a clear end point at the beam energy (or 0 on a scale in which the x-axis is $E - E_{beam}$) with no events remaining above the end point. Events in this energy (above the end point) are kinematically forbidden and any remaining events are an indication that the background subtraction is incomplete.

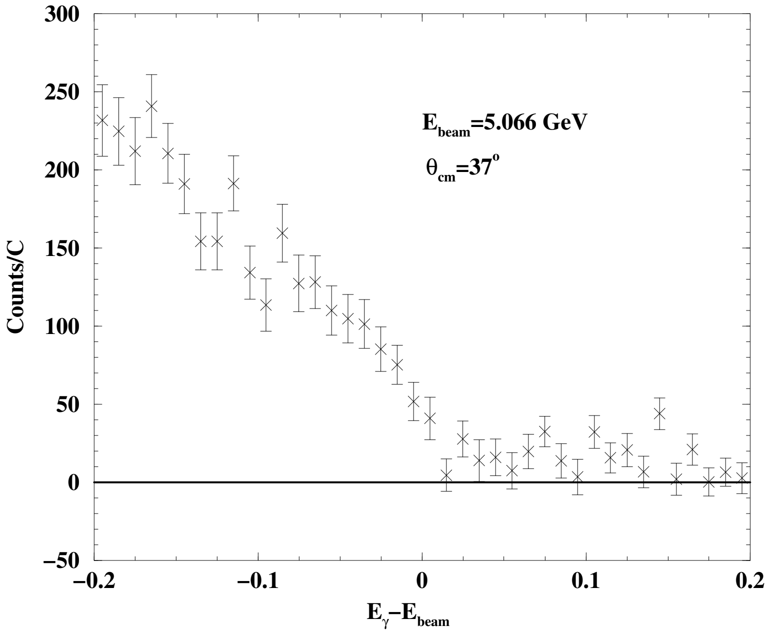

Figure 6.16: E_γ spectra for JLab Experiment E96-003 at E_b=5.066 GeV at $\theta_{cm} = 37°$. The data are subtracted without any compensation for background in the kinematically forbidden region above the end point.

It is frequently the case that a simple subtraction of the hydrogen spectra from the deuterium spectra is incomplete (see Fig. 6.16). Scale factors are applied to hydrogen E_γ spectra for background suppression. These scales are found in one of two ways:

1. The number of events above the end point in a hydrogen E_γ spectrum are compared to the number of events in the same region in a corresponding deuterium spectrum. Here it is assumed that the energy dependence of the background is the same in a deuterium target run as it is in a hydrogen target run. Because of statistical effects in the data for E96-003, an averaging procedure was applied when obtaining the scale factor. Because these scales were frequently imperfect, a small flat background was also subtracted from the E96-003 data. In this case, it is assumed that the background is energy independent.

2. A background suppressed y_{tar} spectrum is generated (i.e. $y_{tar_d} - y_{tar_h}$). A channel of the suppressed y_{tar} spectrum, which is near a target endcap, is observed while a scale (s_1 for radiator-in data, s_2 for radiator-out data) is adjusted. The proper scale is determined when the observed "endcap channel" is equal to zero. This technique was only employed for E99-008 data at forward angles where the target endcaps were visible.

These scale factors help suppress kinematically forbidden background and E_γ spectra such as those in Figs. 6.17, 6.18, 6.19, and 6.20 are produced.

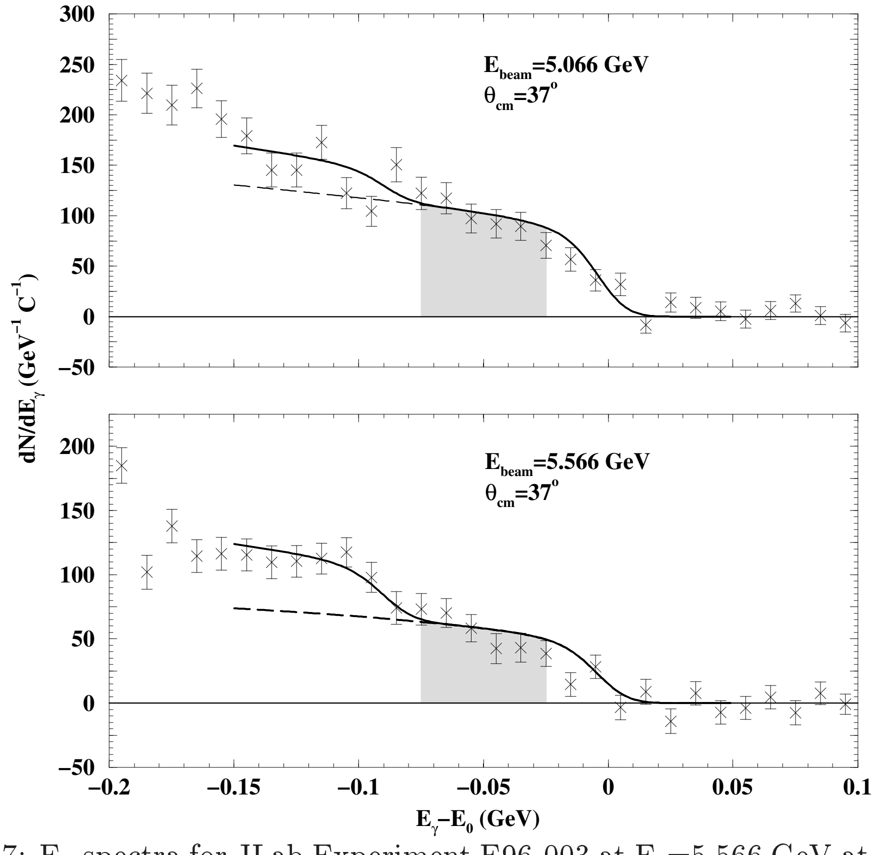

Figure 6.17: E_γ spectra for JLab Experiment E96-003 at E_b=5.566 GeV at $\theta_{cm} = 37°$, top panel, and $\theta_{cm} = 53°$, bottom panel. The spectra are normalized to collected charge and are background subtracted as described in the text. The solid curve illustrates the clear end points in these spectra, as well as the threshold for π^0 production. The grey shaded area represents the region in E_γ used to calculate the photoproton yield.

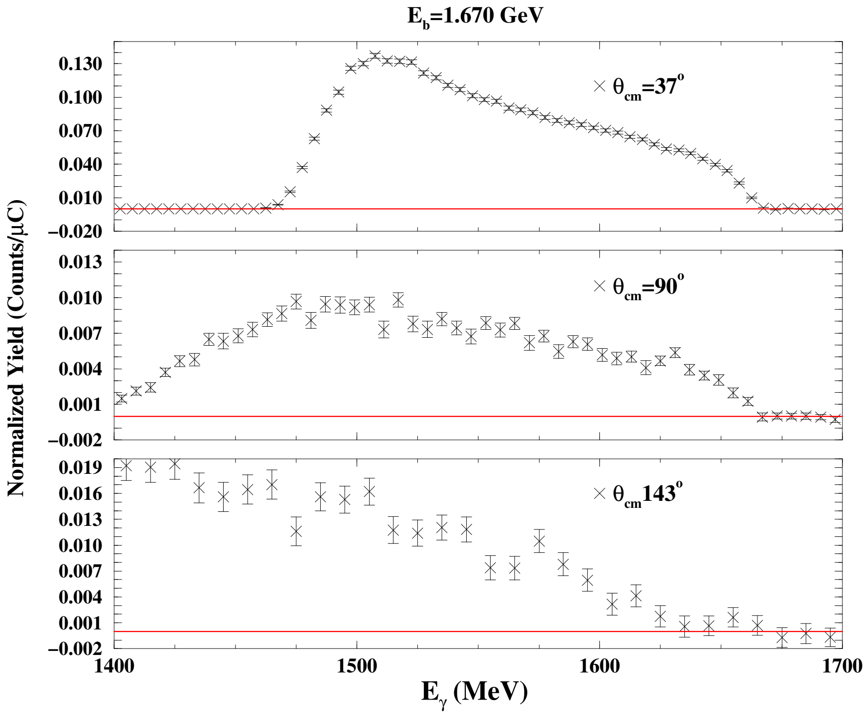

Figure 6.18: E_γ spectra for E_b=1.670 GeV at θ_{cm} = 37°, 90°, and 143°.

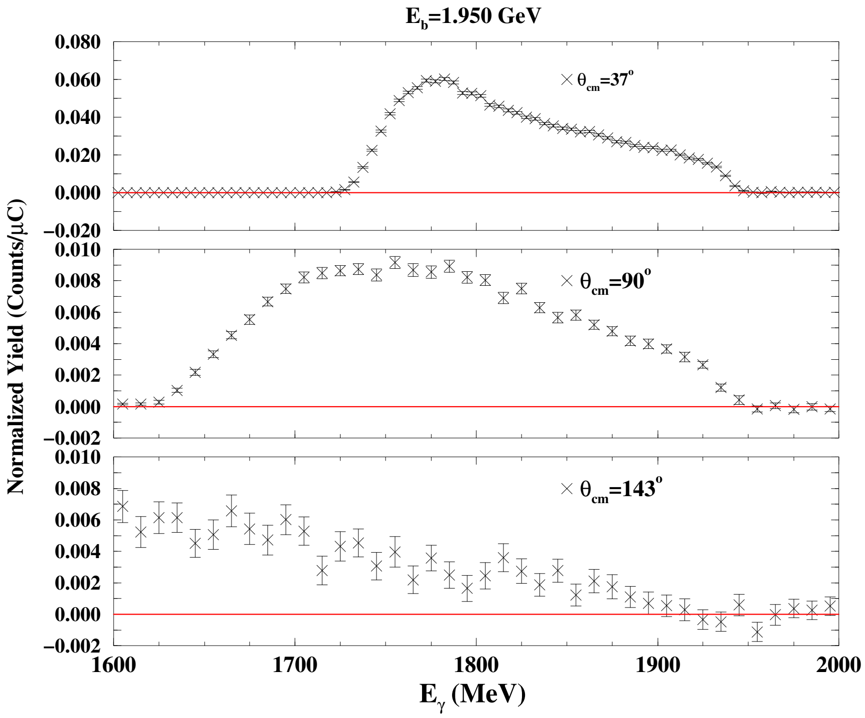

Figure 6.19: E_γ spectra for E_b=1.950 GeV at θ_{cm} = 37°, 90°, and 143°.

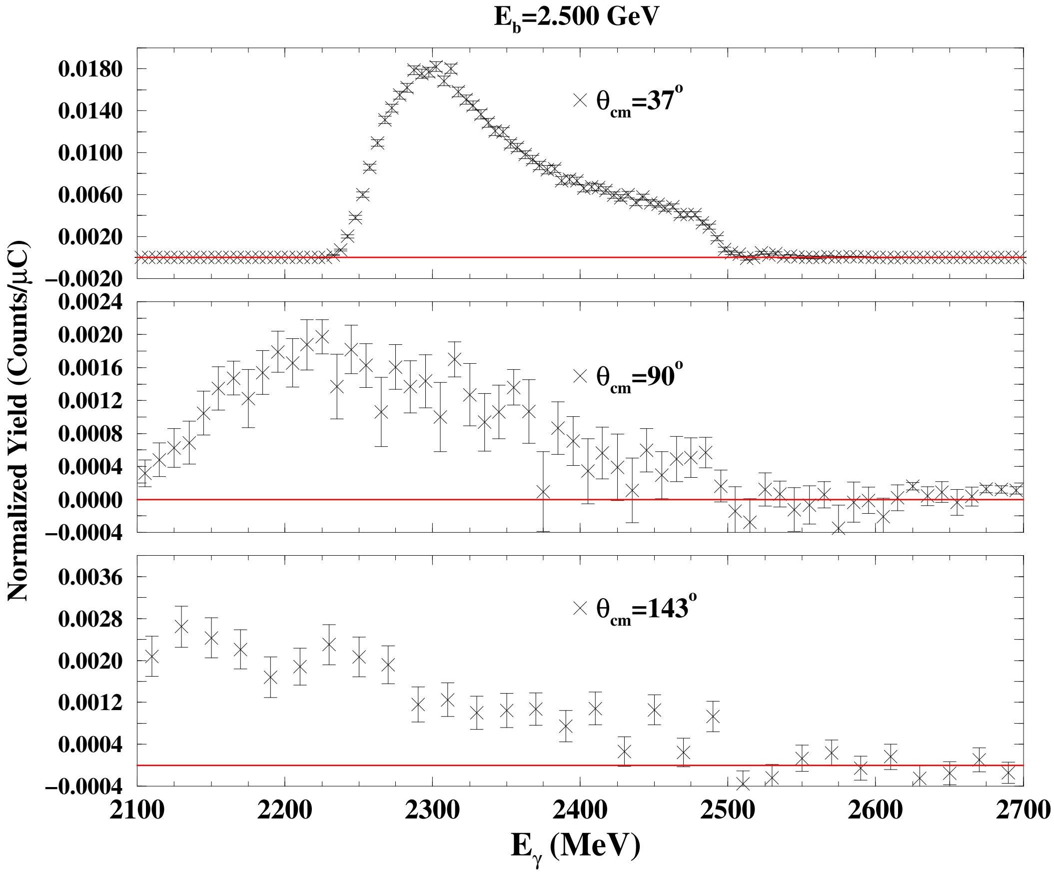

Figure 6.20: E$_\gamma$ spectra for E$_b$=2.5 GeV at $\theta_{cm} = 37°$, 90°, and 143°.

Systematic error in the background measurements came about in one of three forms. For the E96-003 data and the data at $\theta_{cm} = 90°$ through 127°, the scaled background suppression method was compared to a flat background suppression method, where an average background, sampled from the kinematically forbidden region, was subtracted from the simply subtracted spectra (i.e. just deuterium spectrum-hydrogen spectrum). Variations between these two methods were about 3% in the worst case for E96-003 and 4% for E99-008 for the angles listed above. For the forward angle data in E99-008, the scale factors s_1 and s_2 were adjusted until the change in the observed channel from zero was one standard deviation of the statistical error on the channel. The cross section was then calculated with the scale factors varied by the difference between the scale factors at zero and the scale factors at one standard deviation. The resulting error was just over 1%. For the backward angle 143°, where a target position dependent background was observed, it was assumed that this background is the effect of two-step processes *in the aluminum target material* rather than in deuterium. The evidence for this can be seen in Fig. 6.21, where the photoproton background has a similar dependence on the position along the target when no deuterium is present. In this case the hydrogen background runs are scaled and subtracted from the deuterium runs to eliminate the kinematically forbidden background. Because multi-step background from aluminum appears to be dominant, the two-step background from the deuterium is ignored.

A calculation was then made, using the quasi-deuteron model, to estimate the background yield one could expect from two-step processes in deuterium. The quasi-deuteron model provides a relationship between the density of "deuterons" (in atoms per barn), $n_{d_{Al}}$, in a sample of, for example aluminum, to the density (in atoms per bar) of the aluminum in the sample, n_{Al} [69]:

$$n_{d_{Al}} = \frac{\mathcal{L} N Z}{A} n_{Al}. \tag{6.4}$$

In Eq. 6.4 $\mathcal{L}$ is a coefficient which relates the deuteron photodisintegration reaction to the aluminum photodisintegration reaction and was measured to be 2.4. The quantities A, N, and Z are the atomic mass, neutron number, and proton number for the sample (aluminum) respectively. By comparing the density calculated by Eq. 6.4 to the density of deuterium in the target, the systematic error was estimated to be 5.2% due to ignoring two-step processes in the background subtraction at $\theta_{cm} = 143°$.

6.2 Determination of the Differential Cross Section

Once the photoproton yield is determined, the differential cross section can be calculated. The calculation of the differential cross section takes place in several steps.

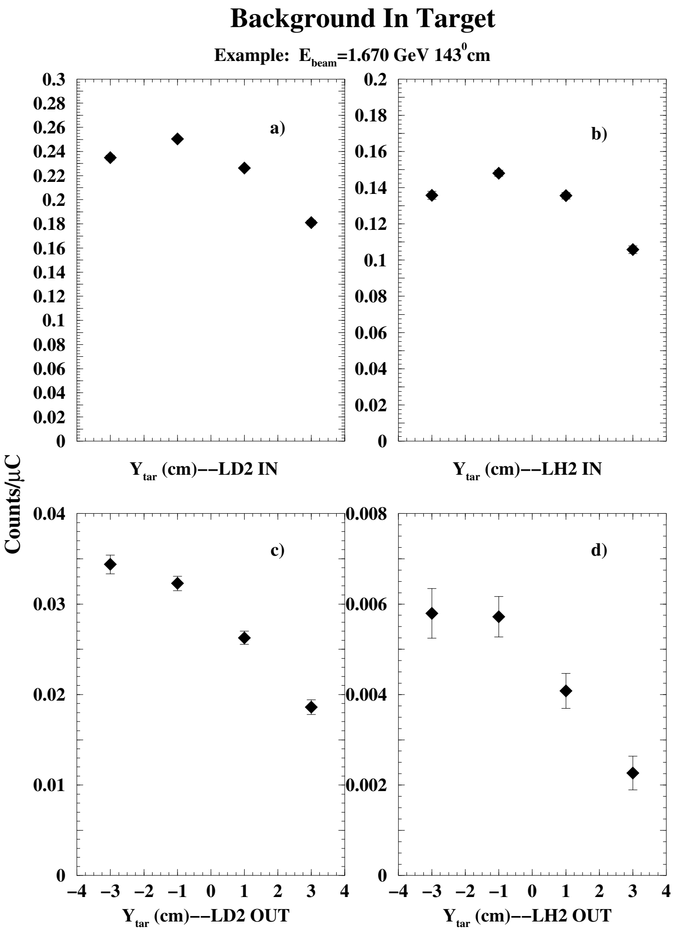

Figure 6.21: Examples of the $\mathrm{Y}_{\mathrm{target}}$ spectra with data taken from the region of the E_γ spectrum which is kinematically forbidden. The data are from $E_b = 1.670$ GeV at $\theta_{cm} = 143°$. Panel a) liquid deuterium target, radiator in; b) liquid deuterium, radiator out; c) liquid hydrogen, radiator in; and d) liquid hydrogen, radiator out. Notice the similar, position dependent pattern to the background.

The first step is the extraction of the photoproton yield from the reconstructed E_γ spectra. Next the raw yields must be normalized in preparation for background subtraction. This subtracted yield must then be converted into a laboratory differential cross section, $\frac{d\sigma}{d\Omega_{lab}}$. This laboratory differential cross section must then be converted into center of mass and invariant differential cross sections.

6.2.1 Photoproton Yield for E96-003

For E96-003, the number of events which came only from the reaction $\gamma + d \rightarrow p + n$ were quite small. At best, a few hundred events were collected in all of the individual runs (time periods during which data were taken) combined. The individual runs each lasted anywhere from 30 minutes to 45 minutes on the average. For this case, the photoproton yield in for each target type is extracted according to the following form,

$$Y_{d \text{ or } h} = \frac{\sum_{i=1}^{r} N_{i_{d \text{ or } h}}}{\sum_{i=1}^{r} Q_i \ell_i}, \tag{6.5}$$

where r is the number of runs in of each target type; $\sum Q_i \ell_i$ is the sum over the charge (See Chapter 5 Section 5.1.3 and live time (see Section 6.1.2) for each run i; and N_i is the number of photoprotons in the E_γ window for run i. Because the statistics (number of counts) was very low, the number N_i is simply the total number of counts in the E_γ window. The statistical accuracy was too poor to divide the energy window up into smaller sections called "bins."

Equation 6.5 produces two "partial yields", Y_d and Y_h. The background suppressed photoproton yield is then determined:

$$Y = Y_d - Y_h \frac{Y_{d_{back}}}{Y_{h_{back}}} - F.B.. \tag{6.6}$$

In Eq. 6.6 the term $\frac{Y_{d_{back}}}{Y_{h_{back}}}$ is the scale factor used to suppress the kinematically forbidden background. The yields are found using Eq. 6.5 with an E_γ window taken above the reconstructed bremsstrahlung end point for each data type.

6.2.2 Photoproton Yield for E99-008

For the data in E99-008, the procedure is much the same with a few exceptions. First, of course, there are four run types which must be taken into account. Also, the statistical accuracy was much higher, so the photon energy window from which the photoproton data were extracted can be broken up into a series of 5 MeV bins.

This permits a more sophisticated averaging technique to be used. For E99-008 the partial yields were found according to the following form,

$$Y_{d \text{ or } h_j} = \frac{\sum_{i=1}^{r} w_j N_{ij}}{\sum_{i=1}^{r} w_{ij}}, \tag{6.7}$$

where j is a 5 MeV bin within the E_γ window used and $w_{ij} = \frac{1}{\sigma_{ij}}$ ($\sigma_{ij} = \sqrt{N_{ij}}$), is the weight applied to obtain the weighted average in each bin. Equation 6.7 is applied to each of the four run types generating four partial yields, two radiator in yields $Y_{d_{in}}$ and $Y_{h_{in}}$, and two radiator out yields $Y_{d_{out}}$ and $Y_{h_{out}}$.

The photoproton yield in each 5 MeV bin, j, is then extracted according to the following method:

$$Y_j = (Y_{d_{in}j} - s_1 Y_{h_{in}j}) - F(E)_j (Y_{d_{out}j} - s_2 Y_{h_{out}j}). \tag{6.8}$$

In Eq. 6.8 $F(E)$ is a function which compensates for the changes in the beam energy profile as a result of having passed through the radiator. The factors s_1 and s_2 are the scale factors described in Section 6.1.2. This correction factor will be discussed further in Section 6.2.3.3.

6.2.3 Normalization of the Photoproton Yield

Converting the photoproton yield into a laboratory differential cross section proceeds along the following lines, which are largely the same for both E96-003 and E99-008. First the photoproton yield is normalized to detector and cut efficiencies and the transmission of the protons throught the detector stack. Second, the number of photons in the E_γ window, per electron, are calculated and applied to the normalized photoproton yield. This produces the yield/photon. This yield is then divided by the target thickness (determined by y_{target} cuts), the density of the liquid deuterium, and the solid angle subtended by the spectrometer (determined by Monte Carlo). This generates the differential cross section in units of barns (10^{-24} cm^2) per steradian.

6.2.3.1 Efficiencies

Various efficiencies were applied to the data. The first is a detector efficiency, the "tracking efficiency." The tracking efficiency is the ability of the drift chambers to reconstruct a particle track. A well defined approach was used in Hall C for the determination of the tracking efficiency for E96-003. In Hall A, the tracking efficiency has been studied using various settings for the VDC's and the tracking efficiency estimation was made from the results of the study.

The procedure used in Hall C required the use of both the drift chambers and the scintillator hodoscopes. The data set which was used was the $E_{beam} = 2.060$ and 2.567 GeV data taken for the purposes of checking out the experimental procedure. Only those scintillator hodoscope paddles which defined a small fiducial area surrounding central ray of the spectrometer were used in the analysis. This defined a "good" event. A scaler was used to count the number of triggers which passed through fiducial area. A set of cuts on the shower counter energy fraction (> 0.45) and a cut on β, the particle speed (> 0.85) were used for particle identification. The number of tracks detected by the drift chambers which met these criteria were then counted and the tracking efficiency was determined:

$$\epsilon_{tr} = \frac{\text{Number of Tracks Detected}}{\text{Number of Triggers Detected}}. \tag{6.9}$$

The number of planes used to make the track (5 or 6) and the number of scintillator planes (3 or 4) to make the trigger were varied, to check for variations. The tracking efficiency for E96-003 was determined to be $98\% \pm 2\%$ by this method [12].

To estimate the tracking efficiency in the Hall A VDC's information from the study in Ref. [70]. Extensive detail on the testing of the VDC's is available in this reference. For the setup which was used during E99-008, the study data indicates that the tracking efficiency should be 99%. The rates in this experiment were only a few hundred Hz, and after all other corrections were made, through comparison with previous data no sizable discrepancy with this estimate was observed.

6.2.3.2 Proton Attenuation

A reasonably large correction to the data ($\sim 10\%$) is the attenuation of the photo-protons through absorption in materials as they travel from the target through to the last scintillator used in the trigger. Tables 6.2 and 6.1 show the estimated absorption values for protons traveling through the various materials in the target-spectrometer system.

HRS Proton Absorption					
Absorber	Density	Thickness	$\bar{\lambda}$	X	$X/\bar{\lambda}$
	(g/cm^3)	(cm)	(g/cm^2)	(g/cm^2)	($\times 10^{-3}$)
Al Target Window	2.7	0.01	88.5	0.027	0.31
Al Chamber Window	2.7	0.0330	88.5	0.0892	1.01
Kapton (Spectrometer Entrance)	1.42	0.0254	73.1	0.0361	0.49
Titanium (Spectrometer Exit)	4.54	0.01	102.4	0.0461	0.45
Air (Spectrometer Exit to VDC1)	0.00121	80	75	0.0968	1.27
Mylar (Wire chamber –entrance/exit windows, –10 sheets$\times$2VDC's)	1.36	0.012	72	0.0167	0.23
VDC Wires (effective) 20μm W, 2 planes$\times$2 VDC's)	19.3	0.00004	147.7	0.0008	0.005
Ar/Ethane (62/38 by weight)	0.00107	20	85	0.002114	0.25
Polystyrene (scintillator S1)	1.03	0.507	70.2	0.523	7.45
Čerenkov Aerogel	0.1-0.2	15	78	1.5-3	19.23-38.46
Čerenkov Gas (CO_2)	0.001977	80	76.1	0.158	2.08
Air (VDC1 to S2)	0.00121	220.2	75	0.0226	3.5
Polystyrene (scintillator S2)	1.03	0.52	70	0.537	7.650
Total					44.0-63.2

Table 6.1: Absorbances of materials in the HRS and target materials other than cryogenic deuterium. Values for these materials are from reference [72].

The absorption was found by employing the following method. Using the nuclear interaction length, that is the mean free path between collisions, the proton absorption can be estimated. The mean free path λ can be found through the following expression,

$$\lambda \ (\mathrm{g/cm^2}) = \frac{\rho}{N_A \sigma}, \tag{6.10}$$

where ρ is a density in grams per mole, N_A is Avogadro's Number, and σ is the cross section for a scattering event to occur [71]. The mean free path used in the estimation of the proton absorption is the average of the mean free path between collisions, λ_T, and the mean free path between inelastic collisions, λ_I. Values for these quantities for various materials are available in Ref. [71]. Combining this average, $\bar{\lambda}$, with the thickness, X, of the material (in grams per cm^2) though which the protons must pass, the ratio $\bar{\lambda}/X$ can be used in the following equation to produce the probability that the proton will be absorbed by the materials in the target-spectrometer system,

$$A = 1 - e^{-\sum_i \frac{X_i}{\lambda_i}}, \tag{6.11}$$

where the sum runs over all of the materials which are in the path of the recoil photoproton [12]. Tables 6.2 and 6.1 show the values for $\frac{X}{\lambda}$ for all materials excluding the cryogenic deuterium. The value for $\frac{X}{\lambda}$ for the deuterium was dependent upon the angle being measured and ranged from 13.6×10^{-3} to 21.5×10^{-3} for E96-003 and 10.9×10^{-3} to 37.1×10^{-3} for E99-008.

Summing the values of $\frac{X}{\lambda}$ and using Eq. 6.11, corrections to the differential cross section of not greater than 11% were applied. This method of estimating proton absorption has been compared to another method using electron-proton elastic scattering in coincidence. By comparison to these data, agreement with the method of Eq. 6.11 has been observed to be within 2% [73].

HMS Proton Absorption					
Absorber	Density	Thickness	λ	X	X/λ
	(g/cm^3)	(cm)	(g/cm^2)	(g/cm^2)	($\times 10^{-3}$)
0.005 in. Al Target Window	2.7	0.0127	88	0.0343	0.39
0.016 in. Al Chamber Window	2.7	0.0406	88	0.1096	1.24
Air	0.00121	$\sim$15	75	0.0182	0.24
Kevlar	0.74	0.0381	$\sim$70	0.0282	0.40
Mylar	1.36	0.0127	72	0.0177	0.25
Kevlar	0.74	0.0381	$\sim$70	0.0282	0.40
Mylar	1.36	0.0127	72	0.0177	0.25
Air (exit pipe to S2)	0.00121	$\sim$256	75	0.310	4.13
0.004 in Mylar (Wire chamber entrance/exit windows)	1.36	0.0102	72	0.0142	0.20
Sense Wires (effective) 25μm W, 12 planes	19.3	0.000076	147.7	0.00146	0.010
Field Wires (effective) 150μm Al/Au (99/1) –18 planes	2.70	0.0068	89.1	0.0184	0.21
Ar/Ethane (50/50 by weight)	0.00154	16.6	$\sim$70	0.0256	0.36
Field Wires (effective) 150μm Cu/Be (50/50) –18 planes	5.40	0.0068	87.9	0.0368	0.42
Polystyrene (scintillator)	1.03	2(1.067)(1.0)	70	2.198	31.40
Čerenkov Windows 0.040 in. Al (entrance/exit)	2.7	2(0.102)	88.5	2(0.275)	6.22
Čerenkov Gas (C_4F_{10})	0.00856	150	78.8	1.28	16.29
Rohacell Mirror Support	$\sim$0.05	$\sim$1.8	$\sim$70	0.09	1.3
Mirror SiO_2	2.20	0.3	83.1	0.66	7.94
Polystyrene (scintillator)	1.03	1(1.067)(1.0)+ $\frac{1}{4}$(1.067)(1.0)	70	1.366	19.50
Total					90.6

Table 6.2: Absorbances of materials in the HMS and target materials other than cryogenic deuterium. Values for HMS and Target components were taken from reference [12].

6.2.3.3 Bremsstrahlung

Bremsstrahlung is the term for energy lost due only to radiation by an electron or positron as it passes through a material [55]. This is the radiation which produced the photons used in these experiments. The bremsstrahlung was caused by two interactions–as a result of the atomic (copper) nucleus and as a result of the electrons surrounding the nucleus. Thus two cross sections are needed to describe the probability that a bremsstrahlung photon will be produced [74]:

$$\frac{d\sigma}{dk} = \frac{\alpha r_o^2 Z^2}{k} \Phi_n(Z, E_0, k), \tag{6.12}$$

for the electron-nuclear bremsstrahlung and

$$\frac{d\sigma}{dk} = \frac{\alpha r_o^2 Z}{k} \Phi_e(Z, E_0, k), \tag{6.13}$$

for the electron-electron bremsstrahlung. Combining Eqs. 6.12 and 6.13 the total bremsstrahlung cross section is obtained:

$$\frac{d\sigma}{dk} = \frac{\alpha r_o^2}{k} [Z^2 \Phi_n(Z, E_0, k) + Z\Phi_e(Z, E_0, k)]. \tag{6.14}$$

In Eq. 6.14 α is the fine structure constant, $\frac{1}{137}$, $r_o^2 = \frac{e^2}{mc^2}$, and k is the photon energy. The terms $\Phi_{n(e)}$ are the bremsstrahlung fluxes for nuclear and electron bremsstrahlung respectively.

Two approaches exist for evaluating the bremsstrahlung cross section and produce the spectrum of photons emitted. The first assumes that the radiator is infinitely thin. This method can be reasonably used for radiators which are approximately 1% of a radiation length, or less, but overestimates the yield for thicker radiators. The solution is to employ a method which will calculate the bremsstrahlung spectrum accomodating the thickness of the radiator material. Such a method was developed by Matthews and Owens [74] and takes into account changes in the energy distribution of the incoming electron beam as it passes through the radiator.

The “thick target” bremsstrahlung used in these experiments was calculated using the radiator thickness (See Chapter 5 Section 5.2.1) and the method of Matthews and

Owens incorporated into a computer code developed by David Meekins at Jefferson Lab. The calculation is accurate to 3% so long as the region of the spectrum used is away from the end point which is difficult to calculate [74]. This code produced not only the resultant bremsstrahlung spectrum, but also the electron energy loss distribution after the electron beam had passed through the radiator. This was important for calculating the correct virtual bremsstrahlung distribution used in E96-003, the calculation of the bremsstrahlung produced by the cryogenic deuterium also needed in E96-003, and the value of the function $F(E)$ used in Eq. 6.8. To obtain the total number of photons per electron which were produced by the copper radiator, the spectrum was integrated across the photon energy window (the integral was across the 5 MeV bins into which the photon energy window was broken up in E99-008) to produce $N_{\gamma_{Cu}}$. In E99-008, no further correction was needed to the number of photons.

The function $F(E)$ serves to accomodate the differences between the radiator-in and radiator-out data. The purpose of the radiator-out data, in E99-008, is to remove events caused by electroproduction. After the electron beam passes throught the Cu radiator, the energy distribution is different from that of the initial electron beam, which is very nearly mono-energetic. An example of the electron beam shape after passing through a 4% radiator can be seen in Fig. 6.22. Because of these electron beam energy distribution differences between the radiator-in data and radiator out data, the number of events detected by the radiator-out data is higher than is actually produced by the radiator-affected residual electron beam. To compensate for this, the thin target approximation is used to generate the bremsstrahlung spectrum from the deuterium cryogen. This is done with and without the beam energy shape change caused by the Cu radiator. The ratio of these two spectra were taken in the photon energy window used in the analysis [12]. In E99-008, the ratio was broken up to correspond with the energy window binning used in the analysis. This ratio, which is about 0.75 for a 6% copper radiator, was then applied to the yield function Eq. 6.8.

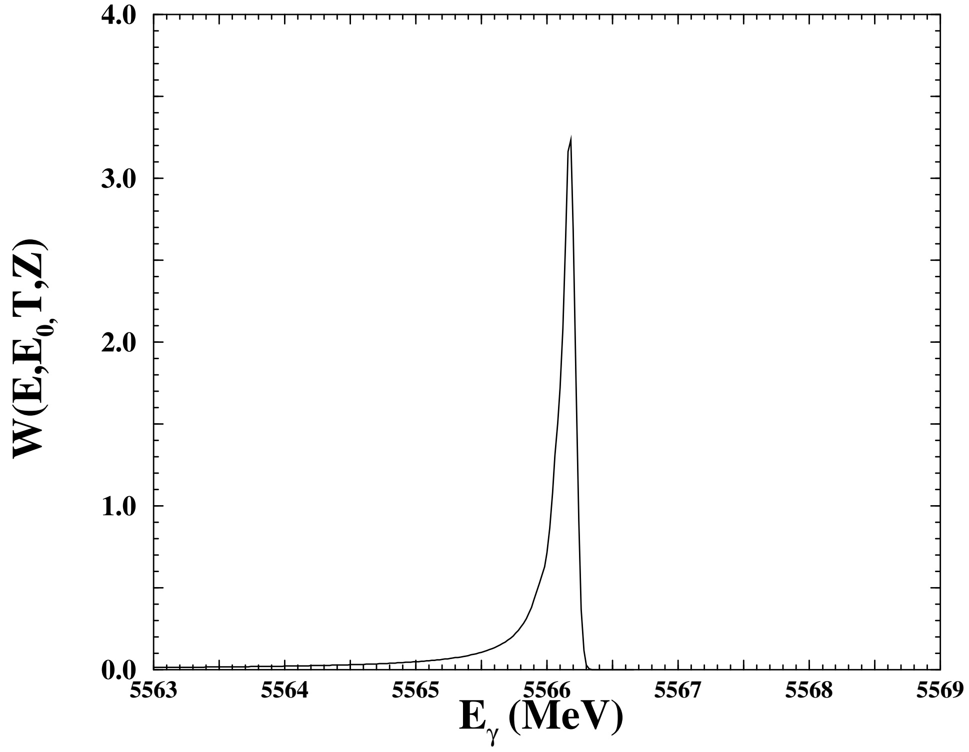

Figure 6.22: An energy loss distribution for 5.566 GeV incident electron beam on a 4% copper target.

For experiment E96-003, bremsstrahlung from upstream the aluminum target end-cap and the cryogenic deuterium must also be taken into account directly and added into the number of photons, N_γ, used to normalize the photoproton yield, because the radiator is always in the beam line. The thin target approximation is used for these calculations and the electron energy beam spread after passing the 2% or 4% copper radiator is used as the input electron energy distribution. This step is not necessary in E99-008. Because this correction is found in the same manner as the overall bremsstrahlung calculation, an additional 3% systematic error is applied for this correction.

6.2.3.4 Virtual Bremsstrahlung

In experiment E96-003 a final adjustment must be made to the total number of photons used in the normalization of the photoproton yield. The effect of electroproduction, which was not subtracted directly, must be taken into account. This was done by using virtual photon theory. That is, the photodisintegration and electrodisintegration differential cross sections are related to each other through the virtual photon which carries the interaction between the incoming electron and the target deuteron.

To employ this technique, an assumption must be made. It is important that the virtual photons must be "nearly real." That is the polarization vector of any given virtual photon must be predominately transverse (perpendicular) to the photon's direction of motion [75]. This is assumed to be the case because the energy region used in the experiment is as near the bremsstrahlung end point as possible. The recoil of the target nucleus must also be taken into account, an item which the Wright and Tiator technique accomplishes.

The technique was originally designed to extract the deuteron photodisintegration differential cross section from the deuteron electrodisintegration differential cross section [75]. The data which were taken produced the following:

$$\frac{d\sigma}{d\Omega_{meas}} = \frac{d\sigma_{\gamma d \to pn}}{d\Omega} + \frac{d\sigma_{ed \to pn}}{d\Omega dE_p}. \tag{6.15}$$

The goal for analyzing the E96-003 data is to convert the electroproduction piece through the virtual photon concept to leave only the photodisintegration differential cross section. Wright and Tiator argue that the electrodisintegration and photodisintegtation can be related to each other, in the limit that the virtual photons are nearly real, by:

$$\frac{d\sigma_{ed \to pn}}{d\Omega dE_p} = \frac{N_e}{\omega_0} R \frac{d\sigma_{\gamma d \to pn}}{d\Omega}. \tag{6.16}$$

In Eq. 6.16 the term $\frac{N_e}{\omega_0} R$ is what was used as the "virtual photon spectrum", where N_e is the Wright and Tiator spectrum, R is the recoil factor needed for light nuclei, and ω_0 is the end point energy [75]. The recoil factor R is

$$R = \frac{M_d + \omega_0 - \frac{E_p}{k_p}\omega_0 \cos\theta_p}{D_0}, \tag{6.17}$$

and N_e is given by

$$N_e = \frac{\alpha}{\pi^2}\frac{\omega_0^2 D_0}{k_i}\int \frac{k_f V_T}{D(\theta_e, \phi_e) q_\mu^4} d\Omega_e. \tag{6.18}$$

In Eqs. 6.17 and 6.18 the factor D are the angular dependent recoil factor and D_0 is evaluated at $\phi_e = 0°$. The quantities k_i and k_f are the electron initial and final momenta and V_T is a function which depends only upon the electron kinematics [75].

Thus to compensate for the electrodisintegration in the data collected during E96-003, the virtual photon spectrum was calculated. This spectrum was integrated over the photon energy window used in the analysis. As with the real bremsstrahlung, this produced a value N_{virt} which was the number of virtual photons per electron produced. Again the beam energy distribution after the radiator was used as the input energy distribution. The quantity N_{virt} was added to the previous real bremsstrahlung quantities to produce the total number of photons which were used to normalize the photoproton yield:

$$N_\gamma = N_{\gamma_{cu}} + N_{\gamma_{tar}} + N_{virt}. \tag{6.19}$$

The systematic error incurred in this process is found through a comparison of the two methods used to suppress events caused by electroproduction. Data at incident photon energies of 2.0 and 2.5 GeV at two center-of-mass angles, $\theta_{cm} = 37°$ and $53°$ were taken during the course of E96-003. These data were taken with the radiator-in/radiator-out method, so a comparison could be directly made between these two techniques. The technique works as follows:

1. Two yields were calculated: the yield due only to real photons (Y_{real}) and the yield which included events caused by both real and virtual photons ($Y_{real+virtual}$).

2. These yields were normalized to the total number of photons which describe the yield ($Y_{real/\gamma}$ and $Y_{(real+virtual)/\gamma}$).

3. The following ratio was produced:

$$R = \frac{Y_{real/\gamma} - Y_{(real+virtual)/\gamma}}{Y_{real}} \tag{6.20}$$

4. Using R in combination with data from a study during E89-012, which investigated how this technique could be applied to future high energy deuteron photodisintegration studies, an average error of 5% was found.

6.2.3.5 The Solid Angle $\Delta\Omega$

The solid angle is the final piece of information needed to convert the photoproton yield into the laboratory differential cross section. The procedure for finding the solid angle was the same for both experiments E96-003 and E99-008. The single arm piece of the Monte Carlo program SIMC, which was originally designed for use with the Hall C spectrometers, was used to simulate the trajectories of the photoprotons through the spectrometer detector system. SIMC was adapted for use with the Hall A HRS's, and the same event generator. The event generator made use of a simple linear fit to the angular distributions. No iteration was performed since the results were very insensitive to the angular distributions.

Events were generated by the event generator and propagated through the "spectrometer" by the computer. The events which succeeded in passing all of the obstacles, such as magnet apertures, and passed to the focal plane were recorded. These simulated events were then analyzed with the same cuts as were applied to the real deuteron photodisintegration data. With the analysis cuts, for both spectrometers, the solid angle was "calculated" to be approximately 6 msr.

A check of the Monte Carlo model was performed by looking at hydrogen elastic singles data. The cross section for hydrogen elastic singles was determined from both from the data and the Monte Carlo simulation. The agreement was quite good. For the HMS in Hall C, the agreement was 2.5% and for the HRS in Hall A 2.6%. This agreement served as the systematic error applied to the solid angle determination.

6.2.4 The Differential Cross Section

Now all of the quantities which are required to change the photoproton yield into the laboratory differential cross section have been obtained. The photoproton yield is converted into the laboratory differential cross section as follows:

$$\frac{d\sigma}{d\Omega_{lab}} = \frac{Y}{n_d N_\gamma T \Delta\Omega}, \tag{6.21}$$

for Hall C where Y is found by Eq. 6.6 and

$$\frac{d\sigma}{d\Omega_{lab}} = \frac{\sum_{j=1}^{b} \frac{1}{\sigma_j^2} \frac{Y_j}{n_d N_\gamma T \Delta\Omega}}{\sum_{j=1}^{b} \frac{1}{\sigma_j^2}}, \tag{6.22}$$

for Hall A where Y_j is found by Eq. 6.8 and b is the number of 5 MeV bins into which the E_γ window was subdivided. In Eq. 6.22 σ_j is the error on the cross section in each bin j. In Eqs. 6.21 and 6.22 T is the target length determined in Section 6.1.1.3. This laboratory cross section is then converted into the center of mass cross section through the Jacobian:

$$\frac{d\sigma}{d\Omega_{cm}} = \frac{d\sigma}{d\Omega_{lab}} . \frac{d\Omega_{lab}}{d\Omega_{cm}} \tag{6.23}$$

The Jacobian $\frac{d\Omega_{lab}}{d\Omega_{cm}}$ is related to the laboratory and center of mass scattering angles

$$\frac{d\Omega_{lab}}{d\Omega_{cm}} = \frac{\sin^2\theta_{lab}}{\sin^2\theta_{cm}}[\cos\theta_{cm}\cos\theta_{lab} + \gamma_{cm}\sin\theta_{cm}\sin\theta_{lab}], \tag{6.24}$$

and the factor γ_{cm} is the quantity which converts the laboratory coordinates into the center of mass coordinates:

$$\gamma_{cm} = \frac{\bar{E}_\gamma + m_d}{[m_d(2\bar{E}_\gamma + m_d)]^{\frac{1}{2}}}. \tag{6.25}$$

The differential cross section, in turn, is converted into the invariant cross section $\frac{d\sigma}{dt}$, where t is the Mandelstam variable which describes the momentum transfer, through:

$$\frac{d\sigma}{dt} = \frac{d\sigma}{d\Omega_{cm}} \frac{d\Omega_{cm}}{dt} \tag{6.26}$$

$$\frac{d\Omega_{cm}}{dt} = \frac{\pi}{\bar{E}_{\gamma,cm} p_{p,cm}}. \tag{6.27}$$

In Tables 6.3 and 6.4 are the measured differential cross sections for experiments E96-003 and E99-008 respectively.

Cross Sections				
E_{beam} (GeV)	$\bar{E}_\gamma$ (GeV)	θ_{cm}	$\frac{d\sigma}{d\Omega_{cm}}$ $(\frac{pb}{sr})$	$s^{11}\frac{d\sigma}{dt}$ (kb GeV^{20})
5.066	5.016	36.9°	10.89 ± 0.73 ± 1.12	5.48 ± 0.37 ± 0.63
	5.011	52.8°	2.36 ± 0.40 ± 0.23	1.18 ± 0.20 ± 0.13
	5.005	69.9°	1.12 ± 0.30 ± 0.11	0.56 ± 0.15 ± 0.06
5.566	5.516	36.9°	4.90 ± 0.31 ± 0.51	5.40 ± 0.34 ± 0.63
	5.511	52.8°	1.39 ± 0.23 ± 0.14	1.52 ± 0.26 ± 0.18
	5.505	69.8°	0.42 ± 0.12 ± 0.04	0.46 ± 0.13 ± 0.05

Table 6.3: Center of mass and s^{11} scaled cross sections for Jefferson Lab Experiment E96-003. The errors are shown first stastical followed by systematic error.

Angular Distribution Cross Sections			
θ_{cm} (nominal)	1.670 GeV	1.950 GeV	2.500 GeV
	$\frac{d\sigma}{d\Omega_{cm}}$ $(\frac{nb}{sr})$	$\frac{d\sigma}{d\Omega_{cm}}$ $(\frac{nb}{sr})$	$\frac{d\sigma}{d\Omega_{cm}}$ $(\frac{nb}{sr})$
26.6°	19.2 ± 0.2 ± 1.1	–	–
30.3°	14.6 ± 0.3 ± 0.9	6.3 ± 0.1 ± 0.4	1.7 ± 0.3 ± 0.1
37.4°	8.7 ± 0.2 ± 0.5	4.02 ± 0.04 ± 0.23	0.89 ± 0.02 ± 0.05
53.6°	4.3 ± 0.1 ± 0.3	1.93 ± 0.04 ± 0.11	0.47 ± 0.01 ± 0.03
70.7°	3.4 ± 0.1 ± 0.2	1.72 ± 0.01 ± 0.10	0.32 ± 0.01 ± 0.02
90.8°	2.6 ± 0.1 ± 0.2	1.08 ± 0.02 ± 0.08	0.18 ± 0.02 ± 0.01
110.7°	2.5 ± 0.1 ± 0.2	1.01 ± 0.03 ± 0.07	0.23 ± 0.03 ± 0.02
127.6°	3.0 ± 0.1 ± 0.2	1.1 ± 0.1 ± 0.1	–
143.5°	4.4 ± 0.2 ± 0.3	1.2 ± 0.2 ± 0.1	0.44 ± 0.07 ± 0.03

Table 6.4: Center-of-mass cross sections for Jefferson Lab Experiment E99-008. The errors shown are first statistical followed by systematic error. Measurements were not made for $\theta_{cm} = 26°$ at 1.95 and 2.5 GeV, due to spectrometer limitations. At $\theta_{cm} = 127°$ at 2.5 GeV, a support post for the target chamber obscured the target making the data unusable. The θ_{cm} values listed are at $E_{beam} = 1.670$ GeV. Values at the remaining energies vary only by a small amount.

6.3 Systematic Errors

Systematic errors, or the estimate of how well the experiment was performed, were estimated to be approximately 10% for E96-003 and approximately 8% in the worst case for E99-008. The errors in E96-003 were dominated by the use of the virtual photon method for the conversion of electroproduction into photodisintegration (5%). In E99-008 systematic errors were dominated by the background suppression method which contributed 5% in the worst cases at $\theta_{cm} = 143°$.

Corrections and Systematic Error Budget E99-008		
	Correction (%)	Systematic Error (%)
Radiator Correcton to Photon Number $F(E_\gamma)$	< 25	3
Matthews and Owens		3
–Bremsstrahlung Calculation		
Radiator Thickness		0.1
E_γ Reconstruction (Angle and Momentum)		0.6
Momentum Resolution (0.2%)		
Proton Attenuation	<9	2
Tracking Efficiency	1	1
Scintillator Efficiency	0.1	
Electronics Dead Time	1	1
Beam Current		0.3
Beam Energy		0.02
Solid Angle ($\Delta\Omega$)		2.6
Target Density	<0.5 at 50 μA	
Target Length		1.3
Background Subtraction:		
Forward Angles ($\theta_{cm} \leq 70°$)		1.1
Background Subtraction:		
Backward Angles ($90° \leq \theta_{cm} \leq 127°$)		4
Background Subtraction:		
Backward Angles ($\theta_{cm} = 143°$)		5.2

Table 6.5: Corrections applied to the data and systematic errors for Experiment E99-008. Center of mass angles are given in nominal values.

E96-003 Corrections and Systematic Errors		
	Correction (%)	Error (%)
Radiator in Correction to Photon Number $F(E_\gamma)$	10-15	3
Matthews and Owens Bremsstrahlung Calculation		3
Wright and Tiator Virtual Photon Correction		5
Radiator Thickness		0.1
E_γ Reconstruction (Angle and Momentum)		5.4 in s^{11}
Momentum Measurement		0.3
Momentum Resolution (0.24%)		2
Beam Current		1.4
Beam Energy		2×10^{-4} GeV
s		7.5×10^{-4} GeV^2
Solid Angle		2.5
Particle Identification		3
Proton Attenuation	10-11	2
Tracking Efficiency	2	2
Scintillator Efficiency	0.1-0.2	
Čerenkov Efficiency	0.01	
Electronics Dead Time	0.01	
Target Density	<0.5	
Target Cut		4.5
Target Length		
5.066 37°		2.5
5.066 53° δ=0%		1.5
5.066 53°δ=3%		1.4
5.066 70°		0.5
5.566 37° δ=0%		0.9
5.566 37° δ=3%		2.7
5.566 53°		0.7
5.566 70°		2.4
Background Subtraction		
5.066 37°		2.7
5.066 53° δ=0%		1.4
5.066 53°δ=3		0.29
5.066 70°		1.4
5.566 37° δ=0%		2.1
5.566 37° δ=3%		2.7
5.566 53°		1.6
5.566 70°		1.6

Table 6.6: Corrections applied to the data and systematic errors for Experiment E96-003. Center of mass angles are given in nominal values.

Both experiments suffered errors intrinsic to the thick target bremsstrahlung calculation. According to Matthews and Owens, the procedure is accurate to 3%. This contributed to bremsstrahlung from the radiator and to photon corrections. In both cases the solid angle determination contributed a systematic uncertainty $< 3\%$. Background subtraction in E96-003 only added an additional 3% in the worst case to the systematic error. Errors due to momentum and angle reconstruction uncertainties attributed about 5% to the quantity $s^{11}\frac{d\sigma}{dt}$ in E96-003 and <1% in E99-008. Tables 6.5 and 6.6 have a complete listing of all systematic errors applied to the data in both E96-003 and E99-008.

Chapter 7

Results and Discussion

Now that the data have been analyzed and the differential cross sections extracted, it is important to study what new information has been obtained. First, it is important to assess the consistency of any overlapping data with previous measurements. Next, it must be established what insight these two data sets are providing into the transition from meson exchange to QCD degrees of freedom. This is done both by assessing the consistency of the results with each other, and through the theoretical descriptions which are available for deuteron photodisintegration. Finally, the consistency of the interpretation of these results with other related experiments and controversy surrounding the validity of some interpretations must be investigated.

7.1 Consistency of E96-003 and E99-008

Experiments E96-003 and E99-008 are complimentary experiments designed to assist in the understanding of the transition region from meson-nucleon degrees of freedom to quark-gluon degrees of freedom. The consistency of these two data sets must be investigated. The first question which must be addressed is how well the new data agree with previous measurements taken at or about the same incident photon energies and angles. The second is if, or how well, the information provided by these two data sets agree with each other.

The first item which must be assessed is the consistency of any data taken which overlaps in energy with any previous measurements. In both E96-003 and E99-008 data at energies which overlapped with previous Jefferson Lab and SLAC experiments were taken. In E96-003 some data were taken expressly for the purposes of checking the experimental procedure. In E99-008 the data were taken as a direct result of measuring an angular distribution symmetric about $\theta_{cm} = 90°$.

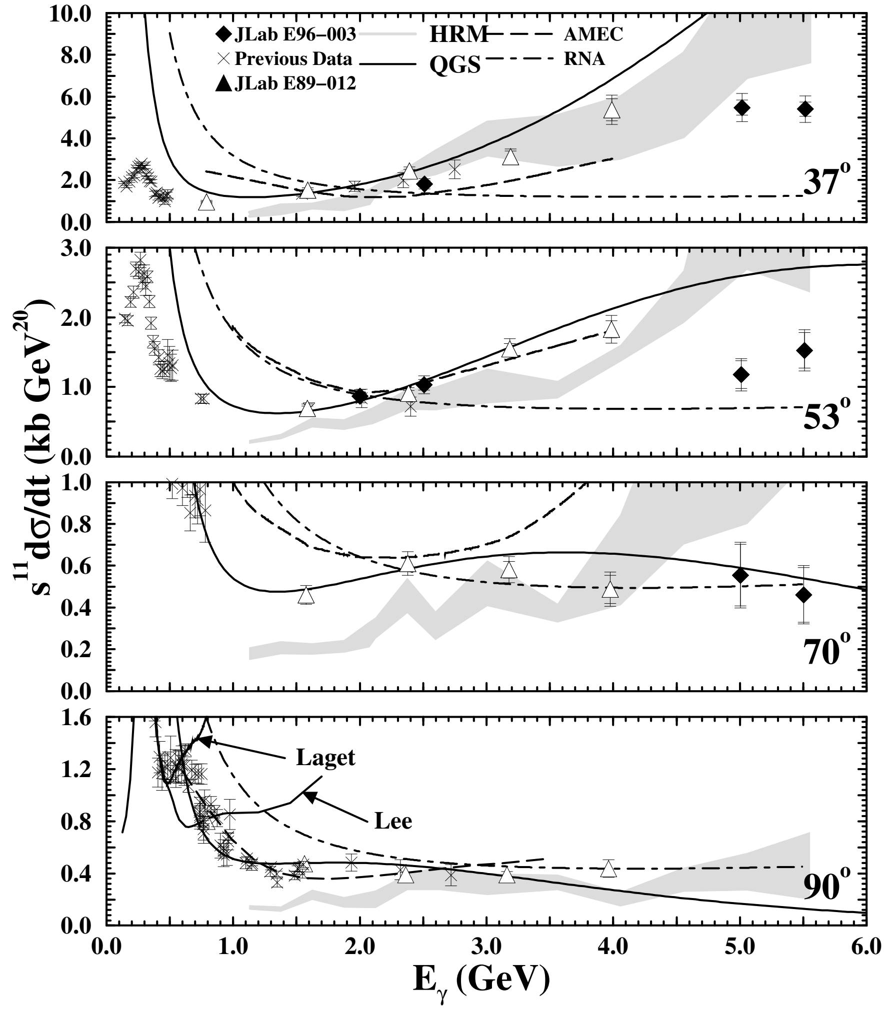

Figure 7.1: $s^{11}\frac{d\sigma}{d\Omega}$ for the $d(\gamma,p)n$ reaction up to E$_\gamma$=5.5 GeV. The present data are in filled diamonds. Previous data are from references [12, 13, 14]

Looking a Fig. 7.1, the solid diamonds at $E_\gamma \approx 2.0$ and 2.5 GeV are in reasonable agreement with the previous data from Jefferson Lab (solid triangles) and SLAC (crosses). The agreement of these data points provides reasonable reassurance that the analysis method employed in experiment E96-003 is reasonable. These data also provide insight into the 5% systematic error applied as a result of the electroproduction background method using virtual bremsstrahlung.

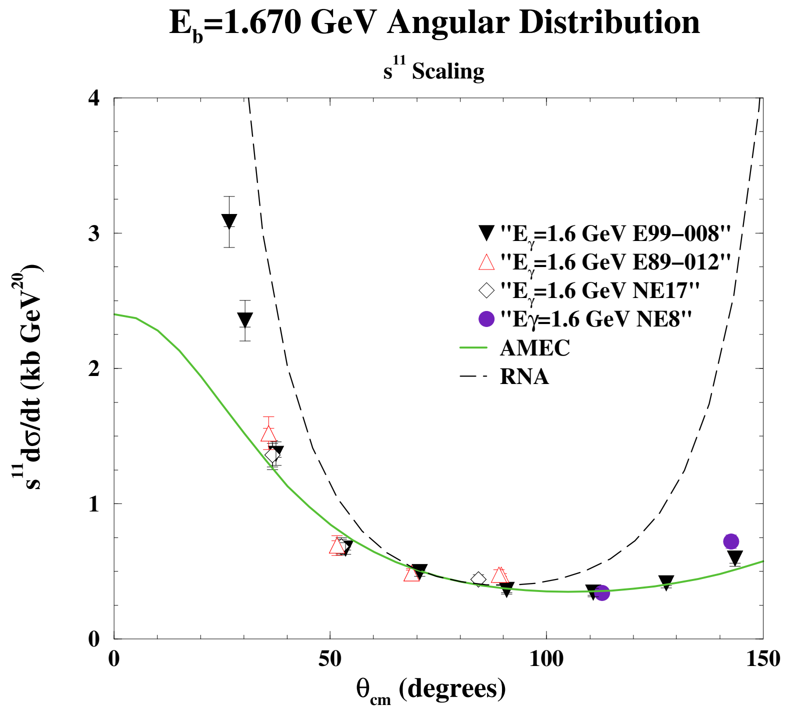

Figure 7.2: Angular distribution of $s^{11}\frac{d\sigma}{dt}$ for $E_\gamma \approx$1.6 GeV. Notice the good agreement with the present data (filled upward facing triangles) with the previous data [12, 13, 14]. The solid curve is the Asymptotic Meson Exchange Model of Nagorny and Dieperink. The dashed curve is the RNA Model.

Figures 7.2 and 7.3 show the angular distribution data plotted as $s^{11}\frac{d\sigma}{dt}$ to minimize any differences in the data points due to energy differences among different experiments. In these figures, the solid downward pointing triangles are the new data from E99-008. Previous Jefferson Lab data is shown as the solid upward facing triangles, and data from SLAC are the solid diamonds (forward angles) and the solid circles

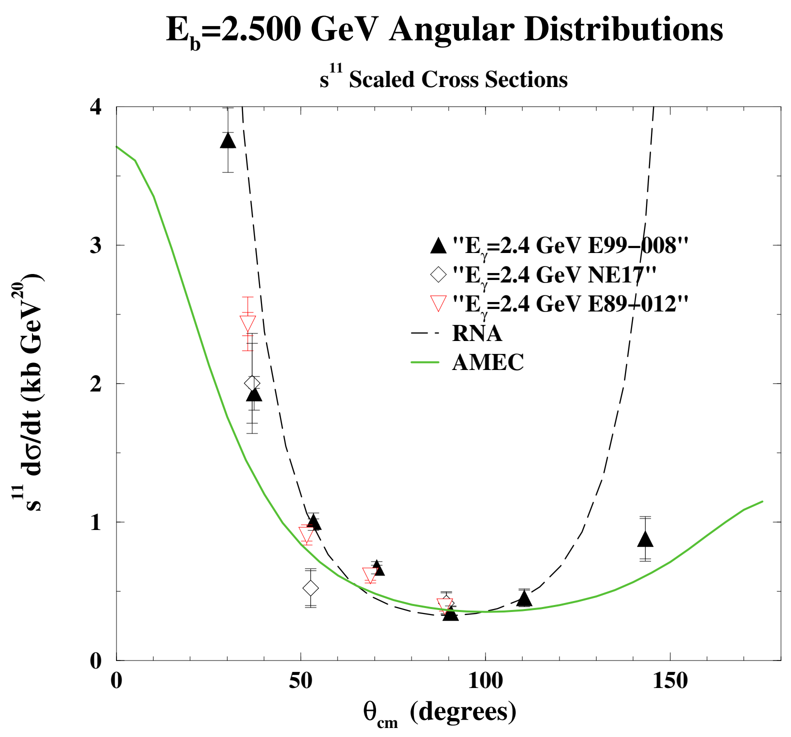

Figure 7.3: Angular distribution of $s^{11}\frac{d\sigma}{dt}$ for E_γ ≈2.4 GeV. Notice the reasonable agreement with the present data (filled upward facing triangles) with the previous data [12, 13]. The solid curve is the Asymptotic Meson Exchange Model of Nagorny and Dieperink. The dashed curve is the RNA Model.

(backward angles). The data at $E_\gamma \approx 1.6$ and 2.4 GeV show very good agreement with previous data. No other data besides that gathered during E99-008 were available for comparison at $E_\gamma = 1.9$ GeV. The agreement of the 1.6 GeV and 2.4 GeV data, however, gives confidence in the analysis method used in these experiments.

7.2 Theories Revisited

In Chapter 3 several available theoretical descriptions of the deuteron photodisintegration differential cross section were discussed. These theories ranged from those based on traditional meson exchange (Section 3.1) to the the simple scaling prediction of perturbative QCD (Section 3.6). By comparing the new data to the available descriptions, some insight can be obtained into how best to describe deuteron photodisintegration in the few GeV energy region.

Not all of the available theories extend their predictions up to the new $E_\gamma = 5.5$ GeV energy point that was measured in experiment E96-003, and even fewer provide angular distributions at the energies which were measured in E99-008. Nevertheless, of those which do provide predictions at high energies, agreement is inconclusive. First, no traditional meson exchange calculation extends much beyond $E_\gamma = 1.5$ GeV, and these calculations are only available at $\theta_{cm} = 90°$. The asymptotic meson exchange model (Section 3.2) only provides a description up to $E_\gamma \approx 4.0$ GeV, and gives mixed results. At $\theta_{cm} = 37°$ and $53°$ the energy dependence of AMEC is reasonably good (see Fig. 7.1, the dashed line). At $\theta_{cm} = 70°$, however, the description is quite poor. AMEC, however, is one of the few descriptions available which gives an angular dependence. In Figs. 7.2 and 7.3 the solid curve is the AMEC prediction for the angular distribution of the deuteron photodisintegration differential cross section. AMEC is able to reproduce the shape, at relatively large angles, of the distribution reasonably well at both energies for which a prediction is available. At smaller angles, $\theta_{cm} < 40°$ the prediction disagrees with the data. Nevertheless, the angular distribution exhibits a forward-backward asymmetry consistent with a MEC model and inconsistent with a quark exchange model.

The Reduced Nuclear Anplitudes model (RNA) (see Section 3.3) of Brodsky and Hiller (or Quark Exchange model by Radushkin), is a description which attempts to take into account the composite nature of the nucleons. The prediction which is given by the RNA model can be seen in the "short-long" dashed line in Fig. 7.1. The prediction is normalized to the $\theta_{cm} = 70°$ data point at about $E_\gamma = 2.5$ GeV. This normalization is kept at all angles presented in Fig. 7.1. For this normailzation the energy dependence of RNA is reasonably good above certain incident photon energies, $E_\gamma \approx 4$ GeV at $\theta_{cm} = 37°$; $E_\gamma \approx 3$ GeV at $\theta_{cm} = 53°$; and $E_\gamma \approx 2.5$ GeV at $\theta_{cm} = 70°$. The angular dependence, however, is not well reproduced by RNA. The RNA/Quark Exchange model predicts a symmetric angular dependence about

$\theta_{cm} = 90°$. The angular dependency data from E99-008 clearly shows that up to at least $E_\gamma = 2.4$ GeV the angular distribution is not symmetric. In fact it is quite asymmetric (Figs. 7.4, 7.5, and 7.6). Therefore, the RNA model fails to reproduce the angular dependence.

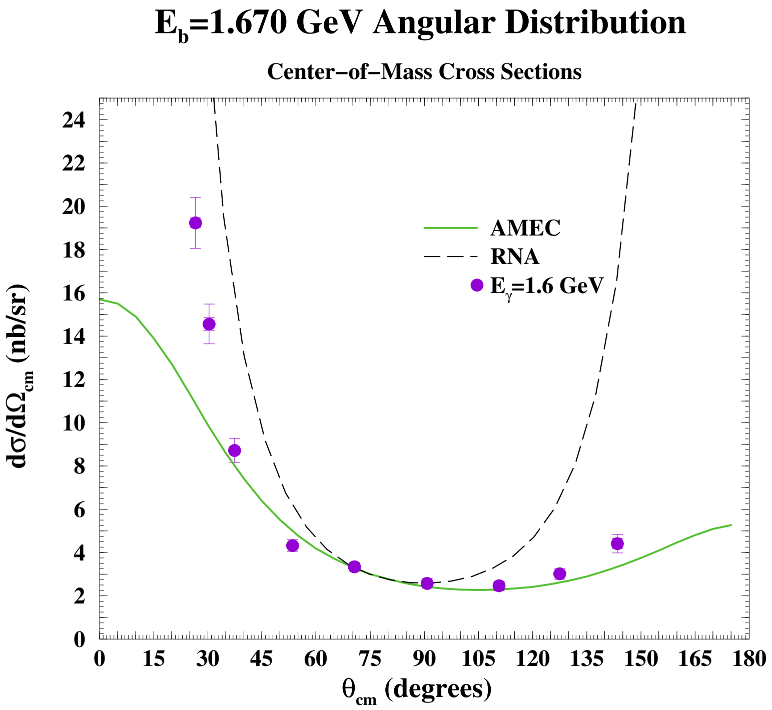

Figure 7.4: Angular distribution of center-of-mass cross sections for $E_\gamma \approx 1.6$ GeV. The solid curve is the Asymptotic Meson Exchange Model of Nagorny and Dieperink. The dashed curve is the RNA Model.

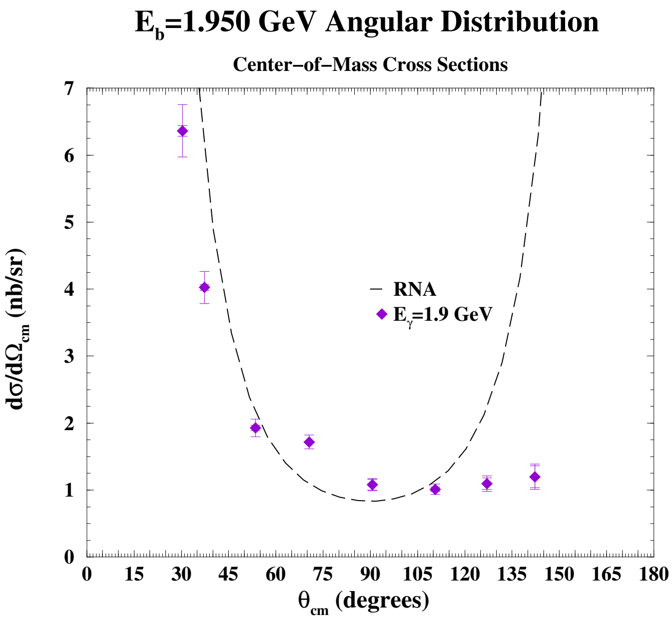

Figure 7.5: Angular distribution of center-of-mass cross sections $\frac{d\sigma}{d\Omega_{cm}}$ for $E_\gamma \approx 1.9$ GeV. The dashed curve is the RNA Model.

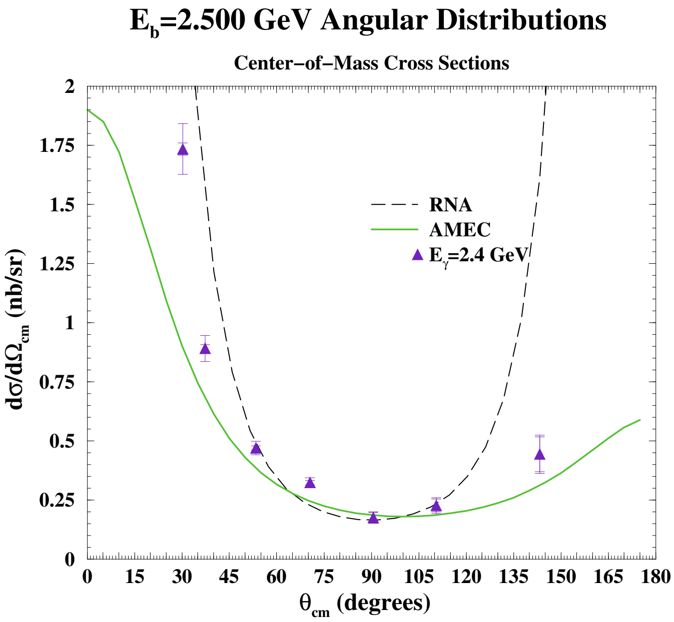

Figure 7.6: Angular distribution of center-of-mass cross sections $\frac{d\sigma}{d\Omega_{cm}}$ for $E_\gamma \approx 2.4$ GeV. The solid curve is the Asymptotic Meson Exchange Model of Nagorny and Dieperink. The dashed curve is the RNA model

The Hard Rescattering Model (HRM) is the grey shaded area in Fig. 7.1. This model is a hybrid model between traditional views of nuclear physics and quantum chromodynamics (see Section 3.4). The uneven nature of the shaded area is the direct result of using the neutron-proton scattering data to parametrize the hard quark rescattering part of the description. The energy dependence is reasonably well described by the HRM up to about $E_\gamma = 4$ GeV, but is unable to predict the behavior of the cross section above this value. No explicit angular distribution prediction, of the type needed to compare to the data in E99-008 is available for this description; however, inspection of the E96-003 data suggests that the HRM does a fair job of reproducing the angular distribution for angles $\theta_{cm} = 90^\circ$ and forward.

The Quark Gluon String (QGS) model, which uses a non-linear Regge trajectory (see Section 3.5) to describe the deuteron photodisintegration differential cross section, is shown as the long-dashed curve in Fig. 7.1. Notice that below $E_\gamma \approx 4$ GeV the QGS prediction is in reasonable agreement with the data in both energy and angular dependence. Above this, however, at $\theta_{cm} = 37^\circ$ and 53° the model does not predict the result particularly well, although, it does predict the turn over at $\theta_{cm} = 53^\circ$. At $\theta_{cm} = 70^\circ$, however, the QGS prediction appears to be quite reasonable.

The final description which is available for investigation is the pQCD scaling prediction (see Section 3.6):

$$\frac{d\sigma}{dt}(AB \to CD) \sim \frac{1}{s^{n-2}} f(\theta_{cm}). \tag{7.1}$$

This scaling law describes the deuteron photodisintegration differential cross section quite well at $\theta_{cm} = 90^\circ$, and reasonably so at $\theta_{cm} = 70^\circ$ in previous measurements. Such scaling had not yet been seen at forward angles, however [4]. The new measurements from experiment E96-003 appear to have provided evidence of a scaling threshold at the forward angles of $\theta_{cm} = 37^\circ$ and 53°.

What is causing the onset of scaling is still a puzzle, however. Brodsky and Hiller in the RNA model suggest that it is the transverse momentum P_T which is the kinematic quantity which should be responsible for the onset of scaling behavior [19].

They also suggest that such scaling should occur for values of P_T above 1 GeV, the value for which scaling appears to set in deuteron form factor measurements. Previous experiments ruled out the P_T=1 GeV value for the onset of scaling [4] because, while it did appear to describe the onset of scaling at $\theta_{cm} = 90°$ and $70°$, this value did not have any predictive power at forward angles. Observing the new data in Fig. 7.1 one begins to see a region where the data go from an energy dependence which is not s^{-11} to an energy dependence which agrees with s^{-11} predictions. Using the apparent thresholds in the 37° and 53° data ($E_\gamma \approx 4$ GeV and 3 GeV respectively) and using the formula for transverse momentum,

$$P_T^2 = \frac{1}{2} m_d E_\gamma \sin^2(\theta_{cm}), \tag{7.2}$$

a value for P_T can be calculated for each apparent threshold. Taking the average and standard deviation of these values, the resultant value for P_T is 1.3±0.1 GeV/c. This is a value which is consistent with scaling at all center of mass angles at which scaling is observed, and shows promise as a predictor of this behavior.

As discussed in Chapter 3, several models exist, each using a different technique, to describe the deuteron photodisintegration differential cross section. Each model has strengths and weaknesses in its description of the data. Few of the models, even those which incorporate quandum chromodynamic elements, are able to predict the high energy behavior seen in the data up to $E_\gamma = 5.5$ GeV. A scaling threshold appears to have been uncovered with a transverse momentum value, $P_T = 1.3 \pm 0.1$ GeV/c. This seems to provide the first evidence of quark effects in a nuclear reaction. Nevertheless, the applicability of perturbative QCD to this, and any exclusive reaction, is still in question. This value of P_T gives photon energy values, 2.0 GeV at 70° and 1.8 GeV at 90° in the center of mass. At both of these energies, the data are consistent with consistuent counting rule scaling.

7.3 What Has Been Encountered?

The question which must now be addressed is just exactly what has been encountered in these new data. From among the available descriptions to date, the pQCD scaling description seems to provide the best fit, with values for $n-2$ of 11.0 ± 0.4 at $\theta_{cm} = 37^{\circ}$ and 11.0 ± 0.3 at $\theta_{cm} = 53^{\circ}$ from linear regression fits to $s^{-(n-2)}$ above threshold values. It is possible for this evidence to be interpreted simply as evidence for the applicability of perturbative calculation techniques of QCD in an exclusive process (that is a process in which the initial and final kinematics are known [76]). There is a catch; inconsistencies with this interpretation abound. The most striking is the evidence from polarization measurements of the recoil proton in polarized deuteron photodisintegration. Before addressing this issue, however, a brief look at the arguments for and against the application of pQCD to exclusive reactions should be taken.

Isgur and Lewellyn-Smith argue that it is not appropriate to apply perturbative QCD to exclusive reactions at presently attainable energies [37]. Brodsky, however, argues that it is possible to apply such ideas, at high momentum transfer, if a factorization theorem is applied (as in RNA) to separate the hard (short range) and soft (long range) components of the reaction. Brodsky does allow, however, that the transition from the short range to the long range domain can be quite complicated [76]. Isgur and Lewellyn-Smith, on the other hand, argue that the perturbative descriptions available which attempt to describe form factors (nucleon and pion) produce descriptions which are far smaller than the data [37]. They also counter that in most cases the wave functions used were inherently flawed, for example, many are highly asymmetric. In fact, high momentum transfer measurements of the pion momentum distribution appear to have ruled out highly asymmetric wave functions for the pion in favor of more symmetric ones [77]. The crowning point of their argument, which on the surface seems to be quite a blow to the applicability of pQCD in exclusive reactions, is the absence of hadron helicity conservation in such processes [37].

Hadron helicity conservation in QCD is a consequence of helicity conservation in vector interactions such as gluon-quark interactions [76], and evidence of it should be seen in reactions where other evidence, such as constituent counting rule scaling, is seen if pQCD is indeed the most accurate description of the reaction. Thus far, however, no hadron helicity conservation has been observed in exclusive reactions. There may be a reason for this, however. Recently a new look at the results of polarized reactions, such as polarized deuteron photodisintegration and proton-proton elastic scattering, has provided some exciting new thoughts on why hadron helicity conservation has not been seen, even when pQCD scaling continues to persist.

Recent measurements of polarized deuteron photodisintegration, performed at Jefferson Lab in Hall A, were made at $\theta_{cm} = 90^\circ$ up to an incident photon energy of 2.4 GeV. This is well within the region in previous measurements of the deuteron photodisintegration differential cross section where constituent counting rule scaling had set in at $\theta_{cm} = 90^\circ$. No conclusive hadron helicity conservation was observed in these data [44]. This phenomenon had been observed before in proton-proton elastic scattering [78], where something else was also noticed. The proton-proton differential cross section appeared to oscillate about the s^{-10} scaling value (see Fig. 7.7) [78, 79]. For proton-proton elastic scattering a probable solution to this anomaly is the effect of Landshoff processes [78]. Landshoff processes are a series of independent scatterings in which each constituent scatters from at least one non-parent hadron constituent [80].

Long range processes can be associated with sugnificant gluon radiation. The radiative corrections associated with the gluon radiation are believed to produce a phase in the long-distance amplitude which is calculable in pQCD [81]. This phase can be momentum-dependent at medium energies and are analogous to phase shifts in Coulomb-nulcear interference in charged particle scattering [79, 78, 82, 83]. By fitting these phases to proton-proton elastic scattering data, the solid curve in Fig. 7.7 is produced. Long distance processes, like Landshoff processes, can also cause interference terms which may mask hadron helicity conservation. Using the parameters found for the curve in Fig. 7.7 the beam-target spin parameter A_{nn} can be reproduced at $\theta_{cm} = 90°$ [78].

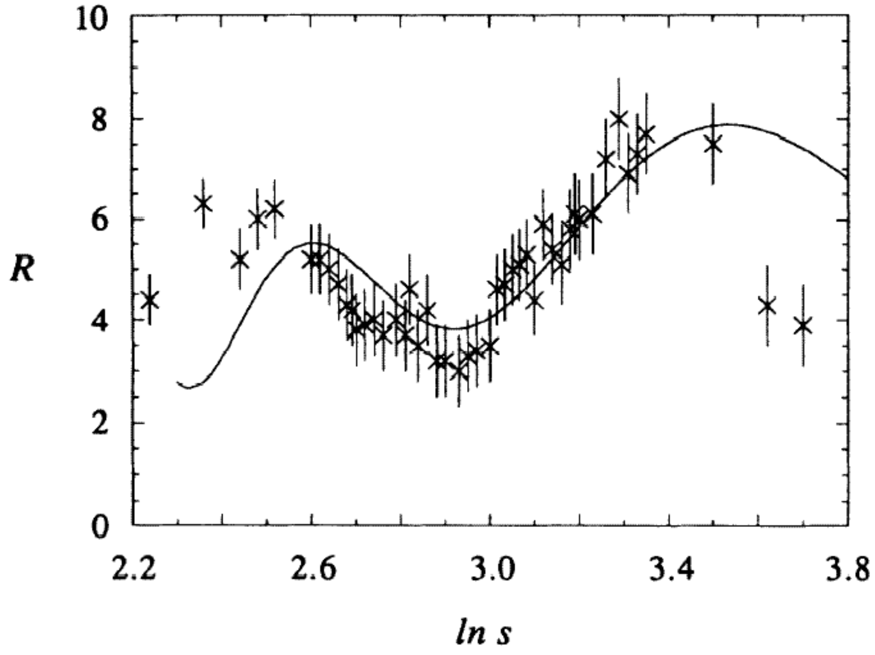

Figure 7.7: Proton-proton elastic differential cross section plotted as $s^{-10}\frac{d\sigma}{dt}$ (R). Notice the appearance of oscillations about s^{-10}. Data are as compiled in Ref. [78]. The solid curve is the fit to the data as described in Ref. [78]. An earlier fit to the data is described in Ref. [79].

Photoreactions, like deuteron photodisintegration, were then turned to as an arena for searching for hadron helicity conservation. Landshoff processes were believed to be unimportant in photoreactions because the incident particle has no underlying structure. Therefore, hadron helicity conservation, the penultimate signature, along with the constituent counting rule scaling, should be observable if pQCD is valid [84]. To date, no hadron helicity conservation has been observed.

This would seem to completely rule out the validity of pQCD as the underlying process causing the scaling, consistent with consitutent counting rules, which is observed in the E96-003 data. Recently, however, this view has been revisited. A second look at the data at $\theta_{cm} = 90°$ has been taken by the theorist Misak Sargsian from Florida International University. He suggests that oscillations, similar to those found in proton-proton elastic scattering, are not excluded in the high energy (E_γ above about 1 GeV) deuteron photodisintegration differential cross section at $\theta_{cm} = 90°$ [85]. This may suggest the presence of a final state, or some other "long range" interaction, such as Landshoff processes, which may be causing interference, possibly masking a clear measurment of hadron helicity conservation [85], even in photoreactions.

These recent developments complicate the search for the underlying cause of the scaling behavior, now seen at all forward angles, in deuteron photodisintegration. What does seem to be clear is that, to date, only descriptions which involve QCD degrees of freedom are able to describe the data above a scaling threshold, and the constituent counting rules seem to give the best description. The high energy angular distribution data support the view that pQCD is not a viable description of the deuteron photodisintegration differential cross section for incident photon energies 2.4 GeV and below. This is not in conflict with other, forward angle, measurements up to 2.4 GeV where only $\theta_{cm} = 70°$ and $90°$ show consistency with constituent counting rule scaling. The high energy data (E96-003) do appear to support the concept that the few GeV energy region is, indeed, a transition region from meson-nucleon degrees of freedom to quark-gluon degrees of freedom. Nevertheless, a full and accurate description of this region is proving quite complicated.

Chapter 8

Summary

Deuteron photodisintegration is a nuclear reaction which has been used to explore the intermediate energy region. This region, a few GeV in incident photon energy, appears to contain a transition region from the traditional meson-nucleon degrees of freedom used to describe nuclear reactions to the quark-gluon degrees of freedom of quantum chromodynamics. Understanding this transition region is an important goal for nuclear physicists.

New high energy measurements of the deuteron photodisintegration differential cross section were made at Jefferson Laboratory during experiments E96-003 (in Hall C) and E99-008 (in Hall A). These experiments were designed to push the highest energy at which the differential cross section was measured up to 5.5 GeV incident photon energy (E96-003) and to measure a complete angular distribution with points symmetrically measured about $\theta_{cm} = 90^\circ$ (E99-008). These experiments, while in principle quite straightforward, each had their own experimental complexities.

Challenges facing the analysis of these data surrounded, primarily, the suppression of background from non-deuteron photodisintegration sources. In experiment E96-003 high backgrounds were a problem which required skillful, and somewhat creative, suppression techniques. Because both the photon and electron beams impinge upon the target, events caused by electroproduction must be removed, or accounted for in the analysis of the data. Traditionally, this is handled by making measurements with the radiator removed from the beamline, thus being able to directly measure events caused by electroproduction. This was the procedure used in E99-008. Time constraints caused by the very small laboratory cross sections, however, necessitated the use of a different technique in E96-003. By assuming that the virtual photons were predominately transverse and employing an analytical spectrum developed by Wright and Tiator which accounts for the recoil of a light nucleus, the electroproduction events could be accounted for to an accuracy of about 5% with respect to the traditional method of radiator removal.

Several different models exist which attempt to explain the deuteron photodisintegration differential cross section. These different approaches, which range from traditional meson exchange theories to perturbative QCD, meet with differing success. The asymmetry of the angular distribution measurements seems to support a description more in line with a meson-nucleon approach. At forward angles, and high energies, however, a scaling threshold, consistent with the predictions of the consitutent counting rules, seems to be evident above $E_\gamma = 4$ GeV at $\theta_{cm} = 37^\circ$ and $E_\gamma = 3$ GeV at $\theta_{cm} = 53^\circ$. Using these apparent thresholds a transverse momentum value of $P_T = 1.3 \pm 0.1$ GeV$/c$ appears to describe scaling at all angles $\theta_{cm} = 90^\circ$ and forward, at least to $\theta_{cm} = 37^\circ$.

The present understanding of the few GeV region for deuteron photodisintegration is still far from clear. Recent polarization measurements seem to indicate that the simple perturbative assumption is incorrect. A further investigation of this, however, seems to indicate that even with the absence of hadron helicity conservation a definitive ruling on the use of perturbative theory cannot yet be made. It seems reasonable that evidence for the necessity of including QCD degrees of freedom in descriptions of deuteron photodisintegration at the few GeV energy level is necessary, but just what is the exact mechanism remains a puzzle which will require further investigation.

Chapter 9

Outlook

It is becoming apparent that the transition from meson exchange to pQCD is a region which is rich in complexity and detail. Where could the community proceed in its search to understand this important region? Several avenues are available which could be employed to delve into this arena.

Experiments have been planned and proposed to Jefferson Laboratory to begin to study some of the new ideas which have been fostered as a result of this and related research. A measurement of the polarization observables of the recoil proton in $\vec{\gamma}d \rightarrow \vec{p}n$ reaction has been approved for running time at Jefferson Lab in the relatively near future. Another experiment has been proposed to Jefferson Lab to look for possible oscillations in the $\gamma p \rightarrow \pi^+ n$ reaction. Further measurements of the complete angular dependence of the deuteron photodisintegration differential cross section at higher energies, up to 6-7 GeV if equipment should become available, would also help to provide insight into this region.

References

[1] J. Chadwick and M. Goldhaber, Nature **134**, 237 (1934).

[2] J.E. Belz, *et al.*, Phys. Rev. Lett., **74**, 646 (1995).

[3] J. Napolitano, Phys. Rev. Lett. **61** 2530 (1988).

[4] C. W. Bochna, *et al.*, Phys. Rev. Lett. **81**, 4576 (1998).

[5] Halzen, F. and Martin, A., *Quarks and Leptons*, John Wiley & Sons, New York, 1984.

[6] J.I. Friedman and H.W. Kendall, Ann. Rev. Nucl. Sci., **22**, 203 (1972); A. Bodek, *et al.*, Phys. Rev. D, **20**, 1471 (1979).

[7] H. Yukawa, Proc. Phys.-Math. Soc. Japan, **17**, 48 (1935).

[8] Pauli, W., *Meson Theory of Nuclear Forces*, Interscience Publishers, Inc., New York, 1946.

[9] L.R.B. Elton, *Introductory Nuclear Theory*, W.B. Saunders Company, Philadelphia, 1966.

[10] T.S.-H. Lee, Argonne National Laboratory Report No. PHY-5253-TH-88; T.-S.H. Lee, *Proceedings of the International Conference on Medium and High Energy Nuclear Physics, Taipei, Taiwan, 1988* (World Scientific, Singapore, 1988), p. 563.; T.-S. H. Lee, ANL/PP-64910 (1991); ANL/CP–73422, (1991).

[11] J.M. Laget, Nucl. Phys. **A312**, 265 (1978).

[12] Terburg, Bart P., Ph.D. Thesis, University of Illinois, (1999), Unpublished.

[13] Belz, Eric, Ph.D. Thesis, California Institute of Technology (1994), Unpublished.

[14] Tung, T. Y., Ph.D. Thesis, Northwestern University (1992), Unpublished.

[15] P. Dougan *et al.*, Z. Phys. **A276**, 55 (1976); R. Crawford *et al.*, Nucl. Phys **A603**, 303 (1996).

[16] Nambu, Y., "Asystematics of Hadrons in Subnuclear Physics," *Preludes in Theoretical Physics*, Editors A. De-Shalit, F.H. Feshbach, L. Van Hove, North-Holland Publishing Company, Amsterdam, 1966, pp. 133-142.

[17] Quigg, C., *Gauge Theories of the Strong, Weak, and Electromagnetic Interactions*, Addison-Wesley, Reading Massachusetts, 1997.

[18] R. J. Holt, Phys. Rev. C **41** 2400 (1990).

[19] S.J. Brodsky and J.R. Hiller, Phys. Rev. C, **28**, 475, (1983).

[20] V.Y. Grishna, *et al.*, Eur. Phys. J., **A10**, 355 (2001); D. De Sanctis, *et al.*, Phys. Rev. C, **42**, 1764 (1990); L.A. Kondratyuk, *et al.*, Phys. Rev. C, **48**, 2491, (1993).

[21] L.L. Frankfurt, *et al.*, Phys. Rev. Lett., **84**, 3045, (2000).

[22] S.J. Brodsky and G.P. Lepage, Nucl. Phys. **A353**, 247c (1981)

[23] W. Leidemann and H. Arenhövel, Phys. Lett. **139B**, 22 (1984).

[24] T.-S. H. Lee, Phys. Rev. C **29**, 195 (1984).

[25] M. Lacombe, *et al.*, Phys. Rev. C, **21**, 861 (1980).

[26] T.-S. H. Lee, Few-Body Syst. Suppl., **6**, 526 (1992).

[27] Sigfrido, B., *et al.*, *Electromagnetic Response of Atomic Nuclei*, Clarendon Press, Oxford, 1996.

[28] R.V. Ried, Ann.of Phy., **50**, 411 (1968).

[29] A.E.L. Dieperink and S.I. Nagorny, Phys. Lett. **B456**, 9, (1999); S.I. Nagorny, *et al.*, Sov. J. Nucl. Phys., **55**, 189, (1992).

[30] F. Gross and B.D. Keister, Phys. Rev. C, **28**, 823, (1983).

[31] S.J. Brodsky and B.T. Chertok, Phys. Rev. Lett., **37**, 269 (1976).

[32] L.C. Alexa, *et al.*, Phys. Rev. Lett., **82**, 1374 (1999).

[33] S.J. Brodsky, *et al.*, Phys. Rev. Lett. **51**, 83 (1983).

[34] A.V. Radushkin, JLAB-THY-99-Draft.

[35] V.A. Matveev, *et al.*, Lett. Nuovo Cim., **7**, 719 (1973).

[36] V.P. Landshoff and J.C. Polkinghorn, Phys. Lett., **44B**, 293 (1973).

[37] N. Isgur and C.H. Llewellyn Smith, Nucl. Phys., **B317**, 526 (1989).

[38] S.J. Brodsky, *et al.*, SLAC-PUB-8836, (2001).

[39] R.L. Anderson, *et al.*, Phys. Rev. D, **14**, 679 (1976).

[40] D.G. Meekins, *et al.*, Phys. Rev. C, **60**, 052201-1 (1999).

[41] D. Abbott, *et al.*, Phys. Rev. Lett., **82**, 1379 (1999).

[42] A.S. Bratashevskiĭ, *et al.*, Sov. J. Nucl. Phys., **44**, 619 (1986); A.S. Bratashevskiĭ, *et al.*, JETP Lett., **36**, 217 (1982). A.S. Bratashevskiĭ, *et al.*, JETP Lett., **35**, 605 (1982). A.S. Bratashevskiĭ, *et al.*, Sov. J. Nucl. Phys., **31**, 444 (1980). A.S. Bratashevskiĭ, *et al.*, Sov. J. Nucl. Phys., **43**, 499 (1986).

[43] F. Adamian, *et al.*, Eur. Phys. J., **A8**, 423 (2000).

[44] K. Wijesooriya, *et al.*, Phys. Rev. Lett. **86**, 2975 (2001).

[45] S.J. Freedman, *et al.*, Phys. Rev. C, **48**, 1864 (1993).

[46] J. Mitchell, private communication, (2000)

[47] Volmer, J., Ph.D. Thesis, Vrije Universiteit, (2001), Unpublished.

[48] C. Yan, *et al.*, Nucl. Instrum. Meth. **A365**, 261, (1995).

[49] P. Gueye, *Status of the Actual Beam Position Monitors in the Hall C Beamline*, CEBAF Internal Report (1995), unpublished.

[50] C. Yan, JLab-TN-99-006 (1999).

[51] R. Gilman, private communication, (2001).

[52] D. Neuffer, *et al.*, CEBAF-TN-92-054 (1992).

[53] Bochna, Christopher W., Ph.D. Thesis, University of Illinois, (1999), Unpublished.

[54] Liyanage, Nilanga K.B., Ph.D. Thesis, Massachusetts Institute of Technology, (1999), Unpublished.

[55] W.R. Leo, *Techniques for Nuclear and Particle Physics Experiments*, Springer-Verlag, Berlin, 1994.

[56] D. Meekins, *Hall C Bremsstrahlung Radiator Technical Report*, JLab Internal Memo, (1999).

[57] J. Dunne, *Cryo and dummy Target Info*, Internal JLab Memo, (1999).

[58] Suleiman, Riad, JLab Technical Note JLAB-TN-98-007. **A367**, 92 (1995).

[59] Arrington, John R., Ph.D. Thesis, California Institute of Technology, (1998), Unpublished.

[60] http://hallaweb.jlab.org/equipment/HRS.htm

[61] J. Wiss, Physics 470 Course Notes, University of Illinois at Urbana-Champaign (1998) Unpublished.

[62] J. Lerose, private communication, (2001).

[63] E. Hecht, *Optics*, Addison-Wesley Publishing Co., Reading, Massachusetts, 1987.

[64] O.K. Baker, *et al.*, Nucl. Instrum. Meth.

[65] J. Gao, Ph.D. Thesis, Massachusetts Institute of Technology, (1999), Unpublished.

[66] http://hallallaweb.jlab.org/document/OPMAN/

[67] J. Arrington, private communication, (2001).

[68] M. Berz, *COSY Infinity User's Guide and Reference Manual*, National Superconducting Cyclotron Facility, Michigan, 1998.

[69] S.J. Levinger, Phys. Rev., **84**, 43 (1951).

[70] C. Leathers, B.S. Thesis, Massachusetts Institute of Technology (1996).

[71] *Review of Particle Physics*, Eur. Phys. J. **C15**, 1, (2000).

[72] Wijesooriya, Krishni, Private Communication (2001).

[73] D. Van Westrum, Ph.D. Thesis, University of Colorado, (1998). Unpublished

[74] J.L. Matthews and R.O. Owens, Nucl. Instrum. Meth., **111**, 157, (1973).

[75] L.E. Wright and L. Tiator, Phys. Rev. C **26**, 2349 (1982).

[76] S. J. Brodsky, SLAC-PUB-8649, (2000).

[77] E.M. Aitala, *et al.*, Phys. Rev. Lett., **86**, 4768 (2001).

[78] C.E. Carlson, *et al.*, Phys. Rev. D, **46**, 2891 (1992).

[79] J.P. Ralston and B. Pire, Phys. Rev. Lett., **61**, 1823 (1988).

[80] P.V. Landshoff, Phys. Rev. D **10**, 1024, (1974).

[81] A. Sen, Phys. Rev. D, **28**, 860 (1983)

[82] S. J. Brodsky, *et al.*, Phys. Rev. D, **20**, 2278 (1979)

[83] J.P. Ralston and B. Pire, Phys. Rev. Lett., **49**, 1605 (1982).

[84] C.E. Carlson, *et al.*, Ann. Rev. Nucl. Part. Sci., **47**, 395 (1997).

[85] M. Sargsian, Private communication (2001).

[86] M.E. Peskin and D.V. Schroeder, *An Introduction to Quantum Field Theory*, Addison-Wesley, Reading, Massachusetts, 1995.

[87] C. S. Armstrong, *Hall C Time of Flight Fitting Code*, Internal Hall C Memo, (1999).

Appendix A

Mandelstam Variables

The Mandlestam variables are a set of kinematic quantities, that is quantities which are defined by the momenta and angles of the incoming and outgoing particles, which are invariant. Invariant quantities, in this case, are quantities which are the same in both the laboratory and center of mass frame. This simple calculating these quantities.

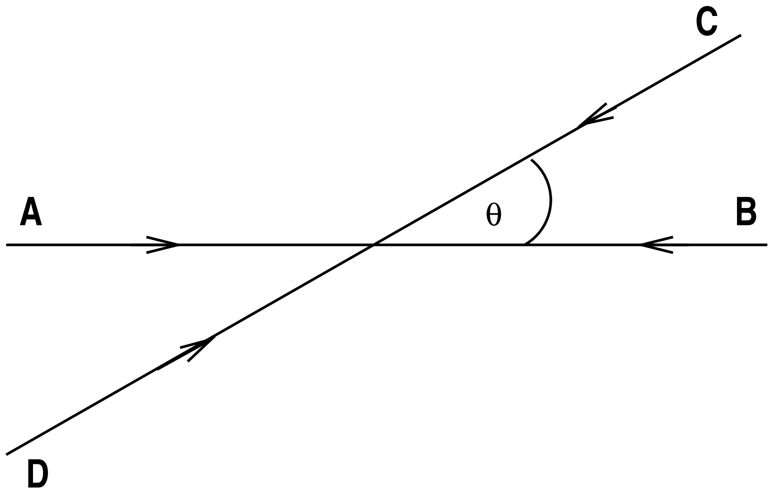

Figure A.1: Schematic diagram of a two body process $AB \rightarrow CD$. The labels *A, B, C, D* are particles with four momenta P_A, etc.

In Fig. A.1 a diagram of a binary process $A + B \rightarrow C + D$ is shown. The four momenta for each particle has the label P_i where$i$ is A, B, C, or D. Four momentum vectors take the following form

$$P = (E, p_x, p_y, p_z) \tag{A.1}$$

where E is the energy of the particle and the remaining components are the three spacial components of the particle's momentum.

There are three Mandelstam variables s, t and u. These variables are defined as [86]

$$s = (P_A + P_B)^2 \tag{A.2}$$

$$t = (P_A - P_C)^2 \tag{A.3}$$

$$u = (P_A - P_D)^2 \tag{A.4}$$

For deuteron photodisintegration particle A is the photon, particle B is the deuteron, and particles C and D are the outgoing proton and neutron respectively.

For this reaction it is most convenient to evaluate the Mandelstam variables in the laboratory frame. The four momenta are given as follows

$$P_A = (E_\gamma, 0, 0, E_\gamma),\ E_\gamma \text{ the photon energy} \tag{A.5}$$

$$P_B = (m_d, 0, 0, 0),\ \text{the deuteron is stationary; } m_d \text{ the deuteron mass} \tag{A.6}$$

$$P_C = (E_p, P_p \sin(\theta_p), 0, P_p \cos(\theta_p)),\ E_p,\ P_p \text{ the outgoing proton energy and three-momentum, } \theta_p \text{ the outgoing proton angle with respect to the photon axis} \tag{A.7}$$

$$P_D = (E_n, P_n \sin(\theta_n), 0, P_n \cos(\theta_n)),\ E_n,\ P_n \text{ the outgoing neutron energy and three-momentum, } \theta_n \text{ the outgoing neutron angle with respect to the photon axis.} \tag{A.8}$$

By performing the vector algebra on these quantities, one acquires for deuteron photodisintegration

$$s = 2E_\gamma m_d + m_d^2 \tag{A.9}$$

$$t = m_p^2 - 2E_\gamma(E_p - P_p \cos(\theta_p)) \tag{A.10}$$

$$u = m_n^2 - 2E_\gamma(E_n - P_n \cos(\theta_n)). \tag{A.11}$$

Appendix B

Time of Flight Optimization

For each experimental setup the timing coefficients for the scintillator hodoscopes must be checked and readjusted to obtain the best timing resolution available for the spectrometer. Many things may cause variations in the timing resolution, changes in the electronics, changes in the particle being detected, etc., the coefficients will change. The two coefficients which are routinely checked are the TDC offsets and the pulse height corrections in Hall C and a "meantime" correction in Hall A.

TDC offsets are caused by differences in cable length among the different phototubes, response times among the PMT's, and the like. The pulse height corrections (PHC's) are added corrections applied to compensate for the effects of different pulse amplitudes on the timing. The first correction calculated is the pulse height correction.

The timing signals are started and stopped by a fixed threshold descriminator [59]. As a result, the acutal time that the discriminator fires depends on the amplitude fo the pulse from the PMT. This can have large effects on the timing resolution. To compensate for this, the pulse height correction and an offset are fitted to data from the scintillator hodoscopes. Because this can be very sensitive to the particles chosen, a clean sample of protons was used for fitting all time of flight corrections. The pulse height correction is fit according to the following formula

$$\Delta t = PHC\sqrt{max(0,(\frac{ACD}{PHOFF}-1))}+t_0 \tag{B.1}$$

where PHC and $PHOFF$ are the values fitted to compensate for the changes in pulse heights, ADC is the ADC value for a reference scintillator bar, and t_0 is an arbitrary offset [59]. Both x and y (crossed) scintillators are used and one of the scintillator PMT's is used in fitting the correction. This limits the area considered in fitting corrections for each PMT. Only the mean times (the average time between the two PMT's on a scintillator bar) are included in the fit, so that time-walk along the scintillator bar is minimized. An average value for the PHC's is used for each plane [87].

After the PHC's are fit, the timing offsets can be fit. This follows the same procedure as given above for the PHC's. With the correct pulse heights, the timing offsets are adjusted to agree with the input particle velocity. The velocity of the particle in question, protons in this case, must be selected in order for the fitting to work properly. Again, average values for the TDC offsets are used for each plane.

In Hall A the same offsets are fit to a sample of data of the desired type (i.e. protons). All timing variations are referenced off of the right hand side phototubes of the second hodoscope plane (S2). The crossed scintillator procedure cannot be used in Hall A because of the design of the scintillator hodoscopes. A mean time is calculated to compensate for timing variations in the hodoscope arising from variations in event position [65].

Vita

Elaine Carol Schulte received her Bachelor of Science from the University of Illinois at Urbana-Champaign in Physics in May 1997. She continued with her graduate education at the University of Illinois, earning her Master of Science (January 2001) and her Doctor of Philosophy (May 2002) both in Physics. In the Spring Term 1997, she received the Laura B. Eisenstein Award for Outstanding Woman in Physics; and for the Spring Term 2000 an Outstanding Teaching Assistant Award. She was a recipient the 1999-2000 GAANN Fellowship.

Talks and Presentations

Fall 1999	Contributed Talk	Fall Meeting of the American Physical Society, Division of Nuclear Physics, Asilomar, CA
Summer 2000	Contributed Talk	Gordon Research Conference on Photonuclear Reactions, Tilton NH
Fall 2000	Contributed Talk	Fall Meeting of the American Physical Society, Division of Nuclear Physics, Williamsburg, VA
Spring 2001	Contributed Talk	Annual Meeting of the American Physical Society, Washington, DC

Publications List

1. E. C. Schulte, *et al.*, Phys. Rev. Lett. **87**, 102302 (2001).

2. K. Wijesooriya, *et al.*, Phys. Rev. Lett. **86**, 2975 (2001).

3. O. Gayou, *et al.*, Phys. Rev. C **64**, 038292 (2001).

4. R. V. Cadman, *et al.*, Phys. Rev. Lett. **86**, 967 (2001).

5. Schulte, E. C., *et al.*, Proceedings of the 7th International Workshop on Polarized Gas Targets and Polarized Beams, Edited by R. J. Holt and M. A. Miller, New York: American Institute of Physics, 1997, pp. 465-466.